JP0250073

MAGNETIZATION OF NEUTRON STAR MATTER AND IMPLICATIONS IN PHYSICS OF SOFT GAMMA REPEATERS

January 2002

V. N. Kondratyev

Magnetization of Neutron Star Matter
and Implications in Physics of Soft Gamma Repeaters

V.N.Kondratyev

Advanced Science Research Center
(Tokai Site)
Japan Atomic Energy Research Institute
Tokai-mura, Naka-gun, Ibaraki-ken

The magnetization of neutron star matter is considered within the thermodynamic formalism. The quantization effects are demonstrated to result in sharp abrupt magnetic field dependence of nuclide magnetic moments. Accounting for inter-nuclide magnetic coupling we show that such anomalies give rise to erratic jumps in magnetotransport of neutron star crusts. The properties of such a noise are favorably compared with burst statistics of Soft Gamma Repeaters.

中性子星物質の磁化とソフトガンマリピーターの物理との関連

日本原子力研究所先端基礎研究センター

V.N.Kondratyev（コンドラチェフ　ヴォロディミール）

熱力学的扱いにより中性子星物質の磁化を考察する。量子効果から核種の磁化に鋭い磁場依存性が生じることを示す。原子核間の磁気的結合を考慮する事でその異常が中性子星の殻での磁気輸送の異常な飛びを引き起こす。そのようなノイズの性質は、ソフトガンマリピーターのバーストの統計を説明するのに好都合である。

日本原子力研究所（東海駐在): 〒 319-1195 茨城県那珂郡東海村白方白根 2-4

Contents

目　　　次

1. Introduction: Soft Gamma Repeaters and Anomalous X-ray Pulsars as Magnetars

Ultramagnetized neutron stars ('magnetars') have been invoked to interpret several astrophysical phenomena associated with an activity of Soft Gamma Repeaters (SGRs) and Anomalous X-ray Pulsars (AXPs). Such high-energy astrophysical sources display persistent X-ray luminosities $L_X \sim 10^{34.5} - 10^{36}$ erg/s which are considerably smaller than the Eddington limit $L_{Edd} \approx 10^{38}(M_{NS}/M_\odot)$ erg/s (see, e.g., Shapiro & Teukolsky 1983). However, the applicability of an accretion model (Chatterjee, Hernquist & Narayan 2000, Chatterjee & Hernquist 2000) to these objects meets serious difficulties (Li & Wang 2000). The observed periods and period derivatives of SGR 1806 + 20 (Kouveliotou et al. 1998) and SGR 1900 + 14 (Hurley et al. 1999, Hurley et al. 1999a, Kouveliotou et al. 1999, Murakami et al. 1999) , and AXPs 1E 1841+045 (Gotthelf, Vasisht & Dotani 1999) and 1E 2259+586 (Kaspi, Chakrabarty & Steinberger 1999) yield large values, up to 10^{15} G, for the strength of dipole-surface-field components when assuming a magnetic-braking spin-down mechanism. Some more involved models e.g. accounting for a loss of angular momentum due to a wind of particles require an order of magnitude smaller dipole fields (Harding, Contopoulos & Kazanas 1999, Marsden, Rothschild & Ligenfelter 1999) to explain such high spin-down rates. Nevertheless, observed properties of SGRs and AXPs strongly support the magnetar hypothesis (Duncan & Thompson 1992) suggesting an ultra-magnetized stellar media (with $B \sim 10^{17.5}$ G). Such a magnetization can be understood, e.g., as an effect of the "dynamo action" process which might operate in fast rotating stars, or spontaneous magnetization of hadron liquid due to ferromagnetic exchange coupling (Tatsumi 2000).

It is worth noticing here that the surface magnetic field does not necessarily reflects the strength of interior fields (Ruderman, Zhu & Chen 1998, Thompson & Duncan 1995, 1996). For instance, toroidal fields below the Sun surface are stronger than average surface dipole fields (~ 1 G) by at least a factor $10^2 - 10^4$ (Galloway, Proctor & Weiss 1977), an excess corresponding to an interior field strength $B \sim 10^{15} - 10^{18}$ G in neutron stars. The estimates based on an application of the Newtonian scalar virial theorem (cf. Lai & Shapiro 1991 and refs. therein) in conjunction with more involved numerical calculations (see, e.g., Duncan & Thompson 1992, Cardall, Prakash & Lattimer 2001, Thompson & Murray 2001) further corroborate the assertion of a possibility for ultra-high stellar magnetic fields. Indeed, the multipeaked pulse profile in the tail of the 1998 August 27 flare and following August 29 event (afterglow) of SGR 1900+14 gives an evidence (Thompson et al. 2000, Ibrahim et al. 2001, Feroci et al. 2001) for essentially multipolar geometry of surface fields with high order multipoles plausibly stronger than the respective dipole component $B_d \sim 10^{14.5}$ G. The energy associated with such super-strong fields dominates the star free energy and powers the magnetar emission. Actually, the change

of the persistent X-ray flux suggests the magnetic reconnections during the giant flare events (Woods et al. 2001).

Apart from mentioned above giant flares of a superhigh intensity $L_X \sim 10^{44.5}$ erg these sources more generally emit the short (~ 0.1 s) outbursts with super-Eddington luminosities $\sim 10^3 - 10^4 L_{Edd}$. Such burst emissions tend to concentrate into short intervals (weeks to months) of intense activity separated by relatively long (years) quasi-regular quiescent periods (Kouveliotou et al. 1998, see also Eq. (128) of sect. 9 and discussion therein). Many properties of SGR activity are well explained within 'magnetar' concept assuming that the emission of SGR bursts originates from the crust dynamics driven by the magnetic field (Thompson & Duncan 1995, 1996, Duncan & Li 1997, Duncan 1998). However, quasiperiodicities in SGR active phases in conjunction with rather stable (without noticeable spin-up glitches) spinning down provide arguments opposing the star-quake triggering mechanism of SGR bursts. Some alternative models have considered exotic processes, like collisions of a strange star with asteroids (Zhang, Xu & Qiao 2000, Usov 2001), or effects of boson condensate in superconducting core (Suh & Mathews 2001).

We argue in this paper that these properties of the bursts activity can be as well understood within the magnetar concept and they are consistent with burst triggering mechanism due to a release of magnetic energy stored in neutron star crusts. The periods of intense activity are related to the quantization induced step-like anomalies in magnetic field dependence of the magnetic moments of crust nuclides. At such conditions the demagnetization proceeds as erratic jumps associated with crust magnetic avalanches, similar to the Barkhausen effect (see, e.g., Feynman 1965 and sect. 5), and causes sharp energy release to the magnetosphere. Significant difference from the Barkhausen noise is the strongly magnetized system far from conditions of magnetization reversal. As demonstrated such model yields accurate quantitative description of the burst statistics during the active period which displays features of self-organized criticality, e.g., power law dependence of number of events on the intensity, lognormal distribution of waiting times between the bursts (Hurley et al. 1994, Göğüş et al. 1999, 2000).

Quantization of spatial motion naturally arises in the inhomogeneous crusty nuclear matter suggested by numerous theoretical studies (cf. Shapiro & Teukolsky 1983, Baym, Pethick & Sutherlan 1971, Haensel, Zdunik & Dobaczewski 1989, Oyamatsu & Yamada 1994, Pethick & Ravenhall 1995, Iida & Sato 1997, Maruyama et al. 1998, Heiselberg & Njorth-Jensen 2000 and refs. therein) at the density $\mathcal{D}$ less than the saturation density $\mathcal{D}_s$. An analysis of free-energy minima indicates that at the transition from a homogeneous neutron-proton-electron plasma to the solid crust with separated nuclides (at $\mathcal{D} < \mathcal{D}_s/3$) the ground state of nuclear matter is transformed to "neutron bubbles", "neutron tubes", "slabs" and "rods" which behave like liquid crystals (Pethick & Potekhin 1998).

As shown recently by Kondratyev, Maruyama, & Chiba (1999, 2000, 2000a, 2001, 2001a)

the structure of neutron star envelopes and the nuclide composition can depend on the magnetic field (see also Kondratyev 2001a). Such an effect originates from the modification of shell-oscillations in the nuclear level density (and, consequently, the masses of atomic nuclei) under an influence of magnetic fields, similarly to atomic clusters and quantum dots (cf. Kondratyev & Lutz 1998, 1999 and refs. therein).

This paper represents an extensive study of magnetic response of nuclear matter at various densities. We develop the thermodynamic formalism (next section) to analyze magnetic reactivity of a system with strong interaction in varying magnetic field. Particular attention is paied for quantization effects due to , e.g., confinement of spatial motion. As demonstrated in sect. 4 the quantization of nucleon levels gives rise to abrupt sharp change of nuclear magnetization in strong magnetic fields. We focus on an analysis of light and medium mass nuclei with mass numbers up to the iron region, where the simplified version of the Nilsson model (NM) can be employed (see Ring & Schuck 1980, Nilsson & Ragnarsson 1990). For these systems the step-like change of, e.g., nuclear magnetic moment arises at the level crossing. As shown in sects. 5, 6, and 7 for realistic system such anomalies in conjunction with magnetic coupling give rise to critical behavior with specific features of magnetic Equation of State. As a consequence, magnetodynamics of 'magnetar' crusts exhibits irregular jumps of the magnetization. The statistics of such a noise is analyzed in sect. 8. As illustrated in sect. 9 the magnetic noise properties at critical conditions are favorably compared to the SGR burst activity.

The principal results of the present study and possible perspectives are discussed in sect. 10.

2. Magnetic Response of Nuclear Matter within Thermodynamic Formalism

As specified in sect. 1 present study focuses on the magnetic field range $H \sim 10^{15} - 10^{18}$ G when one can apply a non-relativistic description of nucleons. Relativistic effects become important when the particle cyclotron energy $\omega_{cp} = 2\omega_L = 2\mu_N H$ ($\mu_N = e\hbar/2m_p c \approx 3.15 \cdot 10^{-18}$ MeV·G^{-1} is the nuclear magneton) is comparable to its rest mass (times c^2). The magnitude of the so-called critical field for nucleons $H_c^N = m_p c^2/2\mu_N \approx 1.487 \cdot 10^{20}$ G corresponds to a flux $\Phi_0 = \hbar c/\pi e$ through the area of a radius given by the nucleon Compton wavelength $\hbar/(m_p c) \approx 0.21$ fm. These fields may affect conditions of the β-equilibrium of the neutron star bulk matter (Broderick, Prakash & Lattimer 2000). They are significantly larger of mentioned above range of strengths which are related to respective flux associated with an area covered by the nuclear size (Kondratyev, Maruyama & Chiba 1999, 2000). We note, however, that the respective critical field for electrons $H_c^e = (m_e/m_N)^2 H_c^N \approx 4.414 \cdot 10^{13}$ G implies an importance of respective relativistic effects (cf., e.g., Broderick, Prakash & Lattimer 2000).

2.1. Observables versus Thermodynamic Potentials

The magnetic response of nuclear matter can be described in terms of the magnetic susceptibility which is convenient to define within the thermodynamic formalism. At a chemical equilibrium the relevant thermodynamic function is given by the grand canonical potential (GCP) Ω which represents the logarithm of the grand canonical partition function $\mathcal{Z}$

$$\Omega = -T \cdot \ln \mathcal{Z}, \quad \mathcal{Z} = \mathrm{Tr}(\exp\{-(\hat{\mathcal{H}} - \sum_{N=n,p} \hat{N}_N \lambda_N)/T\}) , \tag{1}$$

where the total Hamiltonian $\hat{\mathcal{H}}$, the nucleon number operators $\hat{N}_N$, the chemical potentials λ_N for neutrons (N = n) and protons (N = p), and the temperature T provide the description of a system. We recall that GCP per occupied volume V gives the measure of a pressure $P = \Omega/V$.

At statistical equilibrium the magnetic moment of a system is given by the thermodynamic relation

$$M = -\left(\partial\Omega/\partial H\right)_{T,\lambda} . \tag{2}$$

In the following we also consider the magnetization $\mathcal{P} = M/V$. The magnetic susceptibility is defined by

$$\chi = (1/V)\left(\partial M/\partial H\right)_{T,\lambda} = -(1/V)\left(\partial^2\Omega/\partial H^2\right)_{T,\lambda} . \tag{3}$$

When the number of nucleons N_N (or density $\mathcal{D}_N = N_N/V$)

$$N_N = -\frac{\partial\Omega}{\partial\lambda_N} \tag{4}$$

is fixed the system is described in terms of canonical ensemble. The respective thermodynamic function is represented by the free energy

$$F \approx \sum_{N=n,p} N_N \lambda_N + \Omega , \tag{5}$$

while the magnetization and susceptibility are given by respective derivatives.

2.2. Shell Effects within the Mean-Field Treatment

Within the Hartree mean-field treatment the description of a system is reduced to a single-particle (sp) representation, when the nuclear structure is determined by sp Hamiltonians

$$\hat{h}_N = \frac{\hat{\mathbf{p}}_N^2}{2m_N} + V_N(\mathbf{r}) + V_{so}(\mathbf{r}) + \delta h_N^m \tag{6}$$

which include the kinetic energy (first term of the rhs) with the nucleon momentum $\hat{\mathbf{p}}_N$ and mass m_N, the mean-field (i.e. the confining potential $V_N(\mathbf{r})$) and the spin-orbit

interaction,

$$V_{so}(\mathbf{r}) = -\zeta\Big(\hat{\mathbf{s}}\cdot[\partial_\mathbf{r}V_N\times\hat{\mathbf{p}}_N]\Big)\hbar/2(m_Nc)^2 .\tag{7}$$

Here the components of the spin operator $\hat{\mathbf{s}}$ are given by the Pauli matrices, and the fitting parameter ζ depends on a mass number A. $[\cdot\times\cdot]$ denotes the vector product.

The magnetic field $\mathbf{B}$ gives rise to an additional term in the Hamiltonian

$$\delta h_N^m = -\mathbf{B}\hat{\mathcal{M}}_N + (\hat{\tau}_3 + 1/2)\delta h_\circ^m,\tag{8}$$

where the first term in the right hand side (rhs) of Eq. (8) represents an interaction of the field with the nucleon dipole-spin-magnetic moment $\hat{\mathcal{M}}_N = g_N\mu_N\hat{\mathbf{s}}$. Here g_N denotes the nucleon Lande g-factor. $g_n = -3.8263$ for neutrons and $g_p = 5.5856$ for protons, the second term is related to the orbital magnetism of protons due to the Coulomb charge. Incorporating this interaction as a shift of the momentum $\mathbf{p} \to \mathbf{p} + \mathbf{A}\cdot e/c$ with a field vector potential $\mathbf{A} = [\mathbf{B}\times\mathbf{r}]/2$ leads to the form

$$\delta h_\circ^m = \frac{m_p}{2}\omega_L^2 r_\perp^2 - \omega_L\hat{l}_3\tag{9}$$

with the proton spatial coordinate component perpendicular to the magnetic field $r_\perp$, and the operator of the orbital angular momentum projection on the direction of the field $\hat{l}_3$.

The sp level densities $\rho_N(\epsilon)$ can be introduced as

$$\rho_N(\epsilon) = \sum_\zeta \delta(\epsilon - \epsilon_\zeta^N)\tag{10}$$

for given sp eigen-energies ϵ_ζ^N with quantum numbers ζ of the sp Hamiltonian $\hat{h}_N$. Within such an approximation the GCP is simplified to be

$$\Omega_N = -T\int_{-\infty}^\infty d\epsilon\, \rho_N(\epsilon)\cdot\ln[1 + \exp\{(\lambda_N - \epsilon)/T\}].\tag{11}$$

Representing the level density in the form, $\rho_N = \rho_N^{sm} + \delta\rho_N$, with the smooth ρ_N^{sm} and the oscillating $\delta\rho_N$ parts of neutrons (N = n) and protons (N = p) we re-write the GCP as a sum of respective components

$$\Omega = \Omega_n + \Omega_p = \Omega^{sm} + \delta\Omega_n + \delta\Omega_p ,\tag{12}$$

where the smooth component Ω^{sm} is associated with the Thomas-Fermi (i.e. semi-classical) approximation for the nuclear structure and can be treated in terms of the Liquid Drop Model (LDM) (Ring & Schuck 1980), while $\delta\Omega_n$ and $\delta\Omega_p$ are shell-correction contributions of neutrons and protons, respectively.

The oscillating part of the free energy contains an additional term due to the fluctuations $\delta\lambda_N = \lambda_N - \lambda_N^{sm}$ of the chemical potential λ_N around its mean value λ_N^{sm}. Using Eqs. (4) and (11) the nucleon number is obtained to be

$$N_N(\lambda_N) = \int_{-\infty}^\infty d\epsilon\, \rho_N(\epsilon)\mathcal{F}(\epsilon - \lambda_N) = N_N^{sm}(\lambda_N) + \delta N_N(\lambda_N) ,\tag{13}$$

where the Fermi distribution function $\mathcal{F}(x) = 1/[1 + \exp\{x/T\}]$, while the smooth $N_{\mathrm{N}}^{\mathrm{sm}}(\lambda_{\mathrm{N}})$ and oscillating $\delta N_{\mathrm{N}}(\lambda_{\mathrm{N}})$ parts are related to the smooth and oscillating components of the level density, respectively. The upper limit of $\delta N_{\mathrm{N}}(\lambda_{\mathrm{N}})$ is given by the level degeneracy which is the highest for the spherical Harmonic Oscillator (HO) yielding $\delta N_{\mathrm{N}}(\lambda_{\mathrm{N}})^{\mathrm{max}} \leq (n_{\mathrm{F}} + 1)(n_{\mathrm{F}} + 2)$. The principal quantum number of the Fermi level n_{F} is determined by the number of nucleons $N_{\mathrm{N}} = (1 + n_{\mathrm{F}})(2 + n_{\mathrm{F}})(1 + n_{\mathrm{F}}/3)$.

The mean chemical potential $\lambda_{\mathrm{N}}^{\mathrm{sm}}$ is defined by the condition of accommodating N_{N} nucleons to the smooth level density $\rho_{\mathrm{N}}^{\mathrm{sm}}$

$$N_{\mathrm{N}} = N_{\mathrm{N}}(\lambda_{\mathrm{N}}) = N_{\mathrm{N}}^{\mathrm{sm}}(\lambda_{\mathrm{N}}^{\mathrm{sm}}) . \tag{14}$$

As seen from Eqs. (13) and (14) the relative value of fluctuations $\delta\lambda_{\mathrm{N}}/\lambda_{\mathrm{N}}$ is of the same order as the ratio $\delta N/N$ with an upper limit $(1 + n_{\mathrm{F}}/3)^{-1} \approx N^{-1/3}$ (see above). Furthermore, at a finite temperature the exponential suppression of oscillating components (i.e. the factor R in sect. 4 and Appendix A) lowers additionally quantum fluctuations which are washed out at $T \gtrsim \omega/\pi$. For stable nuclei of average mass numbers this estimate gives very large temperature $T \sim 1$ MeV. At small temperatures the estimate of the suppression factor $R \approx 1 - (k2\pi^2 T/\omega)^2/6$ indicates a stronger suppression for higher harmonics k in an expansion of oscillating GCP (see sect. 4).

Thus for sufficiently large systems canonical corrections to the free energy can be evaluated perturbatively. In a linear order in $\delta N/N$ Eq. (14) leads to

$$\delta\lambda_{\mathrm{N}} = \lambda_{\mathrm{N}} - \lambda_{\mathrm{N}}^{\mathrm{sm}} \approx -\delta N_{\mathrm{N}}(\lambda_{\mathrm{N}}^{\mathrm{sm}})/\rho_{\mathrm{N}}^{\mathrm{sm}}(\lambda_{\mathrm{N}}^{\mathrm{sm}}) . \tag{15}$$

We have used here an approximation $N_{\mathrm{N}}^{\mathrm{sm}}(\lambda_{\mathrm{N}}^{\mathrm{sm}}) - N_{\mathrm{N}}^{\mathrm{sm}}(\lambda_{\mathrm{N}}) \approx -(\partial N_{\mathrm{N}}^{\mathrm{sm}}/\partial\lambda_{\mathrm{N}})\delta\lambda_{\mathrm{N}}$ and $\partial N_{\mathrm{N}}^{\mathrm{sm}}/\partial\lambda_{\mathrm{N}} = \rho_{\mathrm{N}}^{\mathrm{sm}}$.

Expanding the relation Eq. (5) to a second order in $\delta\lambda_{\mathrm{N}}$ we get

$$F_{\mathrm{N}} \approx (\lambda_{\mathrm{N}}^{\mathrm{sm}} + \delta\lambda_{\mathrm{N}})N_{\mathrm{N}} + \Omega(\lambda_{\mathrm{N}}^{\mathrm{sm}}) - N_{\mathrm{N}}(\lambda_{\mathrm{N}}^{\mathrm{sm}})\delta\lambda_{\mathrm{N}} - \mathcal{R}_{\mathrm{N}}\delta\lambda_{\mathrm{N}}^2/2. \tag{16}$$

Here we have taken into account Eqs. (4) and introduced the "thermally smoothed" level density according to the relation

$$\partial N_\alpha/\partial\lambda_\alpha = \mathcal{R}_\alpha . \tag{17}$$

Using decompositions of $\Omega(\lambda_{\mathrm{N}}^{\mathrm{sm}})$ and $N(\lambda_{\mathrm{N}}^{\mathrm{sm}})$ on the smooth and oscillating parts and eliminating $\delta\lambda_{\mathrm{N}}$ (i.e. Eq. (15)) in the second order term we obtain an expansion of the free energy to the second order in $\delta N/N$ as

$$F_{\mathrm{N}} \approx F_{\mathrm{N}}^0 + \delta F_{\mathrm{N}}^1 + \delta F_{\mathrm{N}}^2 \tag{18}$$

with

$$F_{\mathrm{N}}^0 = \lambda_{\mathrm{N}}^{\mathrm{sm}} N_{\mathrm{N}} + \Omega^{\mathrm{sm}}(\lambda_{\mathrm{N}}^{\mathrm{sm}}), \tag{19}$$

$$\delta F_N^1 = \delta\Omega(\lambda_N^{sm}), \tag{20}$$

$$\delta F_N^2 = [\delta N_N(\lambda_N^{sm})]^2/2\rho^{sm}. \tag{21}$$

In the semiclassical regime (i.e. to the leading order in $\hbar$) $N_N^{sm}(\lambda_N^{sm})$, λ_N^{sm} and $\Omega^{sm}(\lambda_N^{sm})$ remain constants as a function of the magnetic field. Therefore, F_N^0 represents the field independent component of the free energy regardless of considered system.

As we see from Eqs. (20) and (21) at a finite temperature the canonical correction δF_N^2 is exponentially suppressed as compared to the leading term δF_N^1. Since the case of a high temperature can be identified as a classical limit the term δF_N^1 can be considered as a leading quantum correction term which depends on the magnetic field. Therefore at a finite temperature within the semiclassical accuracy the magnetism of a canonical ensemble is determined by the term δF_N^1 which is just given by the oscillating part of the grand canonical potential at a mean chemical potential. The first canonical correction δF_N^2 has a grand canonical form since it is expressed in terms of a temperature smoothed integral of the level density for a fixed chemical potential. As shown by Kondratyev, Maruyama & Chiba (2000,2001) the first canonical correction corresponds to nearly 10% contribution which we neglect in calculations.

At zero temperature the GCP reduces to a grand potential Ω_N^0 which is expressed as

$$\Omega_N^0 = \Omega_N|_{T\to 0} = \int_{-\infty}^{\epsilon_F} d\epsilon\, (\epsilon - \epsilon_F)\, \rho_N(\epsilon)\,, \tag{22}$$

where the Fermi energy ϵ_F represents the chemical potential at $T = 0$. The oscillating part of the free energy of nuclei Eq. (5) at zero temperature

$$\delta E_N = \delta F_N|_{T\to 0} = \int_{-\infty}^{\epsilon_F} d\epsilon\, \epsilon\, \delta\rho_N(\epsilon) \tag{23}$$

is usually referred for as the shell-correction energy.

We note the relations

$$\Omega = -\int_{-\infty}^{\infty} d\epsilon\, \mathcal{F}'(\epsilon - \lambda)\Omega^0(\epsilon), \tag{24}$$

$$F = -\int_{-\infty}^{\infty} d\epsilon\, \mathcal{F}'(\epsilon - \lambda)E(\epsilon), \tag{25}$$

$$N = -\int_{-\infty}^{\infty} d\epsilon\, \mathcal{F}'(\epsilon - \lambda)N^0(\epsilon), \tag{26}$$

$$\mathcal{R} = -\int_{-\infty}^{\infty} d\epsilon\, \mathcal{F}'(\epsilon - \lambda)\rho(\epsilon), \tag{27}$$

where the energy derivative of the Fermi distribution function $\mathcal{F}'(\epsilon) = \mathcal{F}(\epsilon)[1 - \mathcal{F}(\epsilon)]/T = (4T\cosh(\epsilon/2T))^{-1}$. Note that in the vicinity of a maximum this function is well fitted by $[\exp\{-\epsilon^2/5T^2)/4T]$. We have introduced zero temperature nucleon number N^0.

Making use of the equality

$$dN^0/d\epsilon = \rho(\epsilon) \tag{28}$$

and integrating Eq. (11) by parts we find

$$\Omega_N = -\int_{-\infty}^{\infty} d\epsilon \; N_N^0(\epsilon)\mathcal{F}(\epsilon - \lambda). \tag{29}$$

Furthermore, assuming the condition

$$N^0(\epsilon) = \epsilon\rho(\epsilon)/\kappa \tag{30}$$

with a constant κ and employing the relation Eq. (28) we derive a general solution $N^0(\epsilon) = C\epsilon^\kappa$, representing a form which is often met for smooth level density components. For instance, for the case of Harmonic Oscillator $\kappa = 3$, while square well potential corresponds to $\kappa = 3/2$. Then one can readily see that at such condition the GCP is expressed in terms of a total energy

$$\Omega_N = -\kappa\int_{-\infty}^{\infty} d\epsilon \; \epsilon\rho_N(\epsilon)\mathcal{F}(\epsilon - \lambda) = -C \; T^{\kappa+1} \; I_\kappa(\lambda/T), \tag{31}$$

where the Fermi integrals

$$I_\nu(z) = \int_0^\infty \frac{x^\nu dx}{\exp\{x - z\} + 1} \tag{32}$$

are discussed in Appendix B.

After the pioneering works by V.M. Strutinsky (1967, 1968) the shell-correction approach has been successfully applied for the description of ground state binding energies of nuclei with various shapes and compared to the Hartree-Fock calculations (cf. e.g. Ring & Schuck 1980, Nilsson & Ragnarsson 1990 for review and Möller et al. 1995, Brack, Reimann & Sieber 1997, Vertse et al. 1998 for recent developments). Such a case clearly corresponds to the canonical ensemble at zero temperature.

The picture of a grand canonical ensemble is well suited for a system at chemical equilibrium, especially, for an inner crust with nuclides abutted by a neutron liquid. Therefore, in present paper we concentrate on a study of the magnetic field dependence of the leading semiclassical term δF^1 in the free-energy expansion. We note, that in cases of spherical HO (Kondratyev, Maruyama & Chiba 1999, 2000, 2000a) and the uniform Fermi liquid (see sect. 3) the correction terms arising from the nucleon number conservation (i.e. canonical corrections) contributes less than 20% to the total shell-correction energy and do not affect qualitative results. Thermal effects reduce further canonical corrections. We note, however, that the envelope temperature is relatively low ($\sim 10^6 - 10^{7.5}$ K, see Tsuruta 1998, Schaab, Weber & Weigel 1998, Heiselberg & Njorth-Jensen 2000) even assuming SGRs as an early phase of magnetars (i.e. relatively young stars $\sim 10^3 - 10^4$ y).

3. Uniform Neutron Star Matter

The uniform neutron star matter is predicted (see, e.g., Heiselberg & Njorth-Jensen 2000) for over-saturated nuclear densities $2\mathcal{D}_s \gtrsim \mathcal{D} \gtrsim \mathcal{D}_s$ with predominant concentra-

tion of neutrons, while the proton-electron component contributes of order of a percent. Therefore, we first analyze the magnetism of the neutron bulk as an example of the Fermi liquid magnetic response.

3.1. Neutron Paramagnetism

The neutrons exhibit only the Pauli-type of the magnetization since they are neutral particles and their orbital motion is not affected by the magnetic field. Such a magnetization is simply related to the relative shift $\sigma_i \Delta_n$

$$\Delta_n = -g_n \omega_L/2 \tag{33}$$

of energy levels with neutron spins directed along the field (spin-up: $\sigma_{i=\uparrow} = 1$, minority-spin neutron levels) and in the opposite direction (spin-down $\sigma_{i=\downarrow} = -1$, majority-spin neutron levels). Here the quantity $\omega_L = \mu_N B$ gives the energy of the first proton Landau level.

The shift Eq. (33) modifies GCP and defines paramagnetic response properties. It is worthy to point out here that, in contrast to the Pauli-magnetism of bulk electrons exhibiting the paramagnetic response with spins directed preferably along the field, the neutrons display the magnetization with the spin alignment reversed to the magnetic field vector. Such a behavior of the magnetic response of the neutron bulk is caused by the negative value of the neutron gyromagnetic ratio. It is therefore energetically favorable in the magnetic field the formation of a state with the number of spin-down neutrons ($N_{n\downarrow}$) exceeding the number of spin-up neutrons ($N_{n\uparrow}$).

The field dependent neutron contribution to GCP is given by

$$\Omega_n = \Omega_{n\downarrow} + \Omega_{n\uparrow} \approx [\Omega_n^0(\lambda_n - \Delta_n) + \Omega_n^0(\lambda_n + \Delta_n)]/2, \tag{34}$$

where Ω_n^0 is the neutron part of GCP at zero field.

Using Eqs. (2) and (4) and accounting for the relation $\left(\partial\Omega/\partial H\right) = \left(\partial\Omega/\partial\lambda_n\right) \cdot \left(\partial\lambda_n/\partial H\right)$ we obtain the neutron magnetic moment as

$$M_n = \frac{1}{2} g_n \mu_N \mathcal{N}, \tag{35}$$

where

$$\mathcal{N} = N_{n+} - N_{n-}$$

gives the difference in numbers of ($N_{n+} = N_n(\lambda_n + \Delta_n) = N_{n\downarrow}$) majority- and ($N_{n-} = N_n(\lambda_n - \Delta_n) = N_{n\uparrow}$) minority-spin neutrons (see Eqs. (13) and (34)). Since for a uniform matter $\rho_n = V m_n p_n/2\pi^2\hbar^3$ (with $p_n = \sqrt{2m_n\epsilon}$) neutron numbers are given by expressions

$$N_{n\pm} = N_n(\lambda_n \pm \Delta_n) = \frac{V m_n^{3/2}}{\sqrt{2}\pi^2\hbar^3} \int_0^\infty d\epsilon \sqrt{\epsilon} \cdot \mathcal{F}(\epsilon - \lambda_n \mp \Delta_n)$$
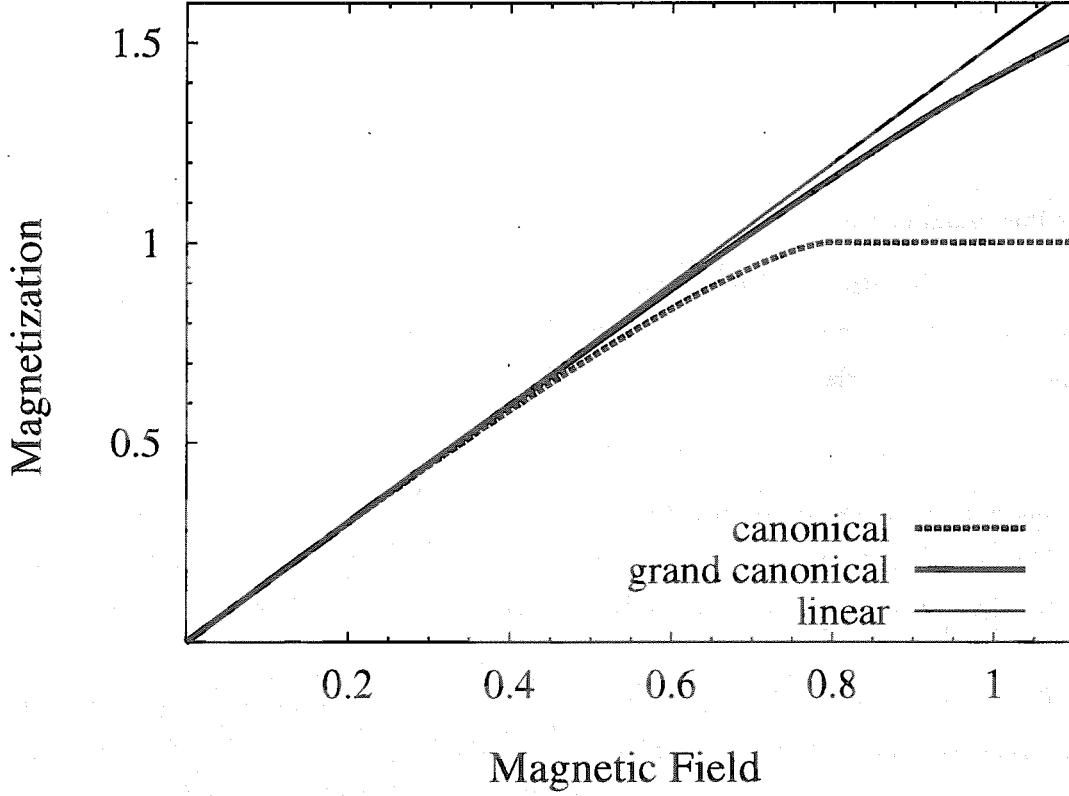
Fig. 1.— Magnetization in units of $\mathcal{P}_{ns}$, i.e. Eq. (40), of the neutron bulk matter versus magnetic field measured in $(2\epsilon_F/g_n\mu_N)$.

$$= \frac{V(m_n T)^{3/2}}{\sqrt{2}\pi^2\hbar^3} I_{1/2}(\lambda_n/T) = V\mathcal{D}_{n\pm}, \qquad (36)$$

where the Fermi integrals $I_\nu(z)$ are defined by Eq. (32).

Using Eqs. (3) and (35) we write the neutron magnetic susceptibility as

$$\chi_n = (1/V)(g_n\mu_N/2)^2 [\mathcal{R}_n(\lambda_n - \Delta_n) + \mathcal{R}_n(\lambda_n + \Delta_n)] . \qquad (37)$$

In zero temperature limit $(T \to 0)$ only the first term of the expansion Eq. (B5) contributes to the Fermi integration. Then Eqs. (36) and (37) are further reduced to

$$N_{n\pm} = \frac{V\sqrt{2}m_n^{3/2}}{3\pi^2\hbar^3} [\epsilon_F \pm \Delta_n]^{3/2} \qquad (38)$$

$$\chi_n = (g_n\mu_N)^2 \frac{\sqrt{2}m_n^{3/2}}{4\pi^2\hbar^3} \left[\sqrt{\epsilon_F + \Delta_n} + \sqrt{\epsilon_F - \Delta_n}\right] \qquad (39)$$

The number of minority-spin neutrons vanishes at fields $H > H_F \approx 1.5\epsilon_F/(g_n\mu_N)$ for canonical, and $H > H_{Fg} \approx 2\epsilon_F/(g_n\mu_N)$ for grand canonical ensembles, respectively. Such a condition of complete neutron spin-polarization at saturated nuclear density corresponds to relatively large fields $H_F \approx 10^{18.5}$ G which is consistent with respective evaluation by Broderick, Prakash & Lattimer (2000). The saturated magnetization of canonical
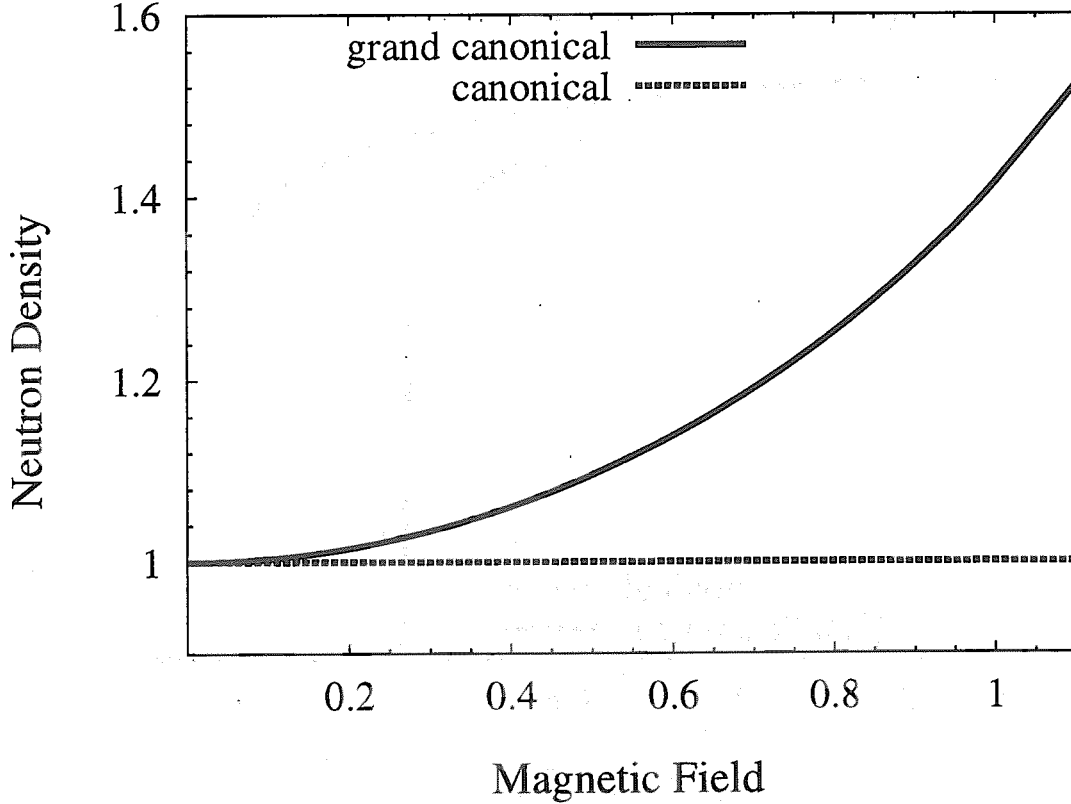
Fig. 2.— Density in units of $\mathcal{D}_n$ of the neutron bulk matter versus magnetic field given in $(2\epsilon_F/g_n\mu_N)$.

ensemble remains a constant [1] (see fig. 1)

$$\mathcal{P}_{ns} = g_n\mu_N\mathcal{D}_n/2 \approx 10^{16} \text{ Oe}. \tag{40}$$

This results in an abrupt behavior of the magnetic susceptibility at saturation fields $H = H_F$ as seen in fig. 3. The grand canonical ensemble magnetization increases further at over-saturation fields because of growing neutron density. As shown in fig. 2 such a density increase is noticeable at over-saturation fields, while the change is negligible for small fields. The complete neutron polarizability is displayed in this case as a discontinuity in the magnetic susceptibility at $H = H_{Fg}$, see fig. 3.

As seen in fig. 1 at undersaturation fields the canonical and grand canonical calculations yield very similar results with a difference of a couple of percent at canonical-saturation fields. Thus the mentioned in sect. 2.2 estimates for the difference between grand canonical and canonical ensembles are supported by numerical calculations. The magnetic response of the neutron bulk exhibits a linear regime for a wide range of the field strengths. Some nonlinearity arises at nearly saturation fields. Such a behavior can be clearly seen on the field dependence of the magnetic susceptibility displayed in fig. 3. As shown the nonlinear effects contributes less than 20 % for the entire interval of the field strength.

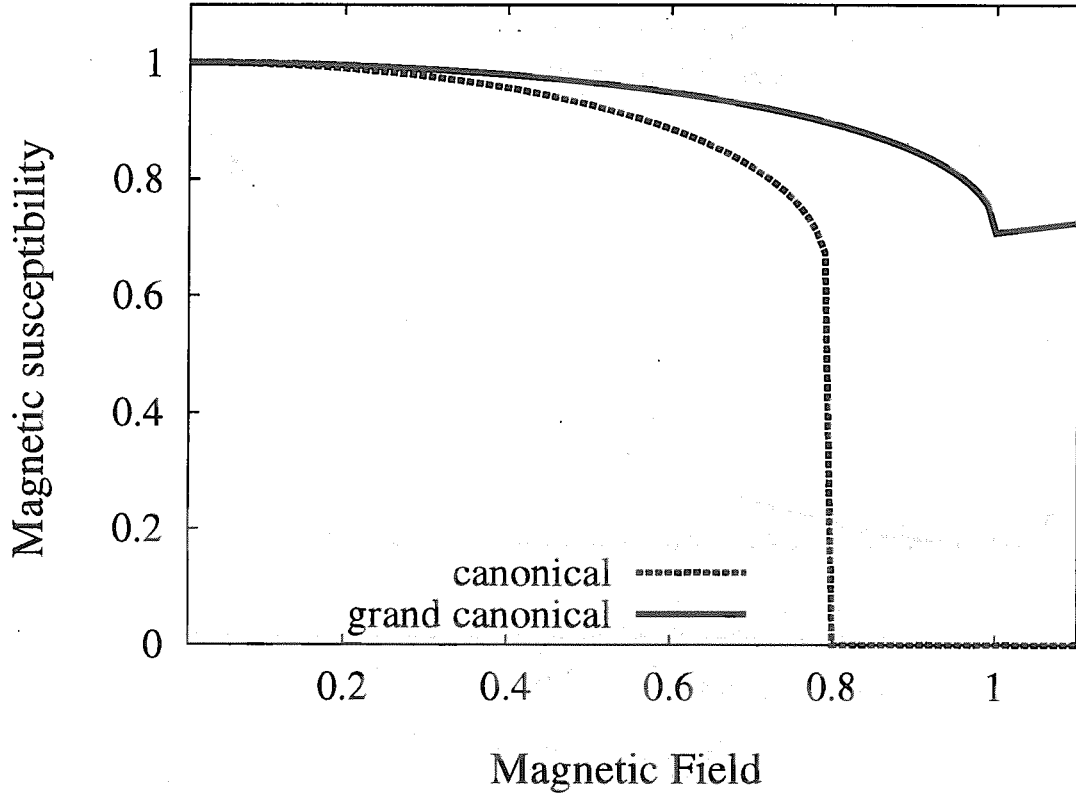[1] Estimate is given for normal nuclear density D_s.

Fig. 3.— Magnetic susceptibility measured in units of χ_n^0 given by Eq. (41) of the neutron bulk matter versus magnetic field presented in $(2\epsilon_F/g_n\mu_N)$.

In the linear regime of the magnetic response (i.e. at $H \lesssim H_F$) the neutron magnetic susceptibility is easily calculated from Eq. (39) to give a constant

$$\chi_n^0 = (g_n\mu_N)^2 \frac{m_n p_n}{2\pi^2 \hbar^3} \approx 10^{-3}\mathcal{D}_n^{1/3} \cdot \text{fm} \tag{41}$$

which is nearly an order of magnitude smaller than the familiar (cf. Landau & Lifshitz 1985) Pauli magnetic susceptibility of an electron gas of the same density as the neutron density $\mathcal{D}_n$.

We note finally that the contribution to the magnetic response of the proton component can be considered in terms of the magnetic impurities.

4. Crusty Neutron Star Matter

The proton concentration grows in importance at sub-saturated nuclear densities, when the structure of neutron star matter becomes noticeably inhomogeneous (see Shapiro & Teukolsky 1983, Baym, Pethick & Sutherlan 1971, Haensel, Zdunik & Dobaczewski 1989, Oyamatsu & Yamada 1994, Pethick & Ravenhall 1995, Iida & Sato 1997, Maruyama et al. 1998, Heiselberg & Njorth-Jensen 2000 and refs. therein). At relatively large densities $\mathcal{D} \lesssim \mathcal{D}_s$ the nuclear matter is predicted to transform from a uniform liquid to the structures containing spherical and cylindrical 'bubbles'. With further decreasing

densities the neutron liquid is filled by slabs, rods and, finally, bcc lattice of spherical nuclei. However, some recent studies by Watanabe, Iida & Sato (2000, 2001) suggest that the two 'inside-out' and the slab phases might be missing because of thermal fluctuations. Furthermore, as pointed out by Douchin, Haensel & Meyer (2000) at some choice of the nuclear interaction no exotic phases show up in the crust if one accounts for nuclear curvature energy. One of the most recent studies by Bulgac & Magierski (2001) suggests that accounting for the shell-correction type of energy in such structures may lead to a mixture of several types of shapes at the same density. In proceeding section we consider the magnetic response of a primitive element of such phases.

4.1. Nonspherical Inner Crust Structures

We consider in this section the magnetism of slabs as an example of the non-spherical nuclear configuration.

4.1.1. Proton Orbital Magnetism in 'Slabs'

In a slab-like structures the mean-field V_N is given by a periodic potential dependent only on one coordinate component, say x_3, and the s-o potential can be neglected (Baym, Pethick & Sutherlan 1971, Oyamatsu & Yamada 1994, Pethick & Potekhin 1998). Protons are confined in plates which are arranged periodically with a step a. The sp eigen-energies ϵ_{n3} are of a typical level spacing $\omega_{sl} \approx 4-5$ MeV (Oyamatsu & Yamada 1994) and an overlap between wave functions of the nearest neighbor plates can be neglected. For simplicity we assume at first that only one from such levels is occupied. The magnetic field gives an additional Hamiltonian Eq. (8). The first term of the rhs of Eq. (8) gives rise to the Pauli-spin magnetic response which has been discussed in sect. 3.1 for a case of 3 dimensions ($3D$).

We first consider an effect of the second term in the rhs of the Hamiltonian Eq. (8). At field strengths

$$H \ll H_{sl}, \qquad H_{sl} = \omega_{sl}/\mu_N \approx 10^{18} \text{ G} \tag{42}$$

eigen-states $|n_3>$ are not affected and the orbital magnetic response is determined by two dimensional motion localized in the plate. We can assume a simple geometry with the magnetic field perpendicular to the plate. Then the proton eigenstates are given by the Landau levels with eigen-energies (see Hamiltonian Eq. (9))

$$\varepsilon_n = \omega_L(2n+1), \qquad n = 0, 1, 2, \dots \tag{43}$$

and degeneracy Φ/Φ_0 for one *sort* of proton spin (i.e. up or down), $\Phi = HS$ gives the flux of field H through an area S, and the volume $V = Sa$. Making use of the Poisson summation formula the level density Eq. (10) associated with the spectrum Eq. (43) can

be decomposed into the smooth and oscillating parts

$$\rho_{\rm o}(\epsilon) = \frac{m_{\rm p}S}{2\pi\hbar^2}\Big(1 + 2\sum_{k=1}^{\infty}(-1)^k \cos\Big(\pi k\epsilon/\omega_{\rm L}\Big)\Big). \qquad (44)$$

Incorporating Eq. (44) into Eq. (13) and integrating over energy we obtain (see Appendix A) the proton density in the following form

$$\mathcal{D}_{\rm o} = \mathcal{D}_{\rm o}'\Big(1 + \frac{2}{\pi}\frac{\omega_{\rm L}}{\lambda_{\rm p}}\sum_{k=1}^{\infty}\frac{(-1)^k}{k}\sin\Big(\pi k\lambda_{\rm p}/\omega_{\rm L}\Big)R(kT/\omega_{\rm L})\Big), \qquad (45)$$

where zero field density of such two dimensional gas $\mathcal{D}_{\rm o}' = m_{\rm p}\lambda_{\rm p}/2\pi\hbar^2 a$, and $R(x) = \pi^2 x/\sinh(\pi^2 x)$ gives a thermal damping factor. Replacing such a factor R by p^k, $p \approx exp\{-\zeta\lambda_{\rm p}/\omega_{\rm L}\}$, the summation in Eq. (45) is calculated analytically to give

$$\sum_{k}\{...\} = -\arctg\Big(p\sin(\pi\lambda_{\rm p}/\omega_{\rm L})/(1 - p\cos\Big(\pi\lambda_{\rm p}/\omega_{\rm L}\Big))\Big).$$

As seen the quantum fluctuations of the proton density vanish at relatively large temperatures (with respect to the field strength), while at small temperatures the density displays discontinuities (i.e. step-wise behavior) at the Fermi energies corresponding to the closure of the Landau levels (cf. fig. 5 and discussion therein). In the limit of zero temperature the number of filled Landau levels is found as $\lambda_{\rm p}\mathcal{D}_{\rm o}/(\mathcal{D}_{\rm o}'\omega_{\rm L})$.

At relatively weak fields with respect to the crust temperature T ($\sim 10^2 - 10^{3.5}$ eV),

$$H \ll H_T, \qquad H_T = T/\mu_{\rm N} \approx 10^{13.5} - 10^{15}\ {\rm G}, \qquad (46)$$

the oscillating component is washed out yielding for e.g. an energy integration in Eq. (11) (with the level density Eq. (44)) the following result

$$\Omega_{\rm o} \approx \Omega_{\rm o}^{\rm sm} = -\frac{m_{\rm p}S}{2\pi\hbar^2}\frac{\lambda_{\rm p}^2}{2} + \frac{\mu_{\rm N}^2 m_{\rm p}}{6\pi\hbar^2}\frac{SH^2}{2}. \qquad (47)$$

Note that the second term in the rhs of Eq. (47) originates from an integration of the rapidly oscillating part of the level density Eq. (44). Using Eqs. (3) and (47) we obtain the proton Landau diamagnetic susceptibility to be

$$\chi_{\rm L} = -\frac{\mu_{\rm N}^2 m_{\rm p}}{3\pi\hbar^2 a} \approx -0.407\cdot10^{-4}\ {\rm fm}/a\ . \qquad (48)$$

The smooth component of the spin magnetic susceptibility can be calculated in a way similar to the case of the neutron bulk (see sect. 3.1). Since the smooth level density (see Eq. (44)) is given by a constant

$$\rho_{\rm p}^{\rm sm}(\epsilon) = \frac{m_{\rm p}S}{2\pi\hbar^2} \qquad (49)$$

the smooth Pauli magnetization exhibits a linear regime for a wider field range than those given by conditions Eq. (46). Infact, the grand canonical Pauli magnetic response is always linear with the value of the susceptibility

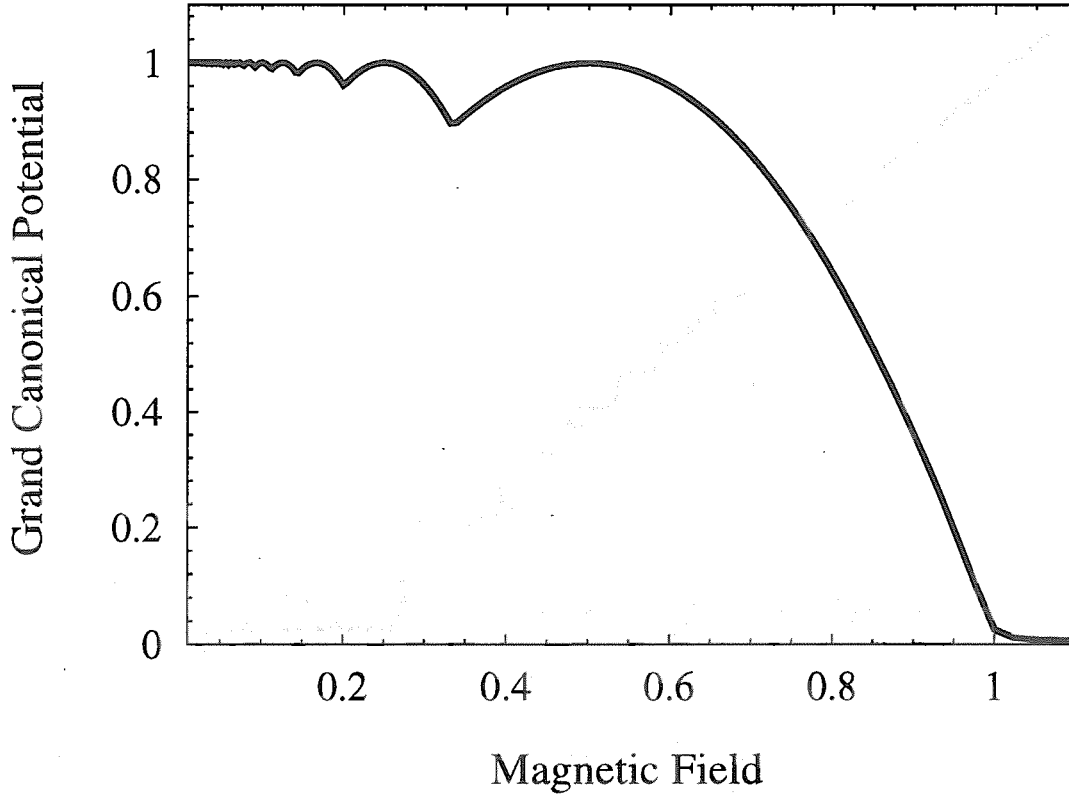$$\chi_{\rm p} = (g_{\rm p}\mu_{\rm N}/2)^2\frac{m_{\rm p}}{\pi\hbar^2 a} \approx 0.38\cdot10^{-2}\ {\rm fm}/a \qquad (50)$$

Fig. 4.— The proton grand canonical potential in units of (Ω_o^0), see Eq. (53), of a slab versus magnetic field in units of (λ_p/μ_N).

which is larger than respective orbital component Eq. (48) by a factor $3g_p^2$, i.e. nearly two orders of magnitude. At a period $a \approx 20$ fm this value of the susceptibility is slightly less than the respective quantity for bulk neutrons at normal nuclear density.

For large magnetic fields (i.e. at $\omega_L \gtrsim T$) the oscillating part of GCP is noticeable

$$\delta\Omega_o(\lambda_p) = \frac{m_p S}{\pi \hbar^2} \sum_{k=1}^{\infty} (-1)^k \left(\frac{\omega_L}{\pi k}\right)^2 \cos\left(\pi k \lambda_p/\omega_L\right) R(kT/\omega_L).$$ (51)

Note that the ratio $[\lambda_p/\omega_L]$-counts the number of occupied Landau levels (see Eq. (43)). This term displays characteristic oscillations with a period $\sim 1/H$. The change in the field strength $\Delta H = H_+ - H_-$ associated with a single oscillation corresponds to an increase by 1 in the number of occupied Landau levels. This leads to a change

$$\Delta H = H_+ H_- \mu_N/\lambda_p$$ (52)

which goes to zero at low field limit. The oscillation amplitude is defined by the relationship between the number of occupied Landau levels (increasing with decreasing H) and the thermal damping factor (exponentially suppressed at small H).

Thus combining Eqs. (47) and (51) the grand canonical potential of slab protons ac-
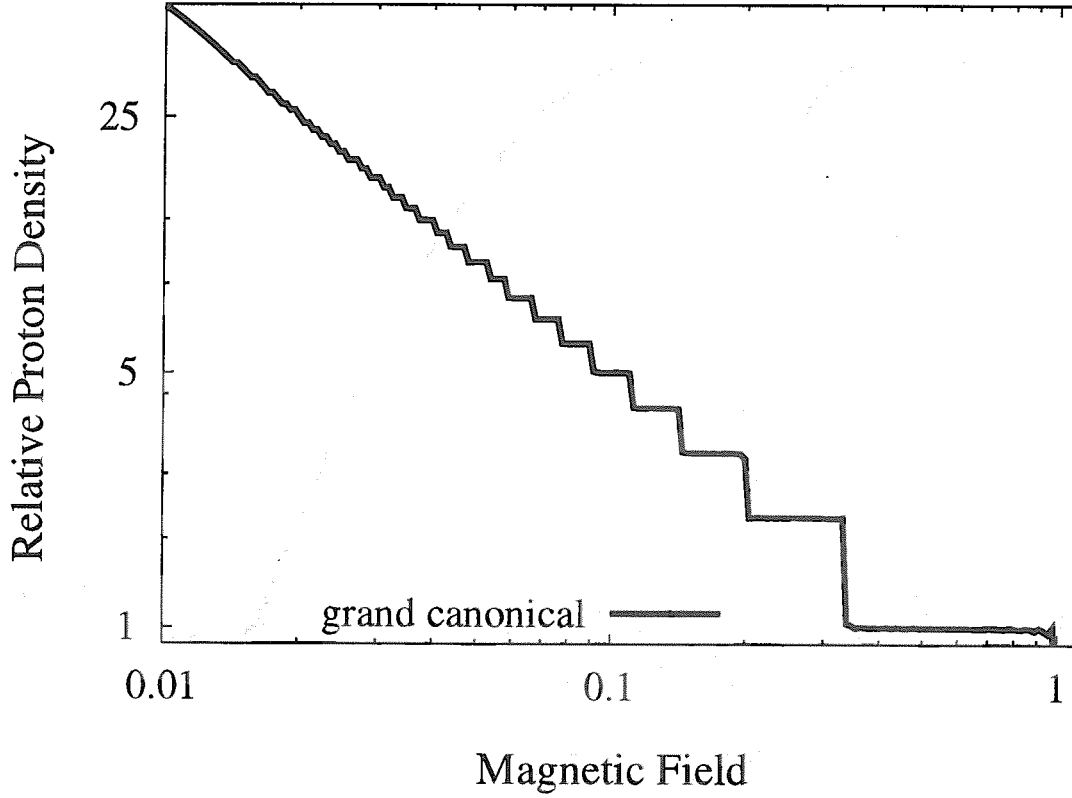
Fig. 5.— The proton relative density (indicating the number of the filled Landau levels) of a slab versus magnetic field in units of (λ_p/μ_N).

counting for the orbital dia-magnetism only reads

$$\frac{\Omega_o}{\Omega_o^0} = 1 - \frac{1}{3}\left(\frac{\omega_L}{\lambda_p}\right)^2 \left(1 + \frac{12}{\pi^2}\sum_{k=1}^{\infty}(-1)^k k^{-2}\cos\left(\pi k \lambda_p/\omega_L\right)R(kT/\omega_L)\right) \qquad (53)$$

with slab proton GCP at zero magnetic field Ω_o^0: $(\Omega_o^0/V) = -m_p\lambda_p^2/4\pi\hbar^2 a$. As seen in fig. 4 the relative proton contribution to the slab GCP (i.e. pressure) displays oscillations which are familiar for electron systems as the de Haas-van Alphen oscillations (Landau & Lifshitz 1985). Originating from Landau levels such a diamagnetic suppression increases as a square of the field strength. The minima in the magnetic field dependence of the slab proton GCP corresponds to a closure of the Landau levels, while the maxima are associated with a case of the half filled highest occupied level, similarly to the shell effect familiar for nuclear masses (see sect. 4.2.1).

The number of filled Landau levels is shown on fig. 5 as function of the magnetic field. We see that when the proton cyclotron frequency $\omega_L = \mu_N H$ exceeds the Fermi energy λ_p only the first Landau level is occupied. Consequently, above such saturation field strengths, i.e. $H > \lambda_p/\mu_N \sim 10^{19}$ G, the proton orbital contribution to the pressure vanishes. Such ultrahigh fields correspond, however, to very large magnetic pressure $F_H = H^2/8\pi = \Omega_o^0 \cdot 2a/r_p \sim 10^4\Omega_o^0$. Here the classical proton radius $r_p = e^2/m_p c^2 \approx 1.535 \cdot 10^{-3}$ fm.
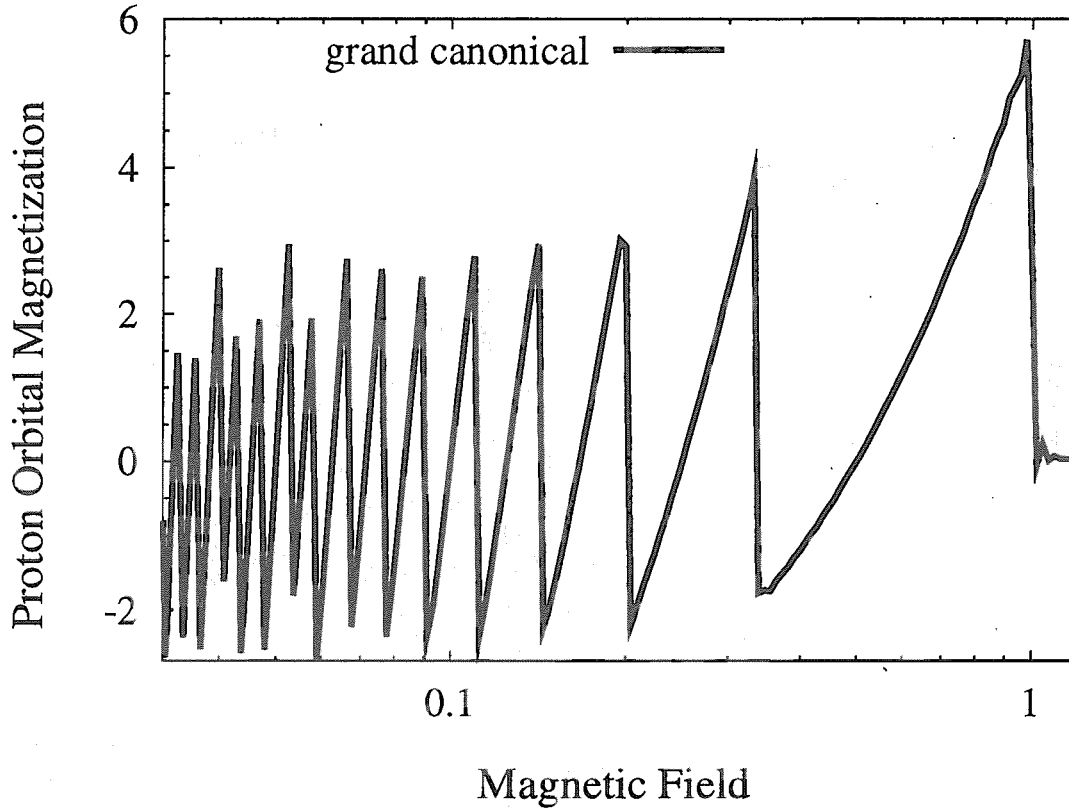
Fig. 6.— The proton orbital magnetization measured in $\mathcal{P}_{\mathrm{o}}^{0}$, see Eq. (54), of a slab versus magnetic field in units of $(\lambda_{\mathrm{p}}/\mu_{\mathrm{N}})$.

Using Eqs. (2) and (53) the orbital magnetization of a slab is given by

$$
\begin{aligned}
\frac{\mathcal{P}_{\mathrm{o}}}{\mathcal{P}_{\mathrm{o}}^{0}} &= \left(\frac{\omega_{\mathrm{L}}}{\lambda_{\mathrm{p}}}\right) + \frac{6}{\pi}\sum_{k=1}^{\infty}(-1)^{k}k^{-1}\left(\sin\left(\pi k\lambda_{\mathrm{p}}/\omega_{\mathrm{L}}\right)\right. \\
&+ \left.\frac{2\omega_{\mathrm{L}}}{\pi k\lambda_{\mathrm{p}}}\cos\left(\pi k\lambda_{\mathrm{p}}/\omega_{\mathrm{L}}\right)\right)R(kT/\omega_{\mathrm{L}}),
\end{aligned}
\tag{54}
$$

where $\mathcal{P}_{\mathrm{o}}^{0} = -\mu_{\mathrm{N}}m_{\mathrm{p}}\lambda_{\mathrm{p}}/6\pi\hbar^{2}a \approx 10^{14.5}$ G · fm/a.

As illustrated in fig. 6 the proton orbital magnetization displays rather sharp, abrupt change at the magnetic field strengths corresponding to a closure of the Landau levels. At the conditions $\omega_{\mathrm{L}} > \lambda_{\mathrm{p}}$ the orbital response vanishes. We note in this regards that for electrons respective saturation fields are relatively small $H_{e} = \lambda_{e}/\mu_{\mathrm{B}} \sim 10^{15.5}$ G, where the Bohr magneton $\mu_{\mathrm{B}} \approx 5.788 \cdot 10^{-15}$ MeV G^{-1}. Therefore, within the considered range of the field strengths we expect to find no step anomalies in electron magnetic response.

Bringing together smooth and oscillating parts the proton orbital magnetic susceptibility can be represented as the Landau and Haas-van Alphen contributions

$$
\frac{\chi_{\mathrm{po}}}{|\chi_{\mathrm{L}}|} = -1 - 6\left(\frac{\lambda_{\mathrm{p}}}{\omega_{\mathrm{L}}}\right)^{2}\sum_{k=1}^{\infty}(-1)^{k}\cos\left(\pi k\lambda_{\mathrm{p}}/\omega_{\mathrm{L}}\right)R(kT/\omega_{\mathrm{L}}).
\tag{55}
$$

Employing again a substitution $R(kT/\omega_{\mathrm{L}}) \to p^{k}$ the summation in Eq. (55) is calculated
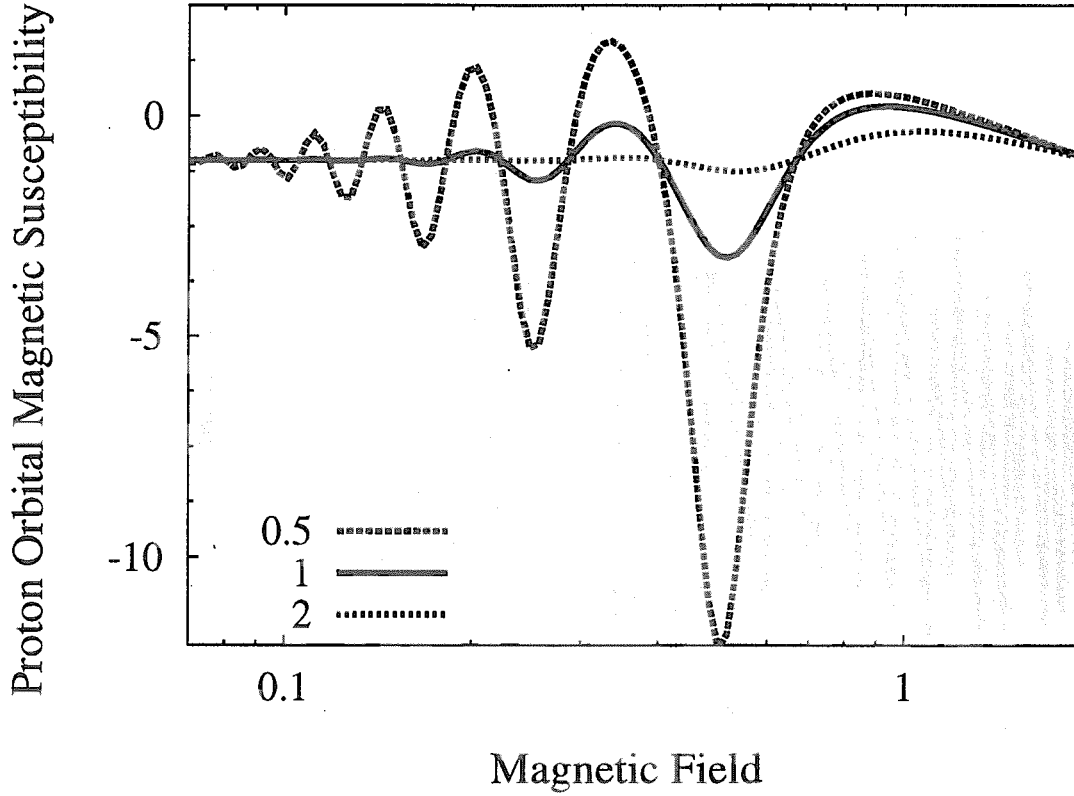
Fig. 7.— The proton orbital magnetic susceptibility in the units of zero-field proton diamagnetic suscep-
tibility $|\chi_L|$, see Eq. (55), of a slab versus magnetic field measured in units of (λ_p/μ_N).

analytically to give

$$\sum\{...\} = p\cos\left(\pi\lambda_p/\omega_L\right)/\left(1 - 2p\cos\left(\pi\lambda_p/\omega_L\right) + p^2\right).$$

This relation indicates that when $p \to 0$ the susceptibility is negatively defined and rep-
resented as a sum of δ-functions at the positions of the Landau level closures. With
increasing temperature such δ-peaks are smeared out. As shown in fig. 7 the oscillat-
ing part becomes almost invisible at large values of the parameter $\zeta \gtrsim 2$. Such a case
corresponds, however, to very large temperatures $T \gtrsim 1$ MeV.

4.1.2. Paramagnetism versus Orbital Magnetism

Including the first term of the rhs of Eq. (8) to the Hamiltonian switches on the Pauli-
spin magnetic reactivity, which we discussed in sect. 3.1 with respect to the neutron
magnetization. It is worthy to notice, however, that in contrast to the case of neutrons
the relative shift $\sigma_i \Delta_p$

$$\Delta_p = -g_p\omega_L/2 \tag{56}$$

of the proton energy levels corresponds to the down-shift of the majority-spin levels with
spins parallel to the field (spin-up, $\sigma_{i=\uparrow} = 1$) and the up-shift of the minority-spin proton
levels with spins antiparallel to the field direction (spin-down, $\sigma_{i=\downarrow} = -1$). Thus similarly
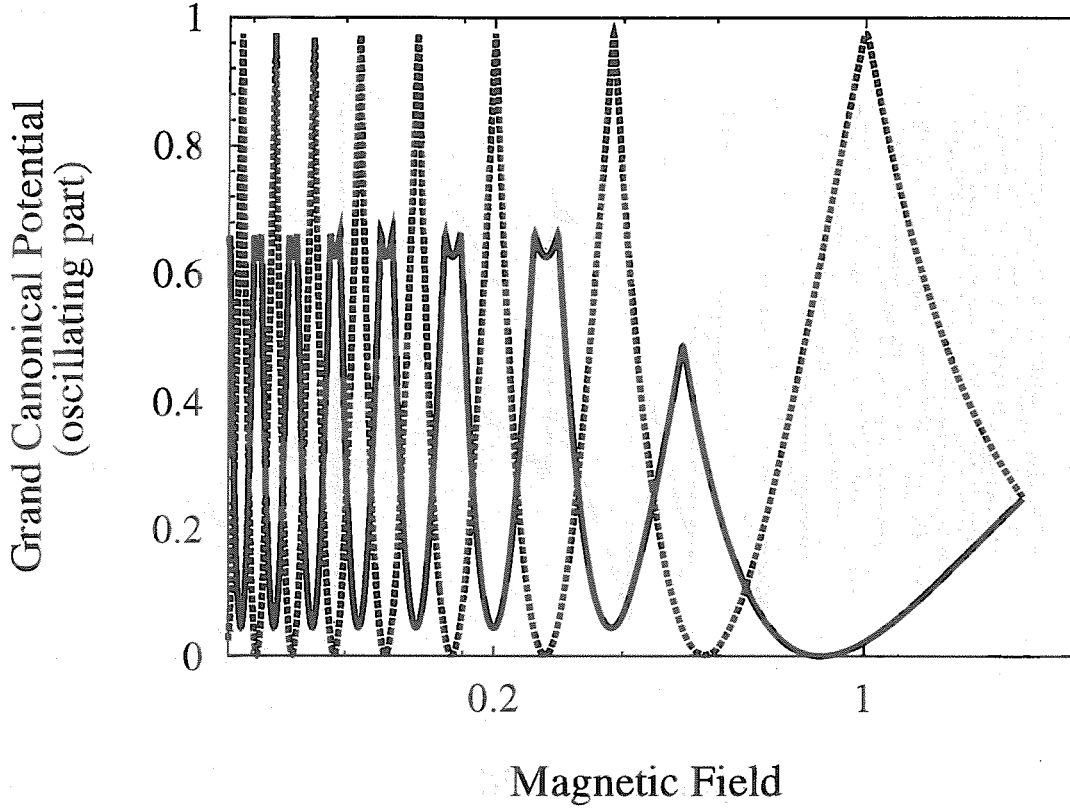
Fig. 8.— The oscillating component of proton grand canonical potential in units of $(2F_H r_p/a)$, see Eq. (53) and discussion therein, of a slab versus magnetic field in units of (λ_p/μ_N).

to the electron bulk system the protons show positive paramagnetic response in magnetic fields, when proton spins are preferably directed along the field vector. The positively defined proton gyromagnetic ratio (see Eq. (8)) favors the preferential occupation of lower laying spin-up proton energy levels as compared to spin-down levels. Such an excess of the number of spin-up protons originates from the relative shift of minority- and majority-spin levels in the presence of a field. This shift leads to a change in the grand canonical potential which can be expressed as

$$\delta\Omega_p = \delta\Omega_{p\uparrow} + \delta\Omega_{p\downarrow} \approx [\delta\Omega_p^o(\lambda_p - \Delta_p) + \delta\Omega_p^o(\lambda_p + \Delta_p)]/2 , \qquad (57)$$

where the index "o" denotes the orbital magnetism and implies that $\delta\Omega_p^o$ yields the discussed in the previous section (sect. 4.1.1) oscillating part of proton GCP corresponding to the case, when the proton orbital magnetism associated with the second term in the rhs of Eq. (8) (see also Eq. (9)) is accounted for, while the first term in the rhs of Eq. (8) is excluded.

In the case of grand canonical ensemble the first term of rhs of Eq. (57) vanishes when the minority-spin energy levels are shifted above the Fermi energy, i.e. $\lambda_p < \Delta_p$. The magnetic response is given by diamagnetism of majority spin protons. At such fields the system shows a single discontinuity anomaly.
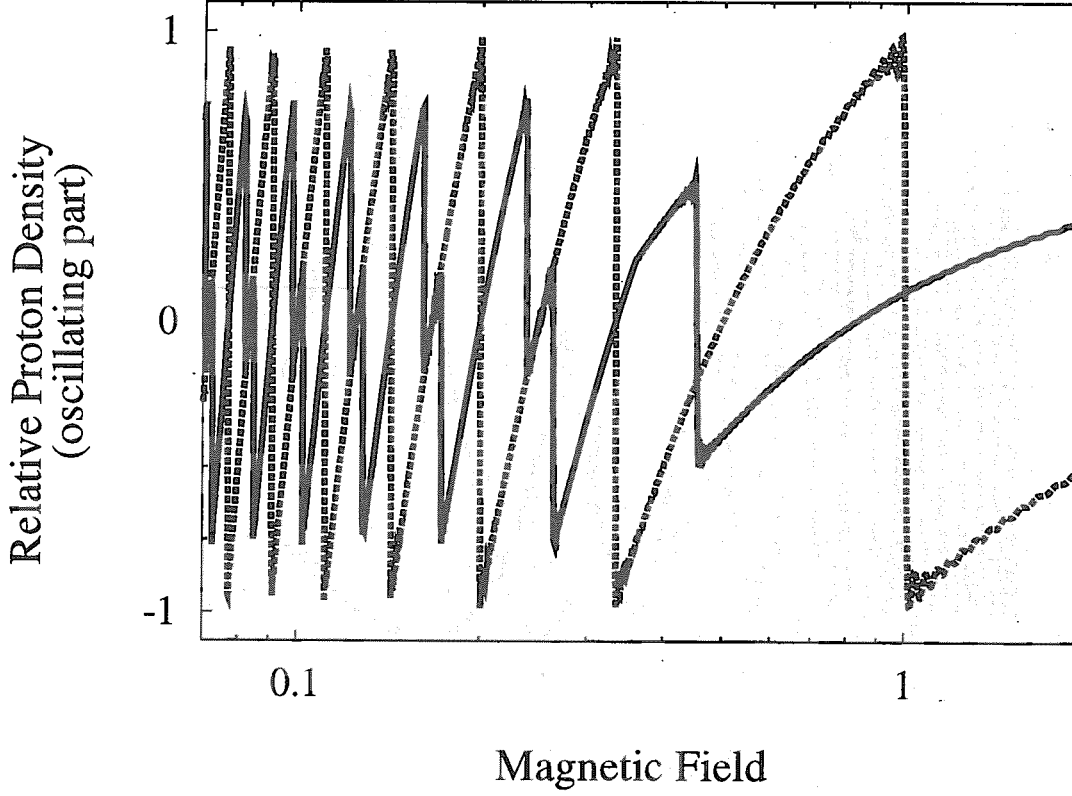
Fig. 9.— The oscillating part of the slab proton density measured in the units $eH/4\pi\hbar c a$ versus magnetic field presented in $(\lambda_{\mathrm{p}}/\mu_{\mathrm{N}})$.

When the condition $\lambda_{\mathrm{p}} > \Delta_{\mathrm{p}}$ is satisfied the superposition of first and second terms of Eq. (57) gives rise to an interference effect in the quantum oscillations. Accounting for a shift $\sigma_i \Delta_{\mathrm{p}}$ (see Eqs. (56) and (57)) we write the oscillating part of GCP as

$$\delta\Omega_{\mathrm{p}}(\lambda_{\mathrm{p}}) = \frac{m_{\mathrm{p}} S}{\pi\hbar^2} \sum_{k=1}^{\infty} (-1)^k \left(\frac{\omega_{\mathrm{L}}}{\pi k}\right)^2$$

$$\cos\left(\pi k \lambda_{\mathrm{p}}/\omega_{\mathrm{L}}\right) \cos\left(\pi k g_{\mathrm{p}}/2\right) R(kT/\omega_{\mathrm{L}}). \tag{58}$$

We see that presence of Pauli magnetic reactivity gives rise to a constant shift of the phase in GCP oscillation components. As seen in fig. 8 such a phase shift between two oscillating contributions yields in addition some beats in the total oscillating GCP resulting in a slight suppression. Such beats can be seen as well in the dependence of the proton density on the ratio of Fermi energy to the magnetic field displayed on fig. 9.

Accounting for both spin- and orbital-magnetism at $\lambda_{\mathrm{p}} > \Delta_{\mathrm{p}}$ the grand canonical potential is written as

$$\frac{\Omega_{\mathrm{p}}}{\Omega_{\mathrm{o}}^0} = 1 - \frac{1}{3}\left(\frac{\omega_{\mathrm{L}}}{\lambda_{\mathrm{p}}}\right)^2 \left(1 - 3g_{\mathrm{p}}^2 \cdot\right.$$

$$+ \frac{12}{\pi^2} \sum_{k=1}^{\infty} (-1)^k k^{-2} \cos\left(\pi k \lambda_{\mathrm{p}}/\omega_{\mathrm{L}}\right) \cos\left(\pi k g_{\mathrm{p}}/2\right) R(kT/\omega_{\mathrm{L}}) \right). \tag{59}$$
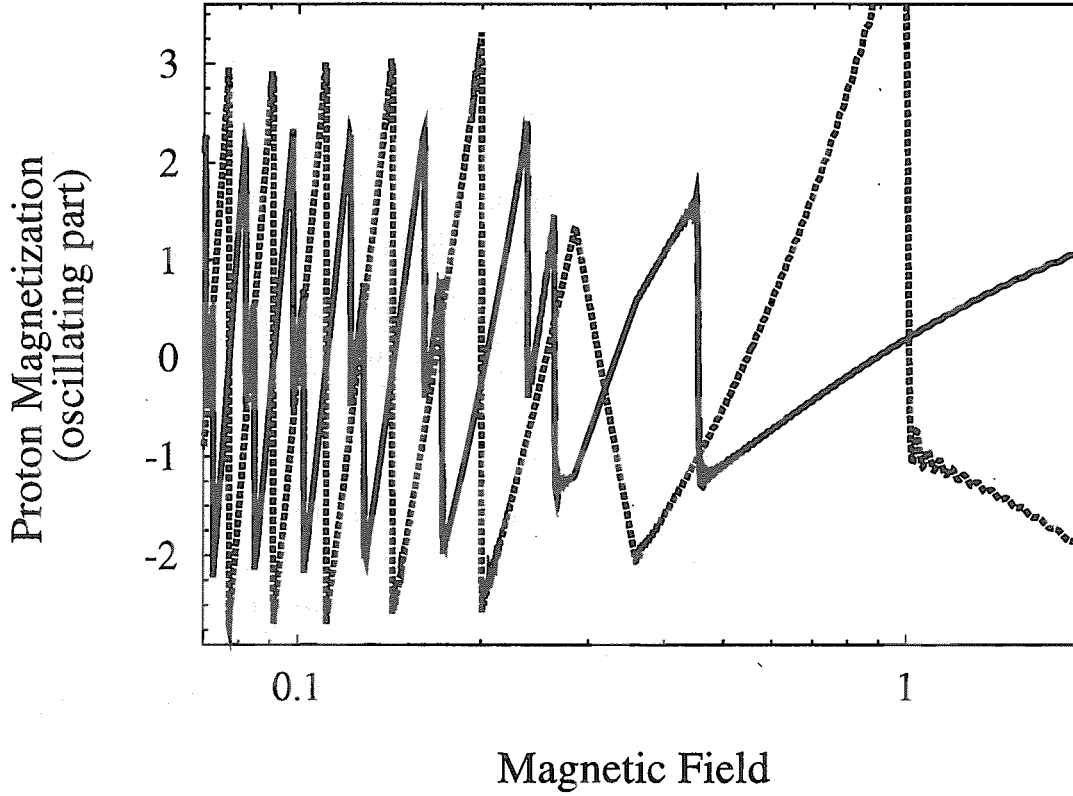
Fig. 10.— The quantum fluctuations of the slab proton orbital magnetization measured in $\mathcal{P}_o^0$, see Eq. (54), versus magnetic field given in the units (λ_p/μ_N).

Using Eqs. (2) and (59) the orbital magnetization of a slab is given by

$$\frac{\mathcal{P}_p}{\mathcal{P}_p^0} = \left(\frac{\omega_L}{\lambda_p}\right)(1 - 3g_p^2) + \frac{6}{\pi}\sum_{k=1}^{\infty}(-1)^k k^{-1}\left(\sin\left(\pi k\lambda_p/\omega_L\right)\right.$$

$$+ \left.\frac{2\omega_L}{\pi k\lambda_p}\cos\left(\pi k\lambda_p/\omega_L\right)\right)\cos\left(\pi k g_p/2\right)R(kT/\omega_L). \tag{60}$$

As seen in fig. 10 the relative shift of spin-up and spin-down levels gives rise to more frequent jumps of magnetization with slightly reduced amplitude.

Finally, collecting the contributions of smooth, Eqs. (48) and (50), and oscillating, cf. Eq. (55), components we obtain the proton magnetic susceptibility to be

$$\frac{\chi_{pt}}{|\chi_L|} = 3g_p^2 - 1 \tag{61}$$

$$- 6\left(\frac{\lambda_p}{\omega_L}\right)^2\sum_{k=1}^{\infty}(-1)^k\cos\left(\pi k\lambda_p/\omega_L\right)\cos\left(\pi k g_p/2\right)R(kT/\omega_L).$$

4.2. Magnetic Response of Outer Crust Nuclides

As we have seen in the previous section (sect. 4.1) the quantization of proton spatial motion (i.e. the Landau levels in magnetic fields) gives rise to some magnetic response anomalies associated with the de Haas-van Alphen oscillations. Such anomalies become

noticeable at relatively large fields and result in a step-like change of proton magnetization at conditions corresponding to the closure of the Landau level. As demonstrated in proceeding section the step-like magnetization jumps are particularly pronounced for the case of finite nuclei. Such a feature is due to the discrete (i.e. shell) level structure of the confined (i.e. dot-like) system (see Kondratyev, Maruyama & Chiba 1999, 2000, 2000a, 2001, 2001a, Kondratyev 2001a). The level crossing in a varying magnetic field leads to a jump of the nuclear magnetic moment.

4.2.1. Structure of Spherical Nuclei: The Nilsson Model

Great success in the understanding of many properties of stable nuclei is associated with the Nilsson model (NM) (cf. e.g. Ring & Schuck 1980, Nilsson & Ragnarsson 1990) which is based on the HO confining potential approximation for the nuclear mean-field. Due to the simplicity of the Hamiltonian this model provides rather clear and realistic picture of the nuclear structure.

For nuclei with $N, Z < 40$ one can assume the form of Eq. (6) for the sp Hamiltonian with spherical HO

$$V_N(r) \approx \frac{m_N}{2}\omega_0^2 r^2 , \quad \omega_0 \approx 41/A^{1/3} \text{ MeV}, \tag{62}$$

and spin-orbit interaction, cf. Eq. (7),

$$V_{ls} \approx -2\eta_{so}\,\omega_0 \cdot (\hat{\mathbf{l}} \cdot \hat{\mathbf{s}}) , \tag{63}$$

where $\hat{\mathbf{l}}$ represents the orbital angular momentum operator, the components of the spin operator $\hat{\mathbf{s}}$ are given by the Pauli matrices, and the parameter η_{so} depends on the principal quantum number. Alternatively, the value of the parameter η_{so} can be assumed to be A-dependent (cf. e.g. Möller et al. 1995). In our experience we find that the choice of η_{so} parametrization affects only slightly qualitative results for the magnetic field effect on the structure of nuclei in the iron region. As discussed by Kondratyev, Maruyama & Chiba (1999) qualitative magnetic effects remain also for deformed shapes of nearly stable nuclei.

The oscillating part of GCP for a case of the unperturbed arbitrary HO (i.e. without the spin-orbit coupling term) is discussed by Kondratyev, Maruyama & Chiba (1999, 2001) and briefly outlined in Appendix A. Since the condition $\eta_{so} \ll 1$ is sutisfied we include the effect of the spin-orbit coupling term, Eq. (63), perturbatively. Using the cylindrical coordinate representation and the first order of perturbation theory the sp energy spectrum is written as

$$\epsilon_{n_\perp l_3 n_3 i} \approx \epsilon_{n_\perp l_3 n_3} - 2\eta_{so}\omega_0 l_3 \sigma_i , \tag{64}$$

where $\sigma_{i=\uparrow} = 1/2$ for the spin-up nucleons (i.e. with the spin directed along the quantization axis, $i = \uparrow$) and $\sigma_{i=\downarrow} = -1/2$ for the spin-down nucleons (i.e. with the spin directed opposite to the axis direction, $i = \downarrow$). The sp energy levels of spherical HO are given by

$$\epsilon_{n_\perp l_3 n_3} = \omega_0(2n_\perp + |l_3| + n_3 + 3/2), \qquad (65)$$

where $n_\perp = 0,1,2,...$ indicates the radial quantum number for the motion perpendicular to the quantization axis, $l_3 = 0, \pm 1, \pm 2, \pm 3, ...$ denotes the quantum number of the projection of the orbital angular momentum to the axis, and n_3 is the quantum number associated with the motion along the axis.

The represented by Eqs. (64) and (65) spectrum is identical (Fock 1928) to that of a triaxial HO with frequencies

$$\omega_1 = \omega_0(1 + \eta_{so}), \quad \omega_2 = \omega_0(1 - \eta_{so}), \quad \text{and} \quad \omega_3 = \omega_0. \qquad (66)$$

Therefore, the equations derived in Appendix can be used for an analysis of the shell-correction GCP when accounting for the spin-orbit coupling as well. Using Eqs. (62), (63), and (66) we write the kth component of GCP as

$$\Omega_k^0 = \frac{\omega_0(-1)^k}{4\pi^2 k^2} \left(\frac{\cos(kX)}{\sin(k\pi(1 + \eta_{so})) \sin(k\pi(1 - \eta_{so}))} R(k\tau) \right.$$
$$+ \frac{(1 - \eta_{so})\cos(kX/(1 - \eta_{so}))}{\sin(k\pi/(1 - \eta_{so})) \sin(k\pi(1 + \eta_{so})/(1 - \eta_{so}))} R(k\tau/(1 - \eta_{so}))$$
$$+ \left. \frac{(1 + \eta_{so})\cos(kX/(1 + \eta_{so}))}{\sin(k\pi/(1 + \eta_{so})) \sin(k\pi(1 - \eta_{so})/(1 + \eta_{so}))} R(k\tau/(1 + \eta_{so})) \right), \qquad (67)$$

where the superscript "0" indicates zero magnetic field, $X = 2\pi\lambda/\omega_0 \approx 2\pi(3N)^{1/3}$ counts the number of filled shells, $\tau = 2\pi^2 T/\omega_0$ gives the suppression factor of the shell-oscillation amplitude due to the temperature. In applications below we focus on very low temperature limit (i.e. $\tau \ll 1$, $R \approx 1$) and refer for the oscillating part of the grand potential, Eq. (67), simply as the shell-correction energy.

In fig. 11 the total shell-correction energy is plotted versus the number of neutrons for symmetric nuclei ($N = Z$). We see that neglecting the spin-orbit interaction gives the magic numbers, $N = 8, 20, 40, ...$, corresponding to closed shells with principal quantum numbers $n = 1, 2, 3...$ The shell-correction energy displays pronounced minima at these numbers. We note that values of the shell-correction energy are large when the spin-orbit interaction is omitted. This is a consequence of the high degeneracy of the sp energy levels (see above).

Making use of the condition $\eta_{so} \ll 1$ Eq. (67) can be further simplified (cf. e.g. Kondratyev & Lutz 1998)

$$\Omega_k^0 \approx -\frac{\omega_0(-1)^k}{8\pi^4 k^2} X(X + 1)\cos(kX) j_0(\eta_{so} kX) R(k\tau), \qquad (68)$$
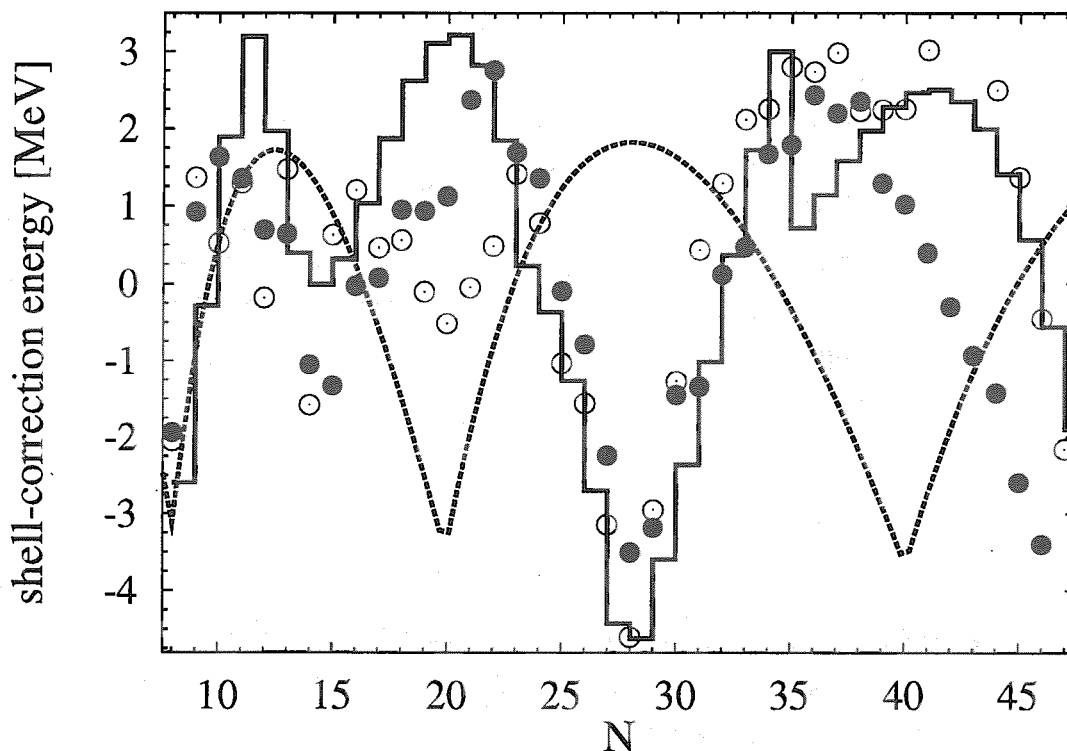
Fig. 11.— The shell-correction energy as a function of the number of neutrons for symmetric nuclei with the spherical HO potential. The solid line denotes the results of calculations for δF^1 with the spin-orbit coupling included perturbatively at the values of parameter $\eta_{so} = 0.16$ for $n = 1$, 0.14 for $n = 2$, and 0.2 for $n = 3$. The dashed line corresponds to zero spin-orbit coupling constant and gives the energy in the units $0.5\ A^{1/3}$ MeV. The full dots represent the deviation of the experimental masses Audi & Wapstra 1995 from the liquid drop model (cf. Ring & Schuck 1980) prediction, the open circles show the results of ref. Möller et al. 1995.

where $j_0(x)$ denotes the spherical Bessel function of zero-th order. We note that in Eq. (68) zero point motion is accounted for as compared to previous results by Kondratyev, Maruyama & Chiba (2000, 2001). A-dependence of the amplitude of shell-oscillations Eq. (68), $\delta E \sim A^{1/3}$, is determined by A-dependence of the HO level spacing ω_0, Eq. (62), and the degeneracy of the Fermi energy level $\sim A^{2/3}$. The spin-orbit coupling removes such a degeneracy resulting in weaker shell effect as well as slower increase of an amplitude of shell-oscillations with the mass number as suggested by Eq. (68).

Including the spin-orbit term Eq. (63) allows to reproduce properly experimentally observed nuclear magic numbers of light and medium mass nuclei (see fig. 11 and Ring & Schuck 1980). Accounting for zero point motion improves the agreement with experimental data for the mass numbers in the oxygen region. In particular, we note that an excess of the binding energy associated with the spherical shell closure at $N = Z = 28$ is stronger than at $N = Z = 20$. This property is corroborated with the experimental findings. From fig. 11 we see that the closed neutron and proton shells for 20 nucleons hardly show up at all as an extra experimental binding for ^{40}Ca whereas both the nuclei ^{32}S and
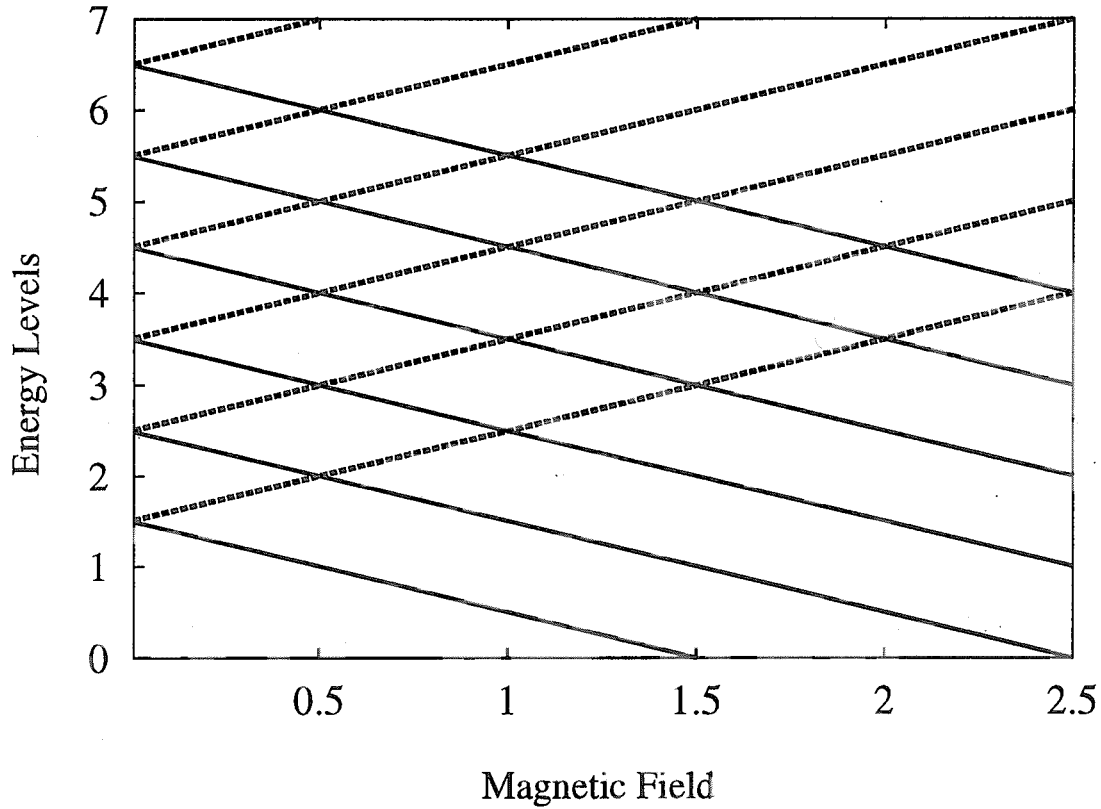
Fig. 12.— Magnetic field dependence of the spherical HO sp energy levels. The solid and dashed lines indicate the majority- and minority-spin levels, respectively. The energy is measured in the units of level spacing ω_0, while the field is given in ω_0/μ_N.

^{36}Ar appear to be "stronger bound" than ^{40}Ca. The comparison to predictions obtained within a more involved treatment (Möller et al. 1995) suggests that the present model yields similar accuracy in the description of the experimentally observed shell-oscillations in binding energies of light nuclei up to the iron region.

Thus accounting for the splitting of nucleon energy levels due to the spin-orbit coupling is crucial for an understanding of nuclear magic numbers observed in the laboratory. We remark, however, that the neutron rich crust nuclides correspond to the confining potential with smaller stiffness (cf. Haensel, Zdunik & Dobaczewski 1989, Oyamatsu & Yamada 1994), i.e. smaller value of the spacing between the major shells ω_0. This gives rise to a suppression of spin-orbit splitting, cf. Eq. (7). Therefore, in present work we extensively analyze also the case of zero spin-orbit term which gives rather transparent picture of the field effect and can be directly applied to analyze the shell structure of e.g. atomic clusters in magnetic fields.

4.2.2. Neutron Spin-Magnetization in Nuclei: Pauli-Paramagnetic Response

In this section we argue that the shell effect of nuclei leads to the jump anomalies of neutron magnetization as well. The magnetic field $\mathbf{B}$ effect for neutrons is represented by
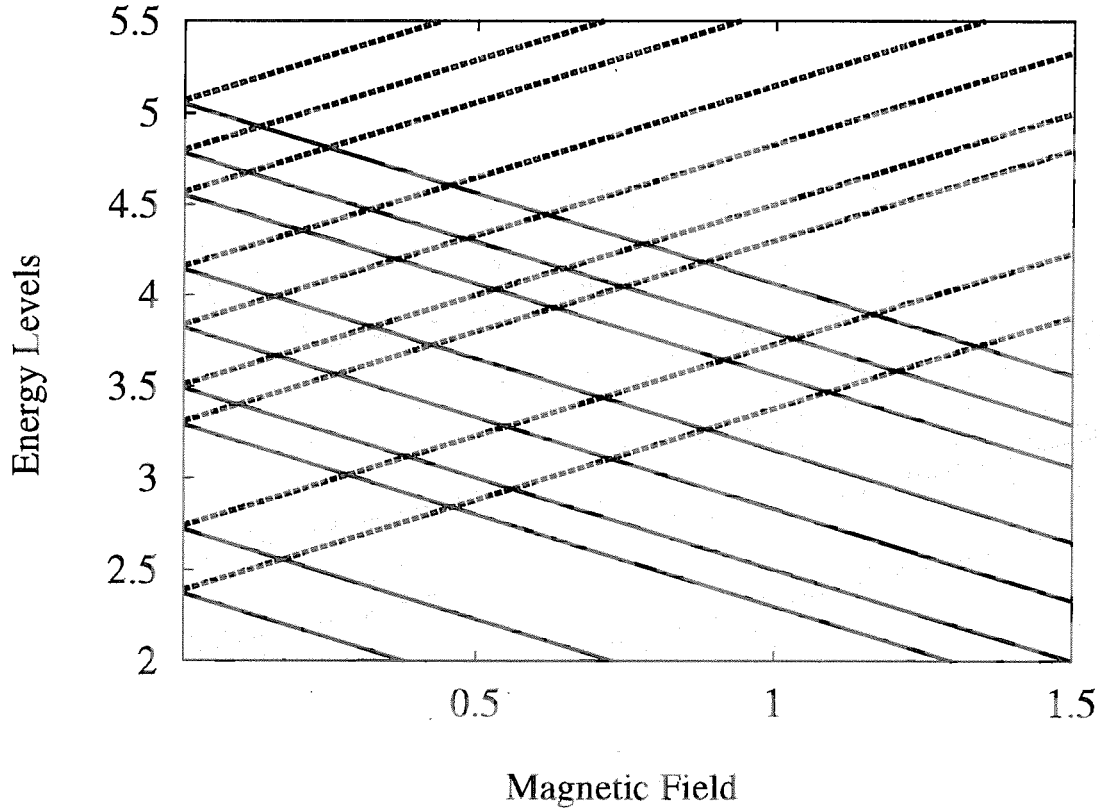
Fig. 13.— Magnetic field dependence of the sp energy levels for NM with spherical HO confining potential. The units are the same as in fig. 12.

the first term in rhs of Eq. (8) arising due to an interaction of the field with the neutron dipole magnetic moment $\hat{\mathcal{M}}_n = g_n \mu_N \hat{s}$. The orbital motion is not affected by the magnetic field at small s-o coupling since neutrons are neutral particles and, therefore, exhibit only the Pauli-type of the magnetization associated with rhs of Hamiltonian Eq. (8). The field dependence of the neutron contribution to GCP as well as magnetization are determined then by Eqs. (34) and (35), respectively. Similarly to the uniform neutron liquid (sect. 3) such Pauli type magnetization originates from the relative shift Eq. (33) of minority- and majority-spin neutron energy levels.

The shift Eq. (33) modifies the level structure of nuclides and defines paramagnetic response properties. Figures 12 and 13 display the field dependence of the neutron single particle levels for spherical HO and NM, respectively. As seen for the case of spherical HO Hamiltonian the levels show regular crossing at the same values of the field strength. Such a behavior is due to highly degenerate equidistant sp energy spectrum of HO potential. Including the s-o coupling removes the spherical HO degeneracy leading to a non-equidistant spectra. Consequently, the level crossings are met more frequently with changing magnetic field.

These properties of sp levels are reflected in the magnetic field dependence of the shell-correction energy. As demonstrated in fig. 14 the regular level structure of spherical HO
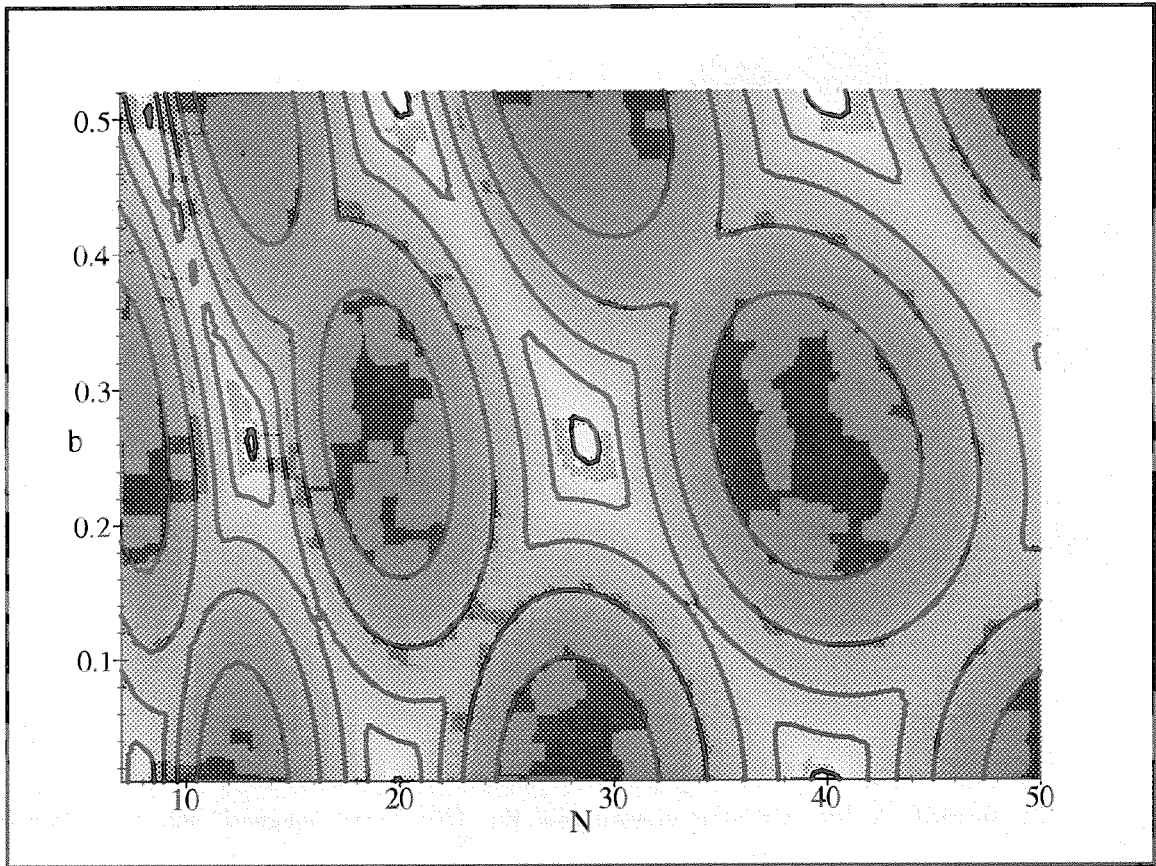
Fig. 14.— The spherical HO model prediction of the neutron semiclassical shell-correction energy versus the neutron number and magnetic field. The smaller energies are indicated by white regions, while the dark regions denote the larger energies. The contours are plotted with the step 1 starting from -3 in the units $A^{1/3}$ MeV.

gives rise to periodic behavior of the neutron shell-correction energy as a function of the magnetic field. The NM displays similar qualitative features as have been extensively discussed by Kondratyev, Maruyama, & Chiba (1999, 2000, 2000a, 2001). Therefore, to illustrate in the simplest way the qualitative picture of the considered effect we present the results for magnetic reactivity of nuclei on an example of spherical HO.

Figure 15 represents the magnetic field dependence of the difference $\mathcal{N}$ between the majority- and minority-spin neutron numbers at various values of the total neutron number. As seen this dependence exhibits a step-like behavior at field strengths corresponding the majority- and minority-spin level crossing. Such a behavior resembles properties of a magnetic phase transition.

The physical origin of such a jump of nuclear magnetic moment can be rather clearly understood within the following qualitative picture applied for the spherical HO potential. Let us consider a magic nucleus with a filled neutron shell (i.e. the number of neutrons
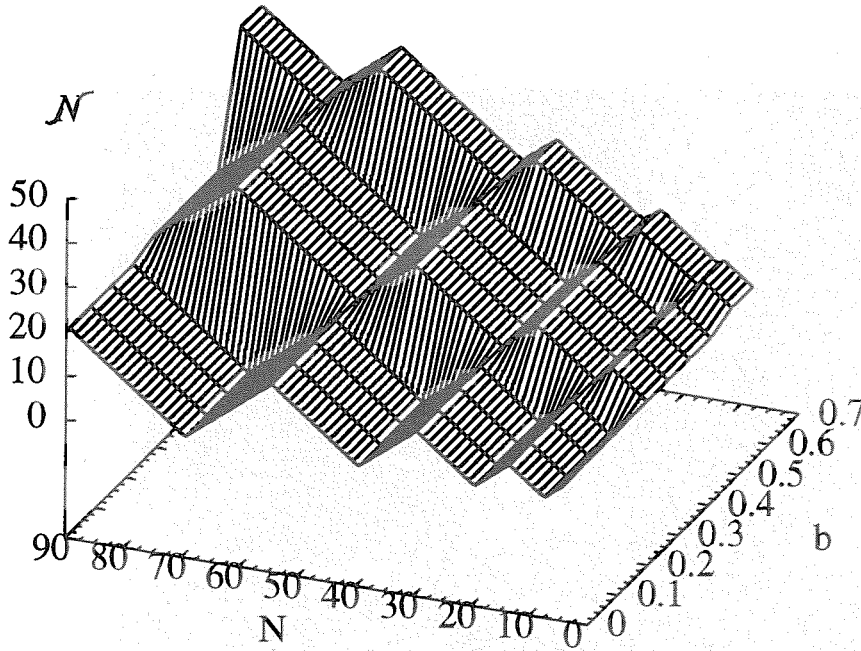
Fig. 15.— The quantity $\mathcal{N}$ (i.e. magnetic moment, see Eq. (35)) versus magnetic field b and neutron number N.

on the highest occupied shell corresponds to the degeneracy number). For a case of zero spin-orbit coupling such a nucleus could have e.g. 40 neutrons ($N = 40$) when the shell with the principal quantum number $n = 3$ is just filled. At zero magnetic field such a magic nucleus has zero magnetic moment and corresponds to a negative minimum of the shell-correction energy (see fig. 14). The magnetic field shifts majority- and minority-spin neutron levels down and up, respectively (see fig. 12). At the field strength corresponding to the energy shift on a half of HO frequency (i.e. $b = |0.5/g_n|$) the majority- and minority-spin energy levels cross. Therefore, 20 spin-up neutrons of n=3 shell (at $b < |0.5/g_n|$) are rearranged to occupy the spin-down n=4 shell. Consequently, the magnetic moment of such a nucleus is changed step-wise at the level crossing.

We recall here that the neutron magnetization corresponds to the spin alignment reversed to the magnetic field vector due to the negatively defined neutron gyromagnetic ratio. Therefore, in the magnetic field the relative number of spin-down neutrons ($N_\downarrow$) exceeds the number of spin-up neutrons ($N_\uparrow$). However, the actual balance between the minority- and majority-spin neutrons is rather sensitive to the shell structure.
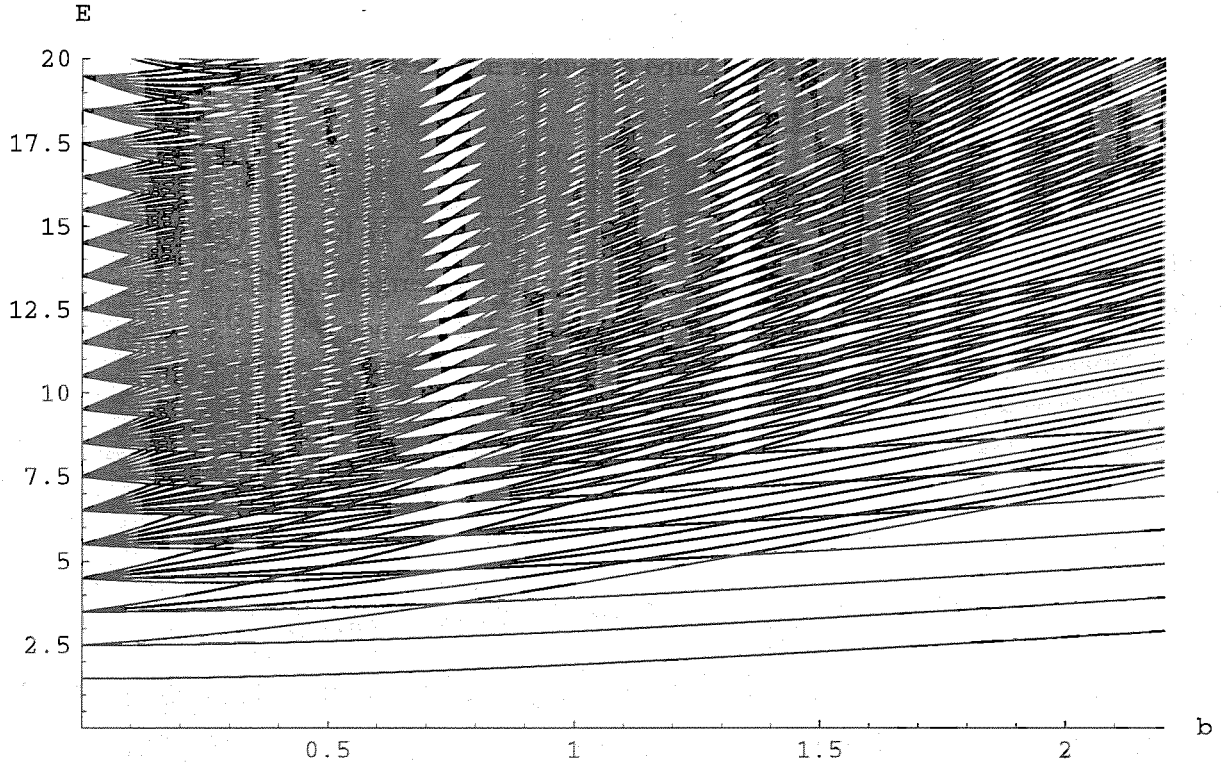
E

Fig. 16.— Magnetic field dependence of the sp energy levels of spinless protons for spherical HO confining potential. The units are the same as in fig. 12.

4.2.3. Orbital Magnetism of Protons in Nuclei

As discussed in sect. 4 the proton magnetic response is given by a superposition of orbital and spin magnetism. In this section we briefly consider some properties regarding the orbital magnetic reactivity of protons with confined spatial motion.

The Landau-type proton orbital response in the magnetic field arises due to an interaction of the field with the charge moving on an orbit. As a consequence, the proton shell-correction GCP exhibits an additional field dependent modification as compared to the neutron GCP as extensively studied by Kondratyev, Maruyama, & Chiba (1999, 2000, 2000a, 2001). The sp energy level spectrum of spherical HO including the Hamiltonian Eq. (9) can be written as (Fock 1928) (cf. Eq. (65) of sect. 4.2.2)

$$\epsilon_{n_\perp l_3 n_3} = \omega_0 [\sqrt{1 + b^2}(2n_\perp + |l_3| + 1) - bl_3 + n_3 + 1/2], \tag{69}$$

where the notations are identical to those of Eq. (65) with a quantization axis directed along the magnetic field.

As seen in fig. 16 the degree of the degeneracy for the proton energy levels is reduced dramatically because of an interaction of the orbital magnetic moment with a field. The proton shell structure is almost washed out as compared to the case of neutrons (cf. figs.

12 and 13 and discussions therein). As evident from fig. 16 the degeneracy is restored, however, at certain relatively large fields. Such bifurcation points of a system appear similarly to cases of large deformations (cf. (Kondratyev, Maruyama & Chiba 1999) and refs. therein).

One can easily see that the spectrum given by Eq. (69) is equivalent (Fock 1928) to that of a triaxial HO with the frequencies

$$\omega_1 = \omega_0 \nu_+, \quad \omega_2 = \omega_0 \nu_-, \quad \text{and} \quad \omega_3 = \omega_0, \tag{70}$$

where $\nu_\pm = \sqrt{1 + b^2} \pm b$. This allows to utilize the results for GCP of HO for the nuclei in magnetic fields (Kondratyev, Maruyama & Chiba 2000, 2001). Applying the condition $b \ll 1$ we obtain (cf. e.g. Kondratyev & Lutz 1998) the k-th component of the proton GCP in the form

$$\Omega_k^o \approx -\frac{\omega_0(-1)^k}{4\pi^4 k^2} X(X+1)\cos(kX) j_0(bkX) R(k\tau) \tag{71}$$

which represents the k-th component for the nonperturbed HO modulated by the spherical Bessel function of zero order with the field dependent argument. Similarly to Eq. (68) in Eq. (71) it is accounted for zero point motion as compared to previous results by Kondratyev, Maruyama & Chiba (2000, 2001).

The relation Eq. (71) properly describes some slight re-increase of shell oscillation amplitude at small values b. However, rather pronounced re-enhancement of the level degeneracy at, e.g., the field strength $b \approx 0.75$ (see fig. 16) is not reproduced within such a perturbative treatment.

4.2.4. Paramagnetism versus Orbital Magnetism in Nuclei

Switching on the spin-magnetism leads to further reduction of the energy level degeneracy. From the comparison of figs. 16 and 17 we see that the spin magnetic moment gives rise to more frequent level crossings with changing magnetic field. The re-enhancement of the degeneracy remains, however, almost at the same field strengths. The levels cross at fields corresponding to the relative shift of proton majority- and minority-spin energy levels Δ_p comparable to the energy difference between major shells given by the HO level spacing ω_0. The energy of the first Landau level is by the factor $2 - 3$ smaller than the energy difference between major shells, while the radius of the proton cyclotron orbit is larger than radii of nuclei on approximately the same factor. Consequently, Landau levels give practically no contribution to the outer crust magnetism at such a field strength. The proton Landau diamagnetism is expected to dominate at the condition $b \gg 1$ i.e. at a field strength exceeding $B \sim 10^{19.5}$ G.

The proton contribution to the magnetic moment of a nucleus is given as a combination
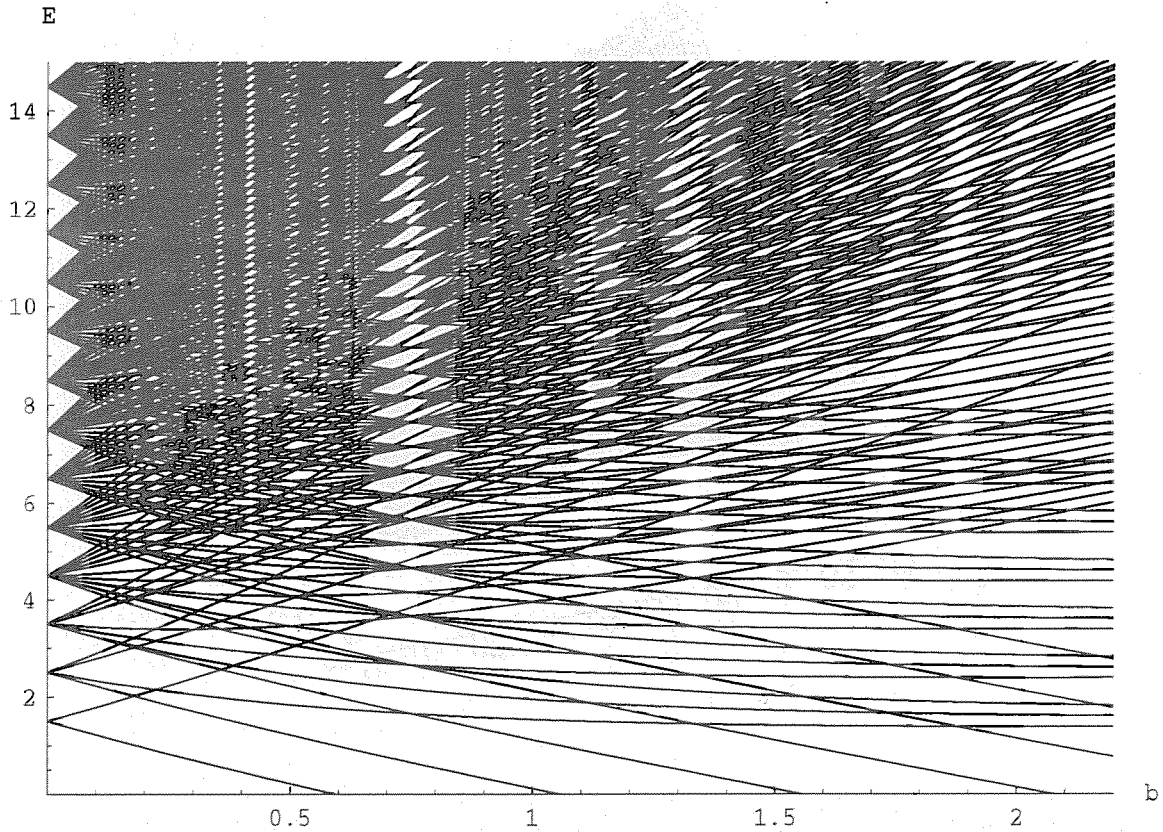
Fig. 17.— Magnetic field dependence of the proton sp energy levels for spherical HO confining potential. The units are the same as in fig. 12.

of the spin and orbital magnetic components

$$M_{\rm p} = [g_{\rm p}\mathcal{Z} + \sum_i l_3^i]\mu_{\rm N} \approx gI_{\rm b}\ \mu_{\rm N}, \tag{72}$$

where $\mathcal{Z} = (Z^\uparrow - Z^\downarrow)/2$ measures the difference between majority-spin $(Z^\uparrow)$ and minority-spin $(Z^\downarrow)$ proton numbers, l_3^i denotes the projection of angular momentum on the field axis.

Figure 18 shows the quantity $gI_{\rm b}$ as a function of the magnetic field at different values of the proton number. The step-like behavior of nuclear magnetization is displayed for protons as well. The associated field change between jumps is significantly smaller as compared to the neutron magnetic response as seen in more details on fig. 19.

It should be noticed an important difference between the proton orbital magnetism considered here and the Landau diamagnetism of a homogeneous liquid or slab-like structures considered in sect. 4.1. The latter is originating from the quantization of Landau levels. Since at relatively small field strengths (i.e. $b < 1$, which are considered below) the radii of Landau levels are much larger than nuclear radii they give practically no contribution to the magnetic response. The orbital magnetism in such a case is mainly caused by an interaction of magnetic field with magnetic dipole arising from the quantum orbital mo-
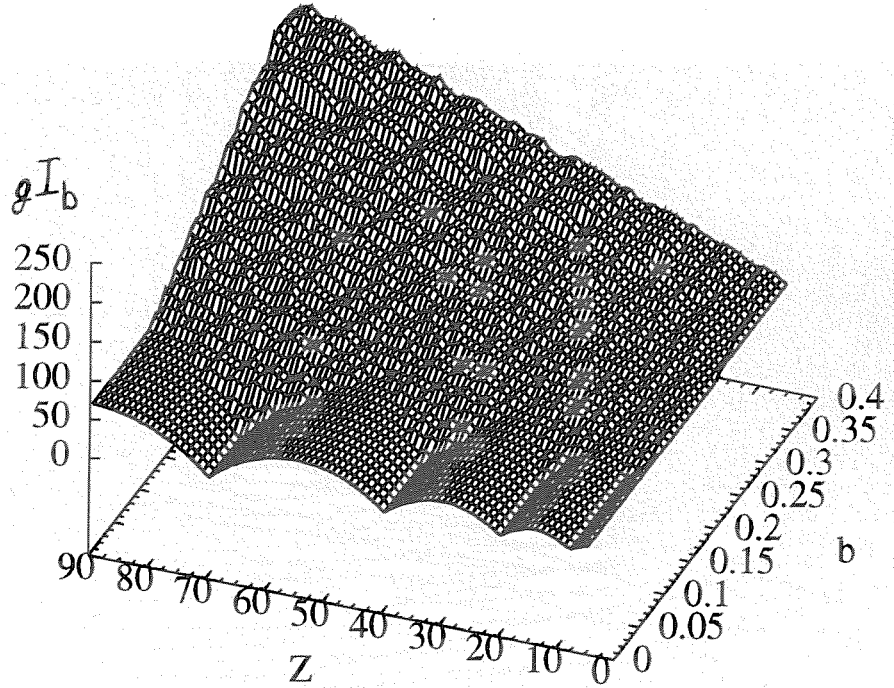
Fig. 18.— Proton magnetization (gI_b) versus magnetic field b and proton number Z.

tion of protons inside the nucleus. The orbital magnetic response of such inhomogeneous systems is considerably amplified as compared to the case of a homogeneous liquid.

We stress here that in contrast to the homogeneous liquid the neutron star crust may display positive as well as negative proton linear magnetic response of Pauli-type due to inhomogeneous structure. The nuclear shell effect influences the relationship in the occupation of minority- and majority-spin proton energy levels and modifies properties of the magnetization.

5. Modeling the Magnetodynamics of Crusty Nuclear Matter

As shown in sect. 4 the quantization of spatial nucleon motion gives rise to the step-like jumps of the magnetic response in varying magnetic fields. In particular outer crust nuclides display such an anomaly at the crossing of nuclear levels. In this section we demonstrate that these properties result in the noise during the crust demagnetization. As a consequence, the time evolution of magnetic fields experiences erratic jumps leading to a sharp energy release to the magnetosphere of the magnetic energy stored in, e.g., the nuclear degrees of freedom of neutron star crusts. Therefore, within present picture the mechanism of SGR burst emission by a magnetar is similar to the generation of a noise in the loudspeaker by the coil of a wire surrounding a ferromagnet and being put under the
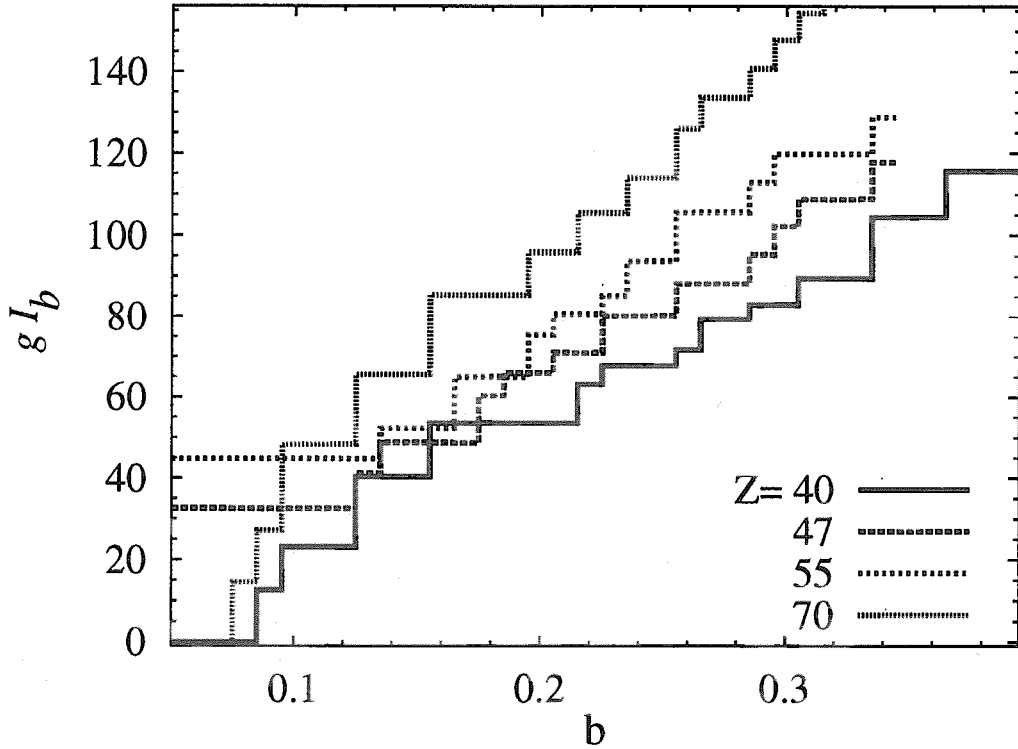
Fig. 19.— Proton magnetization (gI_b) versus magnetic field b at proton number $Z = 40$ (solid line), 47 (dashed line), 55 (dotted line) and 70 (frequent dots).

conditions of magnetization reversal by external varying magnetic field, i.e. the magnetic Barkhausen emission (see, e.g., Feynman 1965). Because of the domain structure the dynamics of magnetic field exhibits some sharp changes with time. Such a jump induces a current in a wire. The energy released to the coil-wire is determined by the applied field H_{ext}, magnetization of a ferromagnet $\mathcal{P}_F$ as well as respective volume V_{magn} and estimated to be

$$E_{Bark} \approx H_{ext}\mathcal{P}_F V_{magn} . \qquad (73)$$

The analogy can be seen between the crust and ferromagnet as well as between the magnetosphere and the coil-wire. We note that 'magnetar' related processes considered here correspond to ultramagnetized media and energy scale larger by about 30 orders of magnitude. Furthermore, the sharp change of crust magnetization originates from step-wise behavior of the nuclide magnetic moments rather then from magnetization reversal.

5.1. Magnetic Coupling, Disorder and Fluctuations in Outer Crusts

In this section we quantify some observables related to crust magnetodynamics on the basis of theoretical analysis.

The induced magnetic moment of nuclides contributes to the magnetization of neutron

star crusts on the basis of theoretical analysis. For aligned moments the magnetization component is given by

$$\mathcal{P}_N = \frac{M_N}{V_{WS}} \approx \frac{M_N}{A\mu_N} \frac{\mathcal{D}_{Nb}}{\mathcal{D}_s} 10^{15} \text{ Oe} , \tag{74}$$

where the nuclear magnetic moment $M_N = M_n + M_p$ is represented as a sum of neutron M_n and proton M_p contributions, see Eqs. (35) and (72), respectively, while an average density of bound nucleons $\mathcal{D}_{Nb} = A/V_{WS}$ is related to the Wigner-Seitz volume V_{WS} and evaluated as several tenths of normal nuclear density $\mathcal{D}_s$.

We consider the outer crusts as a polycrystalline structure with nuclei arranged in a closed packed (plausibly bcc) lattice and assume the dipolar interaction between magnetic moments $\mathbf{M}_i$ and $\mathbf{M}_j$ of nuclei i and j

$$J_{ij}^d = \frac{(\mathbf{M}_i \mathbf{M}_j) - 3(\mathbf{M}_i \hat{\mathbf{r}}_{ij})(\mathbf{M}_j \hat{\mathbf{r}}_{ij})}{r_{ij}^3} , \tag{75}$$

where $\hat{\mathbf{r}}_{ij}$ denotes the unit vector indicating the direction from i to j, while r_{ij} gives respective distance. Such a system shows the ferromagnetic ordering (see e.g. Luttinger & Tisza 1946, Weis & Levesque 1993, 1994) with the easiest magnetization axis $\{100\}$. The coupling constant J and an anisotropy energy density K can be estimated from the lattice parameters as

$$J_d \approx M_i M_j / a^3 \sim 0.01 \text{ MeV} , \tag{76}$$

$$K_d \approx 0.1 J_d / V \sim 10^{26} \text{ ergs/cm}^3 , \tag{77}$$

where $a \sim 10^{1.5}$ fm stands for the lattice constant as in previous sections. The coupling strength Eq. (76) corresponds to an effective magnetizing field $\mathcal{P} = J_d/M \approx 10^{13}$ Oe, cf. Eq. (74).

In the energetics of magnetized systems a noticeable effect is represented by demagnetization energy, see (Feynman 1965). Such an energy gives rise e.g. to domain structure of ferromagnets. In our studies we account for such a contribution to the total energy in a global form

$$E_d = \eta \mathcal{P}^2 , \tag{78}$$

where the value of coefficient η depends slightly on the geometry of the magnetized sample.

Another essential feature of realistic systems is associated with fluctuations and randomness. Usually the system contains inhomogeneity and disorder in the form of defects, grain boundaries, impurities, leading to random crystalline anisotropies, and varying interaction strengths in the crystalline structure. Apart from such static spatial fluctuations f_i^{st} we bear in mind dynamical components f_i^d due to inexactness of the model description (see sect. 5.2).

Simple way to implement a certain kind of uncorrelated quenched disorder as well as fluctuations is provided by identifying such effects with uncorrelated random fields f_i,

associated with each site of the lattice, and distributed according the gaussian distribution function

$$W(f_i) = \exp\{-f_i^2/2R^2\}/\sqrt{2\pi}R \qquad (79)$$

as one expects from the central limit (or normal convergence) theorem. We refer to the width R as for the disorder parameter, or just disorder. In the order of magnitude this quantity can be evaluated as an effective magnetizing field $R \sim \mathcal{P} \sim 10^{13}$ Oe (cf. Eq. (75)).

It is worthy to notice here that such a value of R is smaller than an expectation for the inter-jump magnetic field spacing β_{jmp}. Average value of the spacing is defined by the field interval between the successive jumps b_n and b_{n-1}, i.e. $\beta_{\text{jmp}} = < B_n - B_{n-1} >_n$, where $< \cdot\cdot >_n$ denotes averaging over n.

To calculate the field spacing we note that two levels with energy difference $\delta\epsilon$ cross in the field interval

$$\delta B = \delta\epsilon \left(\frac{d\delta\epsilon}{dB}\right)^{-1}. \qquad (80)$$

For neutrons the change rate of the energy difference is given by $\left(d\delta\epsilon/dB\right) = g_n \mu_N \approx 10^{-17}$ MeV/G. The inter-jump field spacing can be, therefore, evaluated from the total nuclear level spacing $< \delta\epsilon >$ as

$$\beta_{\text{jmp}} \approx \left(\frac{d\delta\epsilon}{dB}\right)^{-1} < \delta\epsilon > = \left(\frac{d\delta\epsilon}{dB}\right)^{-1}/\mathcal{W}. \qquad (81)$$

In the second equality of Eq. (81) we take into account that the level spacing is given as an inverted total nuclear level density $< \delta\epsilon > = \mathcal{W}^{-1}$ (Ring & Schuck 1980, Nilsson & Ragnarsson 1990). Since the case of shifted energy levels in the magnetic field corresponds to an excited nucleus, the field spacing is estimated, $\beta_{\text{jmp}} \sim 10^{14}$ G, to be an order of magnitude larger as compared to disorder effects.

5.2. The Randomly Jumping Interacting Moments Model as an Extension of the Ising Model

To model the long-range, far from equilibrium, collective behavior mentioned in the beginning of the section (sect. 5), we define the crusts as a collection of Π domains on a hypercubic lattice with magnetic moments per nucleus m_i which changes step-wise as a function of local magnetic fields b

$$m_i = \sum_n \nu_n \, \theta(b - b_n) \qquad (82)$$

with jumps of a height ν_n at field strengths b_n corresponding to level crossings. Here the step-function $\theta(x < 0) = 0$ and $\theta(x \geq 0) = 1$.

According to an analysis of previous sect. 5.1 the coupling between nearest neighbor (nn) domain-moments is ferromagnetic of a strength J_{ij}, and they interact with a uniform

magnetic field H. Then accounting for the demagnetizing energy in a global form, see Eq. (78) and discussion therein, we introduce the total magnetization (below is also referred to as a mean-field)

$$\mathcal{P} = \sum_i m_i \qquad (83)$$

and express the Hamiltonian of the outer crust domains as

$$\mathcal{H} = - \sum_{ij \in \text{nn}} J_{ij} m_i m_j - (H(t) - \eta\mathcal{P}) \sum_i m_i, \qquad (84)$$

where it is understood that the sum runs over nearest neighbor pairs of moments on sites i and j. The parameter η is determined by a strength of the demagnetizing effect. When moments m_i are allowed for two values ± 1 at vanishing η, the Hamiltonian Eq. (84) represents the Ising model which reliably describes the effects of spontaneous magnetization as well as hysteresis and discontinuities in reversing the magnetization (i.e. magnetization curve). As outlined below in this section within the dynamical picture such effects can be interpreted as magnetic avalanches in the system.

As pointed out in sect. 5.1 in order to simulate realistic systems it is required to incorporate in the Hamiltonian Eq. (84) fluctuating fields (see Eq. (79) and discussion therein). Such fluctuations can prevent the spontaneous magnetization of entire system by keeping it on a metastable state. As a consequence, the magnetization curve is modified, i.e. not all the domain-moments jump at the same value of the external magnetic field. Instead, they jump in avalanches of various sizes that can be broken up or stopped by strongly "pinned" magnetic moments or clusters of previously jumped moments. When the disorder in the crust is small, the picture is qualitatively similar to the pure case of the Ising model. One would expect the predominant macroscopic discontinuity at critical field with a few small precursors in the vicinity. Large disorders, as compared to the coupling strength J, can wash out the sharp transition and result in smooth and almost macroscopically continuous magnetization curve.

Applying random fields the Hamiltonian is then given by

$$\mathcal{H} = - \sum_{ij \in \text{nn}} J_{ij} m_i m_j - \sum_i (H - \eta\mathcal{P} + f_i) m_i. \qquad (85)$$

For analytic calculations and simulations we set the interaction between the moments to be independent of the moments and equal to J for nearest neighbors $J_{ij} = J$ and zero otherwise.

The crust magnetodynamics is determined by the magnetic moment m_i jumps which occur when the difference between its local effective field

$$b_i = J \sum_{j \in \text{nn}} m_j + H - \eta\mathcal{P} + f_i \qquad (86)$$

and some of the quantities b_n, i.e. the value $\delta b_n = b_i - b_n$, changes sign. At the condition $b_{n+1} - b_n \gg \delta b_n \gg R$ almost all the moments equal to the value

$$v_n = \sum_{i=1}^{n} \nu_i \tag{87}$$

and point along the field **H** direction (i.e. $m_i = v_n$ for all i). As the field adiabatically decreases the moments progressively jump to v_{n-1}, v_{n-2}, ... Because of the nearest neighbor interaction, the jumped moment can result in the jump of a neighbor which in turn might lead to the reducing moment of another neighbor, and so on, generating thereby an avalanche of moment jumps. The adiabatically changing field $H(t)$ implies that the external field is kept constant during each avalanche, while the magnetization varies according to the definition of the mean-field Eq. (83). At large disorders corresponding to the wide distribution of random fields the magnetic moments tend to jump independently of each other. Small avalanches give rise to the smooth (on a macroscopic scale) magnetization curve. On the other hand, small disorder implies a narrow random field distribution which allows for large avalanches. This leads to noticeable discontinuities in the magnetization curves similarly to what is found for the Ising model at zero temperature. At transitional values of the parameters $R = R_c$ and $H = H_c$ the system shows critical scaling behavior and the widest distribution of the avalanche sizes.

We refer for such a model as randomly jumping interacting moments (RJIM) model.

6. Numerical Simulations for Hysteresis and Avalanches in Outer Crust Magnetodynamics

The simplified description of the neutron star crust magnetodynamics within RJIM model allows to analyze numerically such complex systems of very large size. The comparison of computational results with observational data can provide the quantitative picture of crust magnetic properties. In this section we briefly consider some numerical algorithms for avalanche propagations and results for magnetotransport in terms of avalanche dynamics. As discussed in sect. 5.1 the magnetic field intervals between jumps of nuclide magnetic moments are expected to be large as compared to the disorder. Therefore, we can consider a single jump of the height ν_1 in magnetic moment Eq. (82) at field strength b_1 because of relatively large gaps between the jumps.

6.1. Algorithms for Avalanche Propagation

The evolution of the above (sect. 5) described RJIM model can be simulated numerically by employing various algorithms. In this section we briefly outline some methods for an evolution with increasing and decreasing external fields, which we refer for as magnetizing and demagnetizing, respectively. Since the case of decreasing field is well suited

for practical applications in the crust magnetodynamics we mostly concentrate on such demagnetizing evolution.

The simplest but most time and memory consuming method starts by assigning a random field to each domain-moment on the hypercubic lattice. For the demagnetizing simulations at the beginning all the moments $m_i = \nu_1$ and are pointing along the field. The external field H is then decreased by small increments starting from a large positive value. After each decrease of the field all the domain-moments are inspected to find whether some of them can be triggered to jump (a moment jumps when its effective field changes sign, see Eq. (86) and discussion therein). When a moment jumps the neighbors are checked to satisfy the conditions for the moment to reduce with subsequent examination of next neighbors and so on until no moments are left to jump. Then the external field is further decreased and the process repeated. Since the external magnetic field is decreased by an equal increments a large amount of time is spent searching the lattice for potentially jumping moments. The increments have to be sufficiently large to avoid searching the lattice when there are no jumping moments, but small enough to exclude the case when two or more moments far apart jump at the same field. This method resembles, indeed, an actual crust evolution.

When no jumping moments show up the searching through the lattice can be skipped by using a variation on the described above method. Within such an algorithm one examines all the non-zero moments, finds the next jumping one, and then decreases the external field $H(t)$ to trigger an avalanche. This algorithm is rather efficient for small disorders, since the average searching time for a jump becomes small. However, at over-critical disorders such a method is still very time consuming. Far above from the critical point, where moments tend to jump independently of each other, the checking time scales as N^2 with the number of domain-moments N in the system.

The searching time can be further decreased when the random fields are initially ordered in a list. The 'top' of the list is occupied by the first jumping moment, i.e. the smallest random field for demagnetizing evolution and the largest one for magnetizing direction. The external field is decreased until the effective field of the top moment become b_1, and the moment jumps. We then inspect its nearest neighbors, and the subsequent one, while keeping the external field constant. When no moments are left to jump, the external field needs to be reduced again. The change in the external field δH which is required to induce a jump of the next moment is found by looking for the moment with the random field f_i satisfying the following inequality

$$f_i < b_1 + \eta \mathcal{P} - (H_{\mathrm{prev}} + \delta H) - \nu_1 n_1 J \,, \tag{88}$$

where H_{prev} denotes the field triggering the previous avalanche, and n_1 is the number of nearest neighbors keeping $m_j = \nu_1$ for a moment m_i with the coordination number k.

In general, as a minimum there are $k + 1$ moments from the list to be checked, since the number n_1 can have the integer value between zero and k. We trigger to jump the moment with the random field f_i which satisfies Eq. (88) for the smallest δH, and with the number of non-zero neighbors n_1. It is required to inspect, in fact, more than $k + 1$ moments because moment random field can satisfy Eq. (88) for some value of n_1 but might not have sufficient number of zero moment neighbors, or the moment might be already zero. Since not all the moments have to be examined in order to find the next jumping one this algorithm decreases the searching time. In practice, within such a method about half of the time is spent for the $N \log_2 N$ initial sorting of the list of random field numbers, where N is the total number of domains in the system. Some disadvantage of this method (similar to those mentioned above) consists in the huge amount of storage space required to keep random fields, positions, and values of each moment. This becomes particularly complicated for simulations of large size systems.

The problem of a large storage space can be overcome by exploiting somewhat more sophisticated algorithms making use of an idea that the change δH in the external field between two avalanches follows a probability distribution. Such a probability is associated with the random fields f_i satisfying the gaussian distribution. Therefore, the increments δH in the external field can be chosen according to that distribution as well. The probability density itself is not, in principle, known explicitly. However, an integral value from 0 to some finite strength increment δH of such a probability density can be evaluated. Such an integral just corresponds to the probability $w_{\mathrm{syst}}^0(\delta H)$ that no moment jumps in the entire system during a field change less than the value δH. This quantity can be calculated according to the relation

$$w_{\mathrm{syst}}^0(\delta H) = \Pi_{n_1} \, w_{n_1}^0(\delta H), \tag{89}$$

where the product is taken over $n_1 = 0, 1, 2 \ldots k$, and $w_{n_1}^0(\delta H)$ denotes the probability for remaining a constant non-zero moment $m_i = \nu_1$ with n_1 non-zero nearest neighbors when the external field changes less than δH

$$w_{n_1}^0(\delta H) = \left(1 - \int_{\Delta b^{\mathrm{next}}(n_1)}^{\Delta b(n_1)} W(f) \, df / w_{n_1}^{\mathrm{nojump}}\left(\Delta b(n_1)\right)\right)^{N_{n_1}}. \tag{90}$$

The function $W(f)$ represents the random field distribution function (cf. Eq. (79)), while $\Delta b(n_1)$ and $\Delta b^{\mathrm{next}}(n_1)$ are defined respectively as

$$\Delta b(n_1) = b_1 + \eta \mathcal{P} - H - \nu_1 n_1 J, \tag{91}$$

$$\Delta b^{\mathrm{next}}(n_1) = b_1 + \eta \mathcal{P} - H - \delta H - n_1 J. \tag{92}$$

The quantity $w_{n_1}^{\mathrm{nojump}}(b)$ indicates the probability that a moment with n_1 non-zero nearest neighbors is unchanged until the field reaches the external magnetic field value H

$$w_{n_1}^{\mathrm{nojump}}\left(\Delta b(n_1)\right) = \int_{-\infty}^{\Delta b(n_1)} W(f) \, df = \mathrm{erfc}(\Delta b(n_1)/\sqrt{2}R). \tag{93}$$

In the second equality of Eq. (93) we have used an explicit form Eq. (79) for the random field distribution function $W(f)$. The quantity N_{n_1} in Eq. (90) represents the number of vanished moments with n_1 non-zero neighbors.

For certain probability $w_{\text{syst}}^0(\delta H) = p$ the required field increment δH is found by solving Eq. (89) for δH. In practice, such probability p can be chosen, e.g., as a random number uniformly distributed between zero and one. Once the increment δH is determined we find the next jumping moment. We first calculate the probability $w^{\text{jump}}(n_1)$ that associated with n_1 non-zero neighbors non-zero moment $m_i = \nu_1$ jumps to zero within an interval $[H, H + \delta H]$

$$w^{\text{jump}}(n_1) = \frac{R_{n_1}}{R_{\text{tot}}},\qquad(94)$$

where

$$R_{n_1} = \frac{N_{n1}\, W\!\left(\Delta b^{\text{next}}(n_1)\right)}{w_{n_1}^{\text{nojump}}\!\left(\Delta b^{\text{next}}(n_1)\right)}\qquad(95)$$

gives a jump rate for non-zero moments with n_1 non-zero neighbors, while R_{tot} denotes the sum of the rates R_{n_1} which is taken over the index n_1. The jumping moment has l non-zero neighbors which are found by satisfying the following inequality

$$\sum_{n_1=0}^{l} w^{\text{jump}}(n_1) > p > \sum_{n_1=0}^{l-1} w^{\text{jump}}(n_1)\qquad(96)$$

where the cutoff p is chosen as a random number between 0 and 1. Once l is known, a moment is then randomly picked from the list of non-zero moments with l non-zero neighbors.

Thus, when the first moment has jumped, we check the neighbors. Let assume that one of the neighbors corresponds to the moment $m_i = \nu_1$ and has $(n_1 + 1)$ nearest neighbors with the same moment. Then its probability to jump, while the field approaches $H + \delta H$, is evaluated to be

$$
\begin{aligned}
w_{\text{next}}(n_1, H + \delta H) &= 1 - \frac{\int_{-\infty}^{\Delta b^{\text{next}}(n_1+1)} W(f)\, df}{\int_{-\infty}^{\Delta b^{\text{next}}(n_1)} W(f)\, df}\\[2mm]
&= 1 - \frac{\text{erfc}(\Delta b(n_1 + 1)/\sqrt{2}R)}{\text{erfc}(\Delta b(n_1)/\sqrt{2}R)}.
\end{aligned}\qquad(97)
$$

Here we have employed again an explicit form Eq. (79) in the second equality of Eq. (97). When all the neighbors are inspected, the size of the avalanche is stored, as well as all the other observables. The external magnetic field H is then incremented again by making use of Eq. (89) as to find the next step δH.

Within this method the random fields are not assigned to the moments at the beginning of the simulation and, therefore, are not stored. This represents an important feature of the algorithm which is useful for large system sizes, since memory requirements is significantly reduced.
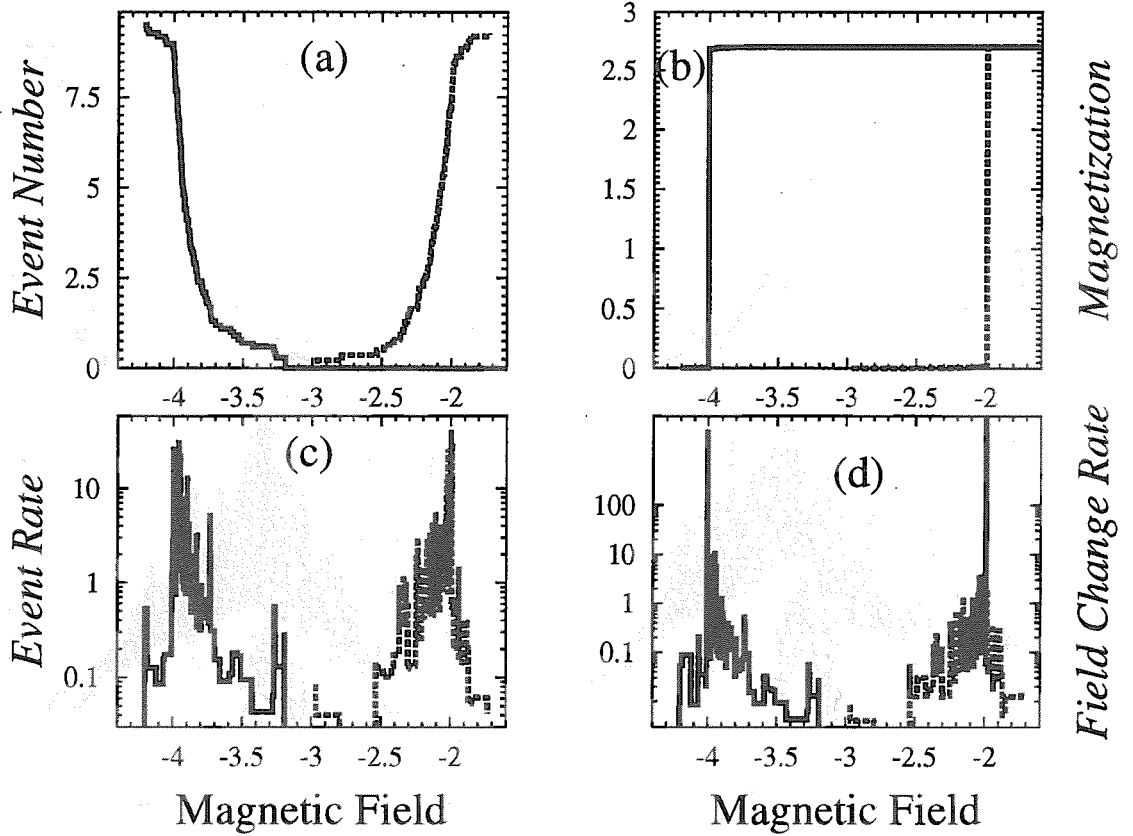
Fig. 20.— Magnetization curves for the cubic lattice of a size $(30)^3$ at the disorder $R = 1.1$ and demagnetizing parameter $\eta = 0$. The solid lines denote the demagnetizing evolution, while magnetizing direction is indicated by dashed lines. Total number of avalanches (the left upper part – a), the magnetization (in units of 10^4 domains, the right upper part – b), the rate of the avalanche number (the left bottom part – c), and of the change of magnetization (in 10^4 domains per field unit, the right bottom part – d) are shown as a function of the magnetic field measured in the units of the coupling constant.

6.2. Magnetization Curves from Simulations

In this section we present some numerical results for the magnetization curves at various values of the crust parameters. We at first neglect the demagnetizing energy, i.e. assume $\eta = 0$, in order to analyze also the sensitivity of magnetotransport phenomena to the choice of the Hamiltonian.

The case of the subcritical value of the disorder parameter is shown in fig. 20. We see very pronounced hysteresis in the magnetization versus the magnetic field (see panel (b) of fig. 20). In fact, the change of overall magnetization is rather rapid in this case and shows diverging slope. From the comparison of magnetization curves with magnetic field dependence of avalanche numbers (panel (a)) we see that the total number changes sharply in the vicinity of the magnetization-step. This corroborates the magnetic field dependence of the rate of the avalanche number shown in panel (c) of fig. 20. The change rates of the magnetization (panel (d)) suggest, however, that the magnetization jumps in
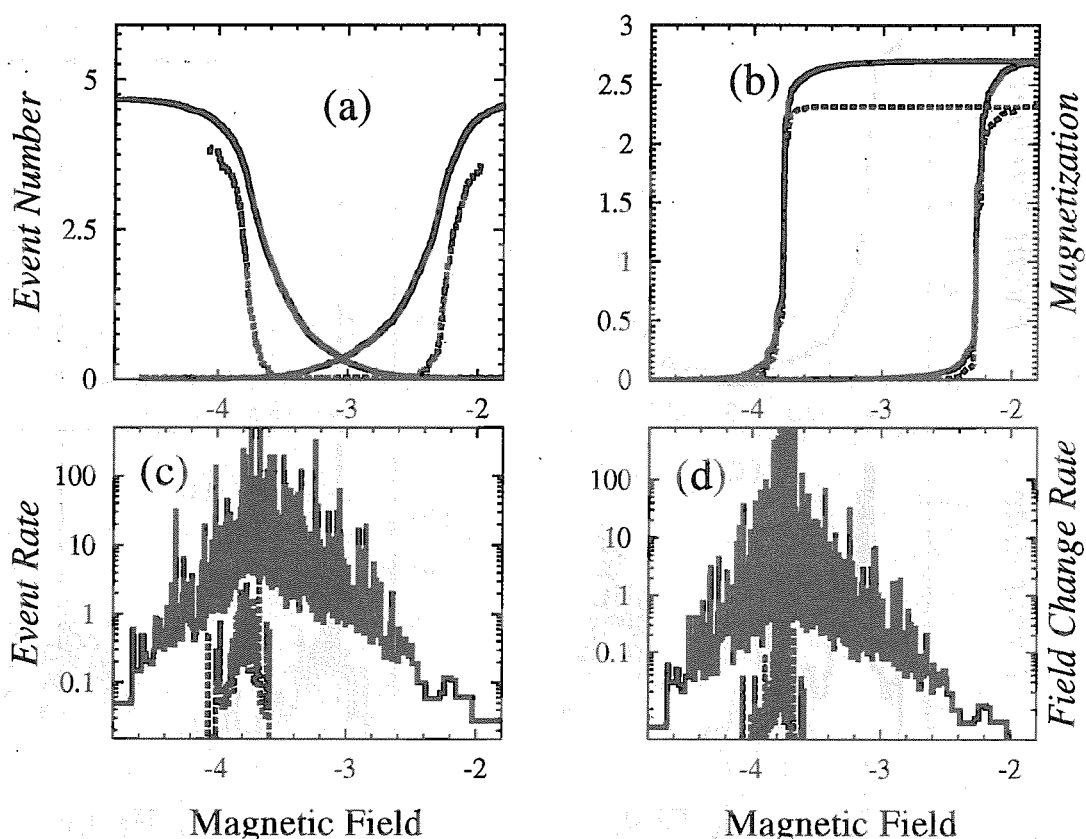
Fig. 21.— Magnetization curves at $R = 1.7$. The parts (a)–(d) represent the same observables as in fig. 20. However, the top part (i.e. panels (a) and (b)) displays magnetizing as well as demagnetizing dynamics, while the bottom part (i.e. panels (c) and (d)) shows the results only for demagnetizing direction. The quantities indicated by solid lines include all avalanches, while dashed lines correspond the large avalanches, i.e. spanning large number of domains with $S > 20$. The avalanche number is in the units of 300 for total and 30 for large avalanches, while the event rates are in the units of 100 and 1000 avalanches per field unit, respectively. The magnetization is given in 10^4 domains, and the field change rates are in units of 1000 and 10^6 domains per field unit for total number and large avalanches, correspondingly.

panel (b) are due to avalanches which span almost entire lattice.

As seen from fig. 21 the magnetodynamics in the vicinity of the critical point display diverging slope with slightly smaller hysteresis as compared to the subcritical conditions (cf. fig. 20). However, the number of avalanches (panel (a) of fig. 21) varies much smoother with magnetic field and corresponds to a wide non-zero rates shown on panel (c). The large avalanches concentrate in vicinity of fields related to sharp change of the magnetization (cf. panel (b)). We note that the case of subcritical disorder of fig. 20 exhibits only a single large avalanche.

As illustrated in figs. 22 and 23 the hysteresis remains noticeable up to relatively large values of the disorder. At such over-critical disorders the magnetization curve shows always finite slope at macroscopic scale, in contrast to sub-critical and critical magneto-transport. Similarly, the number of avalanches changes almost continuously as a function
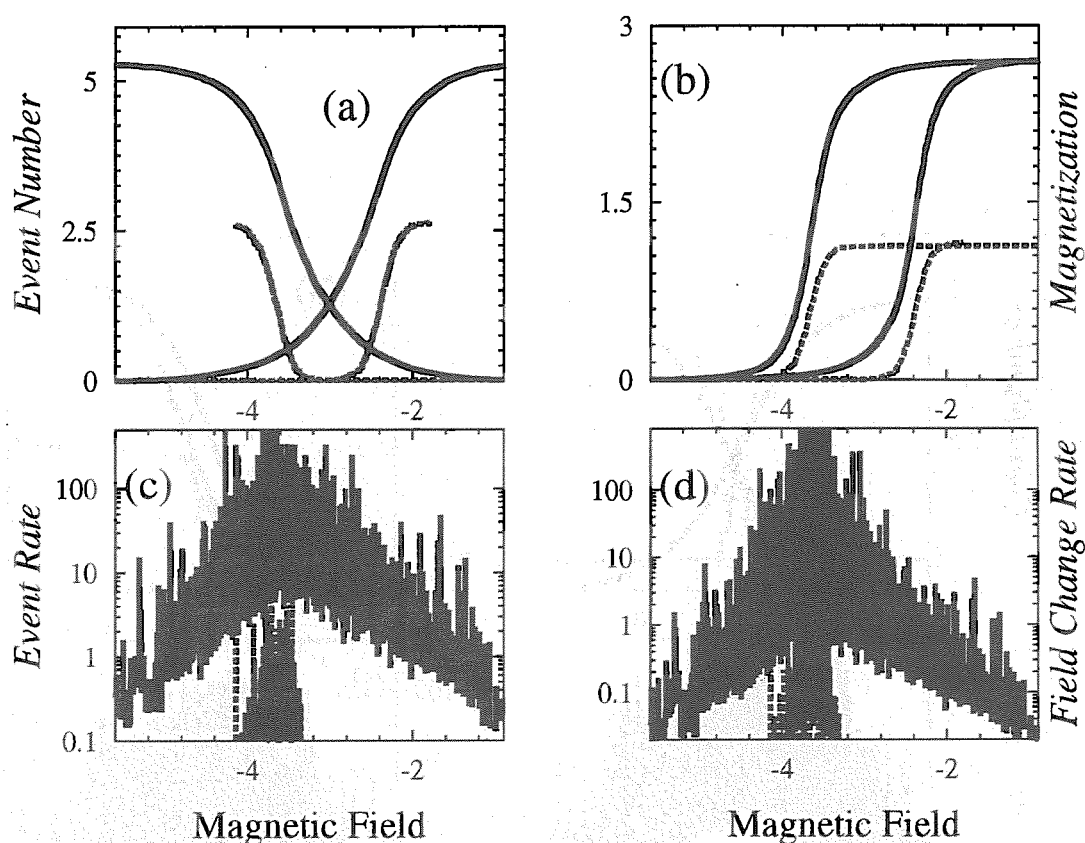
Fig. 22.— Magnetization curves. The same as in fig. 21 but at $R = 2.5$. The avalanche number is in the units of 1000 for total and 100 for large avalanches, while the event rates are in the units of 100 and 2000 avalanches per field unit, respectively. The magnetization is given in 10^4 domains, and the field change rate is in units of 1000 and $2 \cdot 10^5$ domains per field unit for total number and large avalanches, correspondingly.

of magnetic field, while the respective rate indicates that the region of triggering events is even wider than the region of the noticeable hysteresis loop. However, the large size avalanches match an order of magnitude smaller field interval. With further increasing disorder the number of such large size jumps sharply decreases.

Switching on the demagnetizing energy we obtain on the macroscopic scale the finite slope for the magnetization curve also at the critical conditions, see fig. 24.

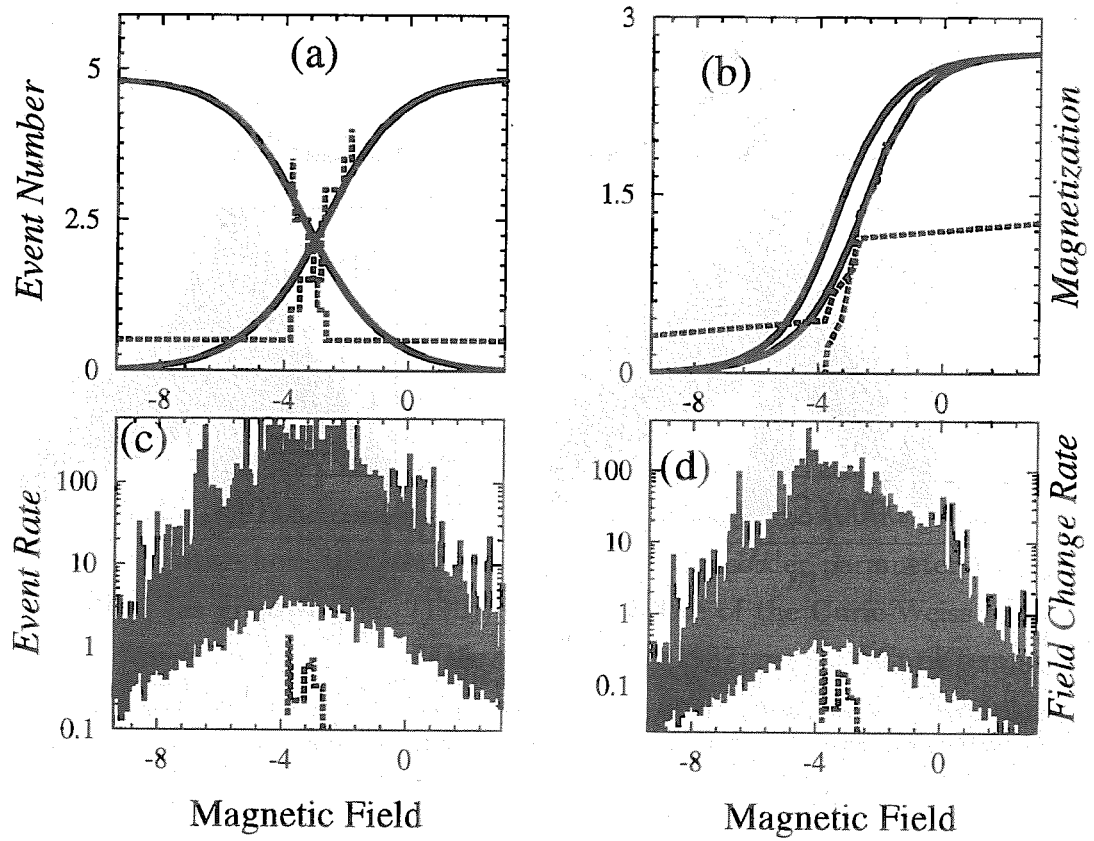Fig. 23.— The same as in fig. 21 but for the disorder $R = 5$. The avalanche number is in the units of 2000 for total and 2 for large avalanches, while the event rates are in the units of 100 and 10 avalanches per field unit, respectively. The magnetization is given in 10^4 domains for total set of avalanches and 100 for large avalanches, and the field change rate is in units of 1000 for both cases.
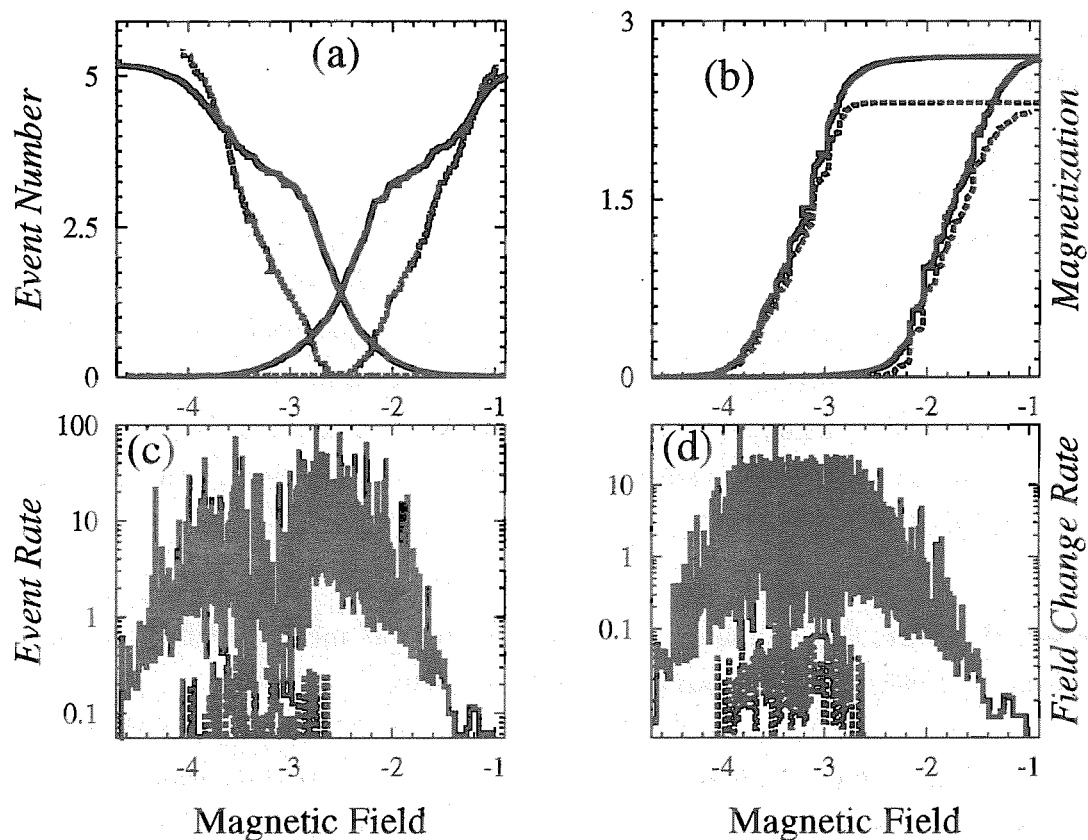
Fig. 24.— The same as in fig. 21 but including the demagnetizing energy with $\eta = 1$. The avalanche number is in the units of 300 for total and 30 for large avalanches, while the event rates are in the units of 100 and 1000 avalanches per field unit, respectively. The magnetization is given in 10^4 domains, and the field change rate is in units of 1000 and $3 \cdot 10^5$ domains per field unit for total number and large avalanches, correspondingly.

7. Mean-Field Approximation

The general properties of the nonequilibrium model corresponding to the Hamiltonian Eq. (85) can be clearly seen by employing the mean-field approximation which assumes an equal interaction strength between the crust domains (i.e. all domain-moments act as nearest neighbors). The coupling is of a strength $J_{ij} = J/\Pi$, where Π is again the total number of moments. The Hamiltonian then takes the simplified form

$$\mathcal{H} = -\sum_i (J_{\text{eff}}\mathcal{P} + H + f_i)m_i \tag{98}$$

with an effectively reduced coupling constant $J_{\text{eff}} = J - \eta$ because of the demagnetizing effect. In the same way as in the Curie-Weiss mean-field theory (see, e.g., Stanley 1987) for the Ising model the interaction of a moment with neighbor one is replaced by the interaction with the overall magnetization $\mathcal{P}$ of the system. This would be, indeed, the correct Hamiltonian when the coupling constant for all the moment pairs would be the same, i.e. for infinite range interactions. For such a case the local field of each side, Eq. (86), is reduced to the form

$$b_i = J_{\text{eff}}\mathcal{P} + H + f_i. \tag{99}$$

We see, therefore, that random fields can be viewed as mean-field fluctuations (cf, e.g., Kondratyev 1994, 1996, Kondratyev & Di Toro 1996).

It turns out that such simplified treatment already reflects most of the essential features of the long-length scale behavior of the system in finite dimensions, e.g., the model exhibits hysteresis, while sweeping the external field through the value b_n (cf. sect. 6.2) . At growing disorder one finds a continuous transition from the case of the macroscopic discontinuity in the magnetization (corresponding to an avalanche spanning almost entire sample) to the series of magnetic jumps of the smallest size. At transitional values of the disorder the system displays the power law distributions of noise (avalanches) and an universal behavior providing thereby criticality signals.

7.1. Magnetization Curves and Equation of State

To investigate the magnetization versus an external field H we consider initially the case $b_{n+1} \gg H \gg b_n$ when all sides have finite value of the moment $m_i = v_n$ and they are directed along the field vector $\mathbf{H}$. At adiabatically decreasing field each moment m_i exhibits a jump at a position of the level crossing, i.e. when its local effective field $b_i = J_{\text{eff}}\mathcal{P} + H + f_i$ passes the value b_n. At a given field strength H all moments with the side local field $b_i > b_n \Leftrightarrow f_i > b_n - J_{\text{eff}}\mathcal{P} - H$ have the value v_n and point along the field vector, while all moments with $b_i < b_n \Leftrightarrow f_i < b_n - J_{\text{eff}}\mathcal{P} - H$ are reduced to v_{n-1}. For the ensemble average $\bar{\mathcal{P}}$ of the magnetization $\mathcal{P}$ defined by Eq. (83) we find
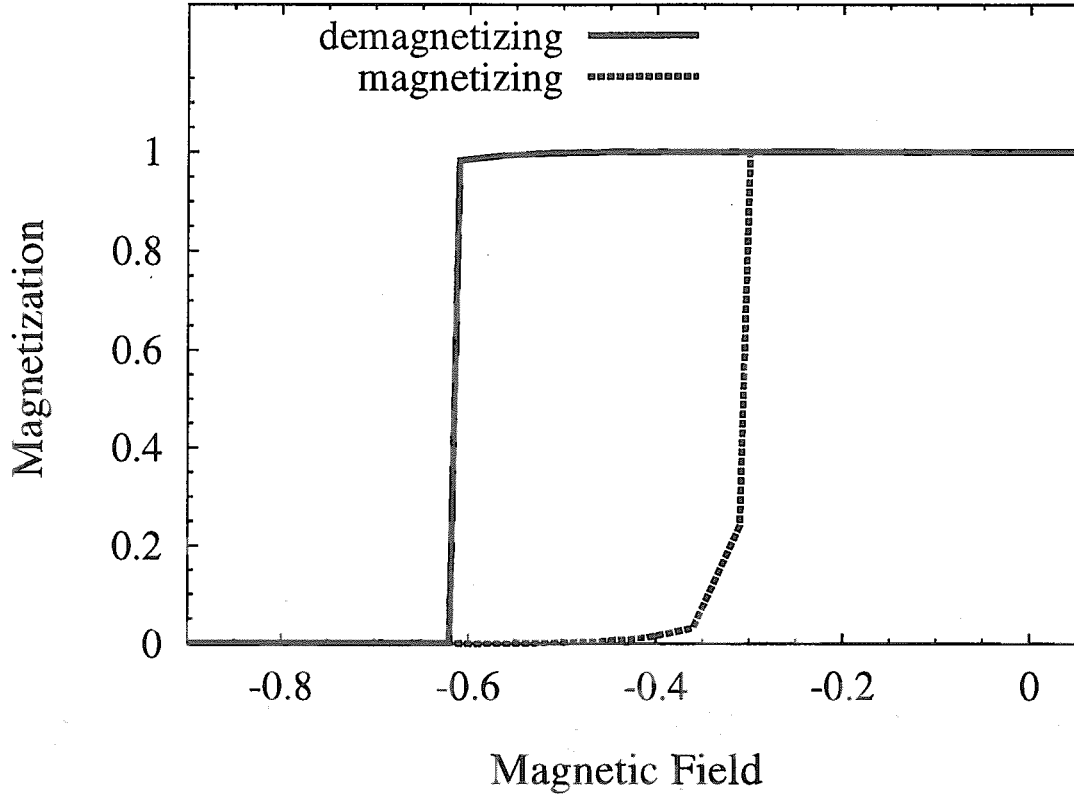
Fig. 25.— Mean-field magnetization curves at the disorder $R = R_c/2$. The solid line denotes the demagnetizing evolution, while the magnetizing direction is indicated by dashed line.

the self-consistency equality

$$\bar{\mathcal{P}} = \int W(f)m_i \, df \tag{100}$$

which gives the relation between the averaged mean-field magnetization and the external field H. The step-wise m_i (see Eq. (82)) yields the self-consistency equation in the form

$$\bar{\mathcal{P}} = v_{n-1} + \nu_n \int_{b_n - J_{\mathrm{eff}} \mathcal{P} - H}^{b_{n+1} - J_{\mathrm{eff}} \mathcal{P} - H} W(f) \, df. \tag{101}$$

Here we have accounted for the relation $v_n - v_{n-1} = \nu_n$ which is obvious from Eq. (82).

We assume the inequalities $b_{n+1} - b_n \gg b_{n+1} - J_{\mathrm{eff}}\mathcal{P} - H \gg R$ and replace in Eq. (101) the upper integration limit by ∞. Then making use of the functional form Eq. (79) we derive the magnetic Equation of State (MEoS)

$$\varpi = 2\frac{v_{n-1}}{\nu_n} + \mathrm{erf}\left[\frac{\varpi + \mathcal{B}_n}{\varrho}\right] \tag{102}$$

which is expressed in terms of reduced magnetization $\varpi = 2\bar{\mathcal{P}}/\nu_n - 1$, disorder $\varrho = 2\sqrt{2}R/J_{\mathrm{eff}}\nu_n$, and external field $\mathcal{B}_n = 1 + 2(H - b_n)/J_{\mathrm{eff}}\nu_n$. The error function $\mathrm{erf}(h) = 2\pi^{-1/2}\int_0^x \exp\{-y^2\}dy$.

The corresponding to MEoS Eq. (102) magnetization curves are displayed in figs. 25, 26, and 27 for various disorders. At small values (i.e. subcritical region, see fig. 25)
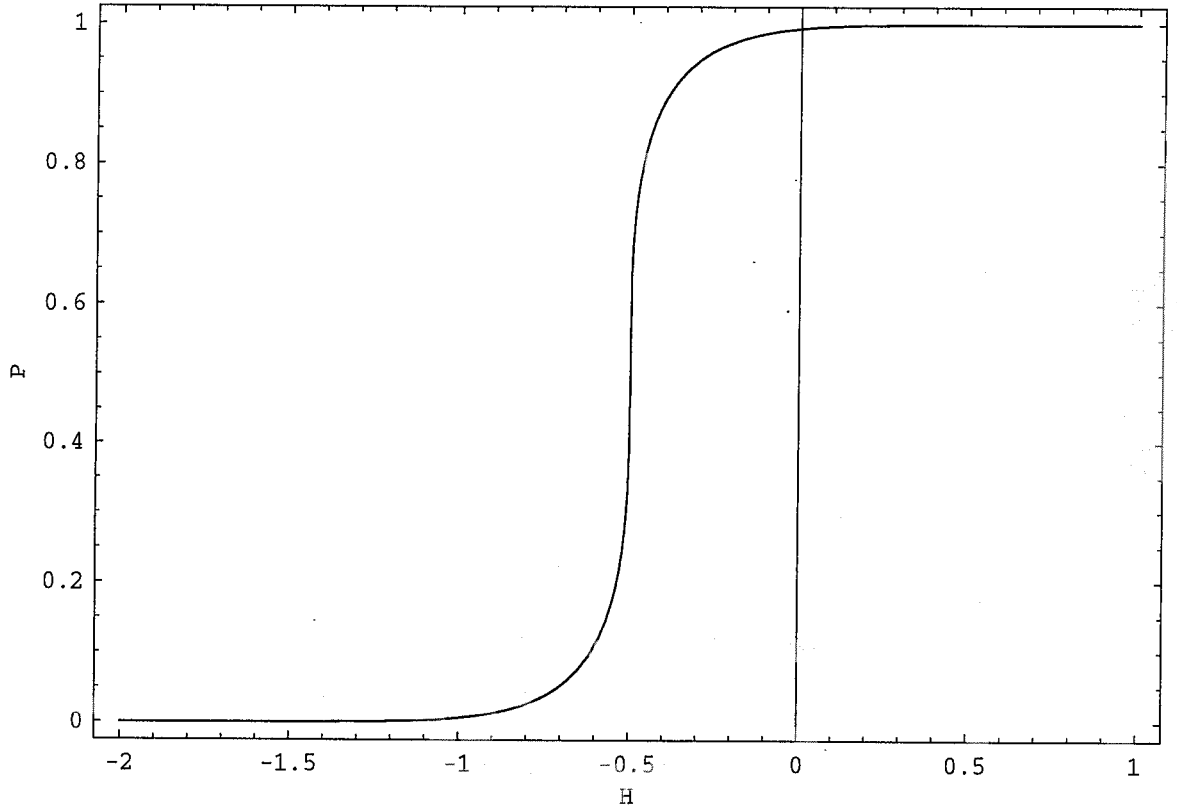
Fig. 26.— Mean-field magnetization curve at the disorder $R = R_c$.

the curve shows the magnetic hysteresis similarly to simulation results (cf. fig. 20 of sect. 6.2 and discussion therein). The magnetization changes step-wise indicating thereby diverging slope at critical fields. The hysteresis gap decreases with increasing disorder. In contrast to simulation results the mean-field approximation yields vanishing hysteresis loop above the critical point. As shown in fig. 26 at critical disorder the magnetization curve exhibits the diverging slope as well, while the slope become finite for over-critical conditions. Such properties are in agreement with the simulations, cf. figs. 20 – 23 of sect. 6.2 and discussion therein.

It is worthy to stress here that the relation Eq. (102) gives the continuous dependence of the magnetization as a function of external field since it corresponds to the smoothed quantity $\bar{P}$ associated with the ensemble average over magnetization events. The individual events, however, represent the magnetization (or demagnetization) processes as successive erratic jumps between metastable states.

7.2.   Mean-Field Phase Diagram

Employing the mean-field MEoS Eq. (102) we consider some general magnetic properties of a crust with respect to the position in $\{H, R\}$-plane corresponding to strengths H
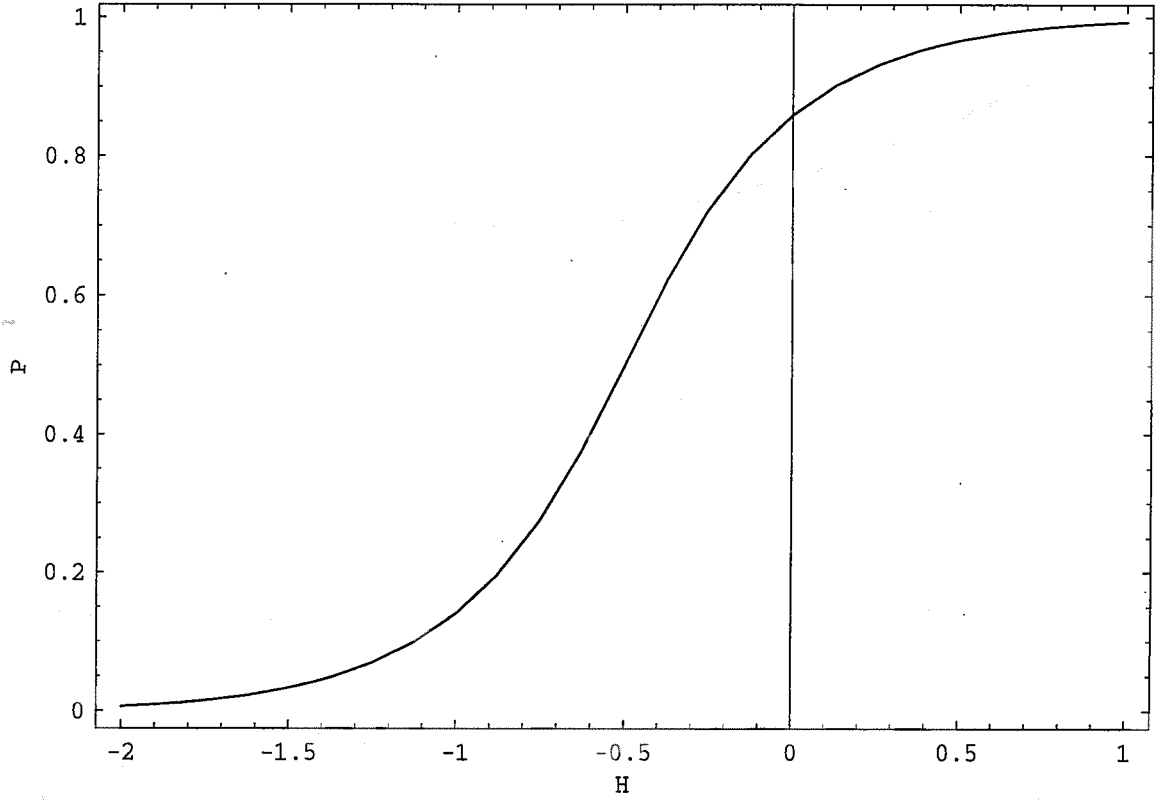
Fig. 27.— Mean-field magnetization curve at the disorder $R = R_c$.

around the value b_n. Making use of Eqs. (3) and (102) we find the magnetic susceptibility of interacting nuclei in the form

$$\chi = \mathrm{d}\bar{\mathcal{P}}/\mathrm{d}H = \nu_n W(h)/(-t(h)) \tag{103}$$

with $h = b_n - J_{\mathrm{eff}}\bar{\mathcal{P}} - H$ and

$$t(h) = \nu_n J_{\mathrm{eff}} W(b_n - J_{\mathrm{eff}}\bar{\mathcal{P}} - H) - 1 . \tag{104}$$

The singularities of the susceptibility given by roots of the function $t(h)$ (i.e. solutions of $t(h_c) = 0$) define the critical conditions h_c. Such solutions never exist for real values of the field H at large disorders $R > \nu_n J_{\mathrm{eff}}/\sqrt{2\pi} \equiv R_c$, when the function $t(h)$ is negative at any field H, while the value of χ and the slope of magnetization curve are always finite. Correspondingly, for such disorders the solution $\bar{\mathcal{P}}(H)$ of Eq. (102) is analytic at all values of H, indicating thereby the stable regime of magnetic field evolution.

For $R \leq R_c$, however, the condition $t(h_c) = 0$ is fulfilled at critical fields $H_c(R)$. Applying the functional form Eq. (79) we find two roots

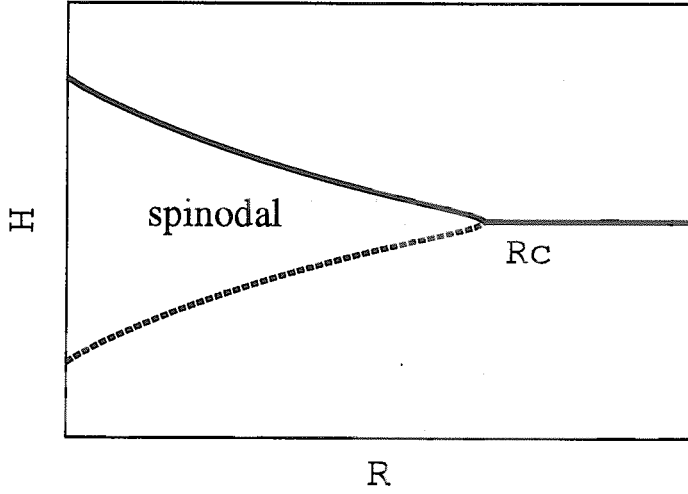$$h_c = \pm\sqrt{\ln(\nu_n J_{\mathrm{eff}}/\sqrt{2\pi}R)} . \tag{105}$$

Fig. 28.— The mean-field phase diagram for the RJIM model Eq. (98). The upper H_c^u (solid line) and low H_c^l (dashed line) coercive fields meet at the critical point $H_c(R_c) = b_1 - J_{eff}\nu_1/2$.

Using the mean-field MEoS Eq. (102) again we obtain the strengths

$$
H_c^{u/l}(R) = b_n - \frac{\nu_n J_{eff}}{2} \tag{106}
$$
$$
\pm \left(\frac{\pi R}{2\sqrt{2}} \sqrt{\ln(\nu_n J_{eff}/\sqrt{2\pi}R)} - \frac{\nu_n J_{eff}}{2} \text{erf}[\sqrt{\ln(\nu_n J_{eff}/\sqrt{2\pi}R)}] \right)
$$

with '−' and '+' corresponding to low $H_c^l(R)$ and upper $H_c^u(R)$ critical fields, respectively. At magnetic fields far from the conditions of level crossings, e.g., $b_{n-1} \ll H \ll b_{n+1}$, the crust experiences a stable phase.

The phase diagram obtained within the mean-field treatment is shown in fig. 28. The spinodal regions are located between the fields $H_c^l(R)$ and $H_c^u(R)$ (i.e. at the field strengths corresponding to the level crossings of crust nuclei) which meet at the critical point. At such critical values of disorder $R = R_c$ and magnetic field $\mathcal{B}_n^c(R_c) = 0$ the magnetization curve $\bar{\mathcal{P}}(H)$ shows diverging slope. For $R < R_c$ the solution $\bar{\mathcal{P}}(H)$ is unique only for H outside of a certain interval $[H_c^l(R), H_c^u(R)]$. In the range between the two "coercive fields" $H_c^l(R)$ and $H_c^u(R)$, the equation has three solutions, two − stable and one − unstable. Unlike equilibrium systems which in zero temperature limit always occupy the state with the lowest overall free energy, the considered nonequilibrium system is trapped due to the specific local dynamics in the current metastable state (i.e. local energy minimum) until

it is destabilized by the external magnetic field. For decreasing external magnetic field such a behavior implies that the system always remains in the metastable state with the largest possible magnetization. On the other hand, for increasing external magnetic field, the system is located in the metastable state with the smallest possible magnetization. As a consequence one obtains a hysteresis loop for $\mathcal{P}(H)$ with macroscopic discontinuities at the upper and lower critical fields $H_c^u(R)$ and $H_c^l(R)$, respectively (see fig. 25).

7.3. Scaling Relations

At critical conditions the system displays some universal scaling behavior which we analyze by considering respective singularities of magnetic susceptibility. To obtain potential scaling behavior in the vicinity of such conditions we expand the denominator of magnetic susceptibility Eq. (103) $t(h)$ around critical values $h_c = b_n - J_{\text{eff}}\mathcal{P}(H_c(R)) - H_c(R)$

$$
\begin{aligned}
t & = \nu_n J_{\text{eff}} W(h) - 1 = -1 + \nu_n J_{\text{eff}}(W(h_c) \\
& + W'(h_c)(h - h_c) + (1/2)W''(h_c)(h - h_c)^2 + \cdots)
\end{aligned}
\tag{107}
$$

Since by definition of h_c

$$
t(h_c) = \nu_n J_{\text{eff}} W(h_c) - 1 = 0
\tag{108}
$$

we find for the singularity of magnetic susceptibility at small values $(h - h_c)$ the following form

$$
\begin{aligned}
\chi & \equiv \mathrm{d}\bar{\mathcal{P}}/\mathrm{d}H \\
& = (-W(h_c))/(J_{\text{eff}}(W'(h_c)(h - h_c) + 1/2W''(h_c)(h - h_c)^2 + \cdots)).
\end{aligned}
\tag{109}
$$

For general analytic form of random field distributions $W(h)$ with a single maximum and nonvanishing second derivative $(W''(h_c) < 0)$ the form Eq. (109) of the singularities suggests two different scaling behaviors which can be classified with respect to the cases $W'(h_c) = 0$ and $W'(h_c) \neq 0$.

We at first consider the case of vanishing first derivative of the distribution function at critical conditions $W'(h_c) = 0$. For a Gaussian distribution of width $R = R_c$ with zero mean value such a condition corresponds to the relation $h_c = b_n - J_{\text{eff}}\mathcal{P}(H_c) - H_c = 0$ and, consequently, leads to the equalities $W(h_c) = 1/(\sqrt{2\pi}R_c)$ and $W''(h_c) = 1/(\sqrt{2\pi}R_c^5)$. Using Eq. (108) one obtains $R_c = J_{\text{eff}}\nu_n/\sqrt{2\pi}$. This situation is related, in fact, to the largest possible value of R for which the average magnetization $\mathcal{P}(H)$ exhibits a point of diverging slope within the mean-field approximation.

Integration of Eq. (109) over an external field H leads to a cubic equation for $\Delta\bar{\mathcal{P}} = \mathcal{P} - \mathcal{P}(H_c(R))$ and the leading order scaling behavior in the vicinity of the critical point (i.e. for small $\Delta H = H - H_c(R_c)$ and $r = (R_c - R)/R \ll 1$)

$$
\Delta\bar{\mathcal{P}}(r, \Delta H) \sim |r|^\beta \mathcal{M}_\pm(\Delta H/|r|^{\beta\delta}),
\tag{110}
$$

where the mean-field theory predicts the critical exponent $\delta = 3$, while the function $\mathcal{M}_\pm$ is given by the smallest real root $\mathcal{G}_\pm(y)$ of the cubic equation

$$\mathcal{G}^3 \mp \frac{12}{\pi}\mathcal{G} - \frac{12\sqrt{2}}{\pi^{3/2}R_c}y = 0 \,. \tag{111}$$

Hereafter $\pm$ refers to the sign of r.

In a similar manner for distributions with $R < R_c$ we obtain the relations $W(h_c) = 1/(\nu_n J_{\text{eff}})$ and $W'(h_c) \neq 0$. Integrating Eq. (109) over H at critical conditions $h_c = b_n - J_{\text{eff}}\mathcal{P}(H_c(R)) - H_c(R)$ yields a quadratic equation for the magnetization. Then the scaling behavior reads

$$\Delta\bar{\mathcal{P}} = \bar{\mathcal{P}} - \bar{\mathcal{P}}(H_c(R)) \sim (H - H_c(R))^\zeta \,, \tag{112}$$

where the mean-field critical exponent $\zeta = 1/2$ for H in vicinity of critical field $H_c(R)$. As is evident from Eq. (106) $H_c(R_c) = b_n - J_{\text{eff}}\nu_n/2$, while for small $r > 0$ we obtain $(H_c(R) - b_n - J_{\text{eff}}\nu_n/2) \sim r^{\beta\delta}$ with $\beta\delta = 3/2$. At zero disorder $H_c^u(R = 0) = b_n$, and $H_c^l(R = 0) = b_n - J_{\text{eff}}\nu_n$. The corresponding phase diagram is shown in fig. 28.

It is worthy to notice here that the scaling results for disorder parameters R close to critical values R_c (as given by Eq. (110)) resemble those of the Curie-Weiss mean-field theory for the equilibrium Ising model (see, e.g., Stanley 1987) near the Curie temperature $(T = T_C)$. For the case $T < T_C$ the equilibrium model, however, has a discontinuity in the magnetization at vanishing external field, while for $R < R_c$ RJIM-model displays a jump in the magnetization at a (history dependent) nonzero magnetic field $H_c(R)$, where the corresponding metastable solution becomes unstable. The macroscopically large avalanche lines $H_c^{u/l}(R)$ are in fact similar to the spinodal lines in spinodal decomposition (Stanley 1987). At the same time, the mean-field theory does not show any hysteresis for $R \geq R_c$ (see figs. 26 and 27), in contrast, to numerical results (cf. figs. 20, 21, 22, 23, 24 and discussion therein).

8. Avalanche-Size Distribution

As discussed above the adiabatically varying external magnetic field induces the moment jump avalanches. Due to the ferromagnetic interaction a jumping domain-moment can cause some of the nearest neighbors to jump, which may in turn trigger some of their neighbors, and so on, generating thereby (de)magnetizing avalanche. In this section we demonstrate that in vicinity of critical conditions such a process exhibits some universal statistical properties, in particular, the size (i.e. number of jumped domain-moments) distribution displays a self-similar power-law behavior.
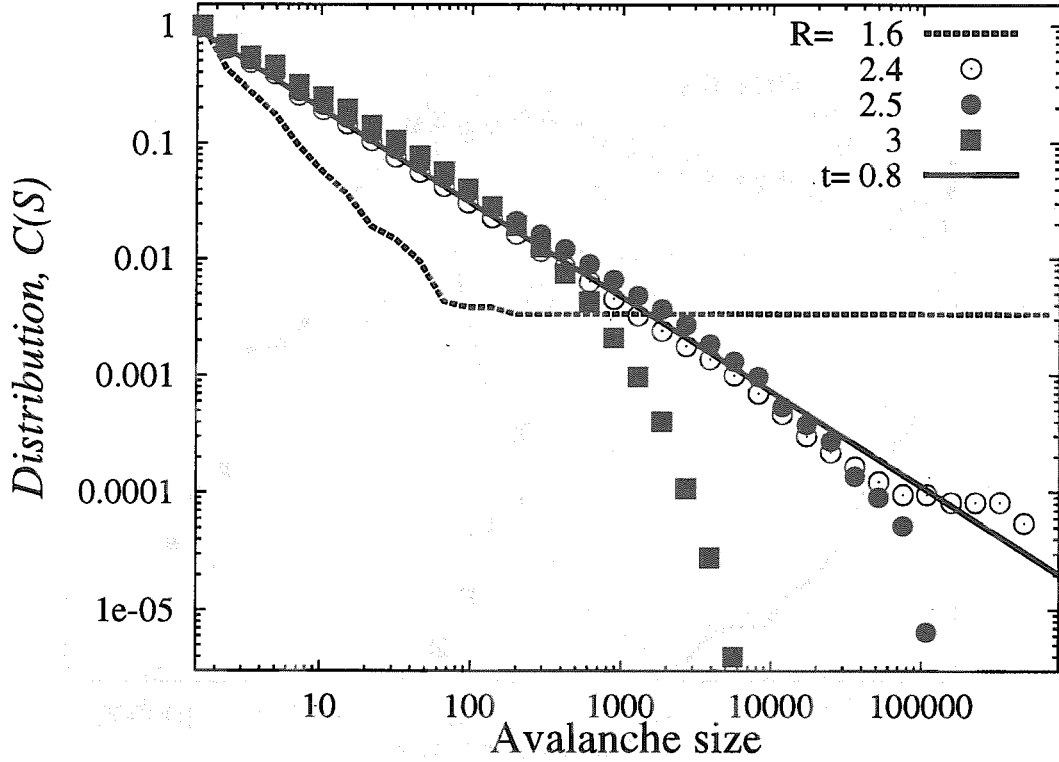
Fig. 29.— Cumulative avalanche size distributions from numerical simulations in demagnetizing direction at zero demagnetization energy, i.e. $\eta = 0$. Results for subcritical disorder $R = 1.6$ are shown by dashed line, the vicinity of critical point $R = 2.4$ and 2.5 are indicated by open and solid circles, respectively, while solid squares correspond to over-critical value $R = 3$. Solid line displays a power law size dependence with an exponent $\tau = 0.8$.

8.1. Simulation Results

As seen from numerical (sect. 6) and mean-field (sect. 7) analysis of the magnetization curves the avalanche sizes depend strongly on the position of a system in $\{R, H\}$-plane. We analyze the size distribution integrated over the demagnetizing branch of the hysteresis loop, i.e. for the decreasing magnetic field H. We consider the cumulative size distribution corresponding to the number of avalanches of a size exceeding certain value

$$C(S) = \sum_{L \geq S} D(L), \qquad (113)$$

where differential size distribution $D(S)$ is proportional to the number of avalanches with the number of jumped domains S. We note that for large sizes $S \gg 1$ the power law distribution $D(S) \sim S^{-\tau}$ yields for Eq. (113) the following relation $C(S) \sim S^{1-\tau} \sim SD(S)$ providing thereby relationship for respective exponents. Employing cumulative values $C(S)$ allows to reduce statistical errors in the data analysis.

For cases of zero demagnetizing energy, i.e. $\eta = 0$, the distributions $C(S)$ are presented in fig. 29. One sees a clear transition from 'U' shape distribution at small disorders to an
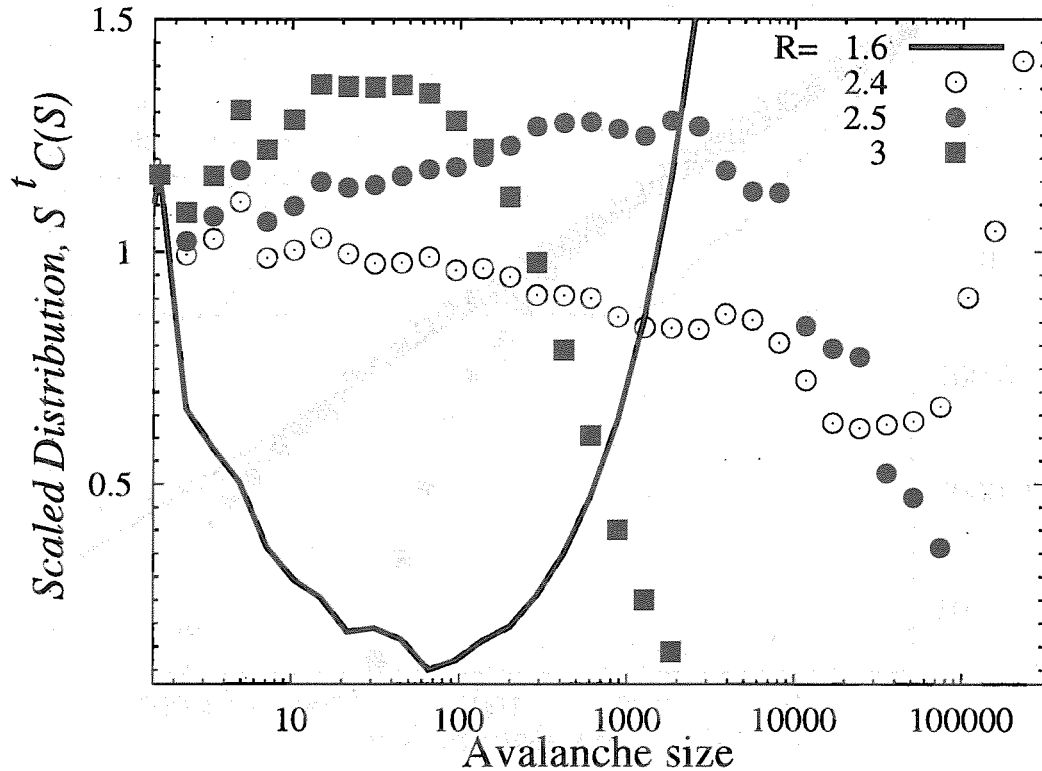
Fig. 30.— The same as fig. 29 for scaled avalanche size distributions, $S^\tau C(S)$.

abrupt exponential suppression of large size avalanches at large disorders. At transitional values the distribution shows a behavior close to the power law dependence with an exponent $\tau \approx 0.8$ corresponding to 1.8 for the differential size distribution (see Eq. (113) and discussion therein) and providing, thereby, a signal for self-organized criticality.

Further visualization of such a signal can be achieved by analyzing scaled avalanche size distribution which is defined as the distribution normalized with respect to the power law, i.e. $C_{\mathrm{scaled}} \sim S^\tau C(S)$. As shown in fig. 30 such a presentation makes rather transparent the change from 'U'-shaped distribution form to the strongly enhanced number of small avalanches and sharp nearly step-like reduction of large sizes.

As illustrated in fig. 31 the large avalanches are suppressed as well due to the effect of demagnetization energy. The effect is particularly pronounced for the scaled avalanche size distribution displayed in fig. 32. One sees that, in addition, demagnetizing effect gives rise to noticeable enhancement in the number of middle size avalanches. Such an enhancement becomes more pronounced with encreasing the demagnetizing energy, i.e. the parameter η.
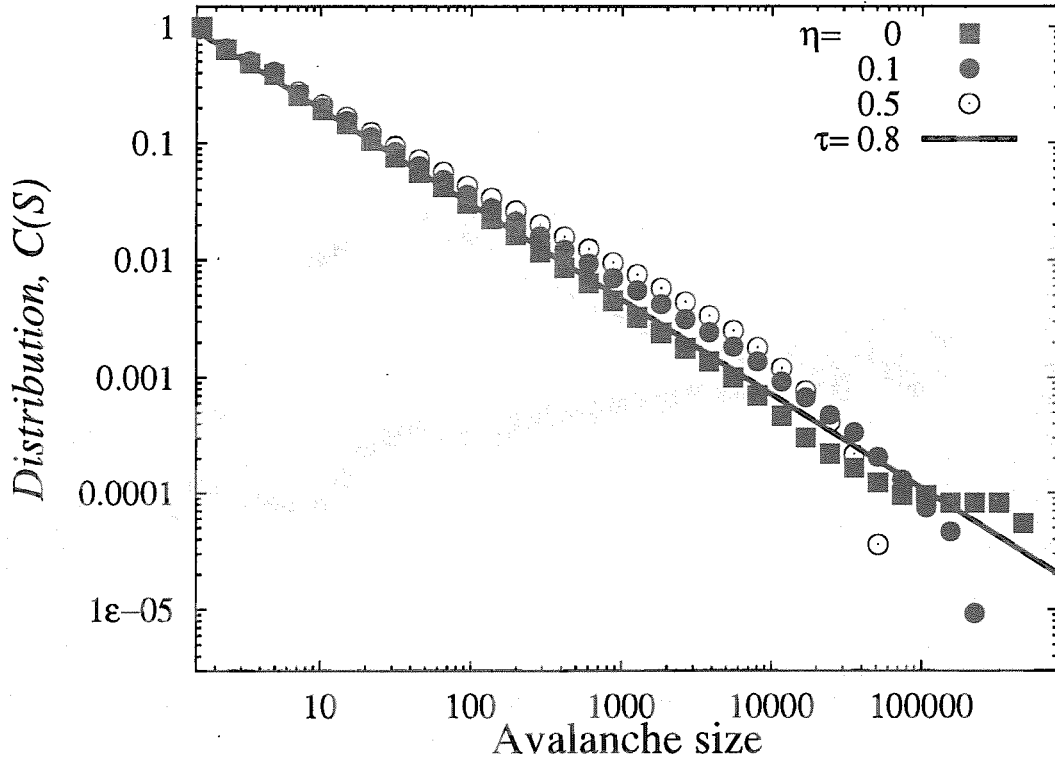
Fig. 31.— Avalanche size distributions at nearly critical disorder $R = 2.4$ and the demagnetizing energy parameters $\eta = 0$ (solid squares), 0.1 (solid circles), 0.5 (open circles). Solid line represents the power law with an exponent $\tau \approx 0.8$.

8.2. Avalanche Sizes within Mean-Field Approximation

The discussed in sect. 8.1 characteristics of numerical results for avalanche size distributions can be understood within the mean-field treatment which is introduced in sect. 7. To consider the distribution properties we first evaluate an average number of the triggered domains per a single jump. Since within the mean-field treatment all the moments are coupled as nearest neighbors with a strength (J_{eff}/Π), the single moment jump from v_n to v_{n-1} changes the effective field of all other moments by a quantity (J_{eff}/Π). Here Π stands for the domain number as in previous sections. In case of a large system with $\Pi \gg 1$ the average number of secondary domain-moments (which are triggered to jump in response to such a change in the effective local field) is then given by

$$\bar{n}_{\text{trig}} \approx (\nu_n J_{\text{eff}}/\Pi)\Pi W(b_n - J_{\text{eff}}\mathcal{P} - H) = \nu_n J_{\text{eff}} W(b_n - J_{\text{eff}}\mathcal{P} - H). \tag{114}$$

When an inequality $\bar{n}_{\text{trig}} < 1$ is satisfied, the avalanches quickly terminate and size distribution displays a suppression for large number of domain jumps. For a case $\bar{n}_{\text{trig}} = 1$ the avalanches are able to sweep almost entire system, since each jumping moment triggers on average one other moment. Such conditions are met when the magnetic field H takes
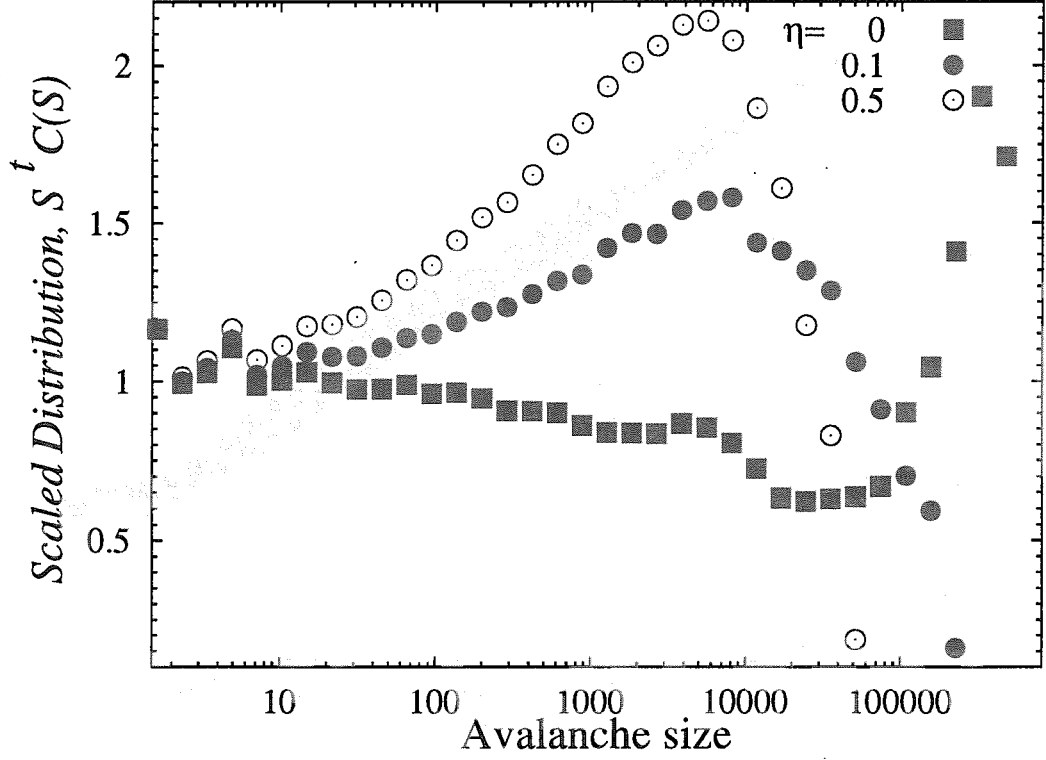
Fig. 32.— The same as fig. 31 for scaled avalanche size distributions, $S^\tau C(S)$.

a value at the macroscopically large ('infinite') avalanche line $H = H_c^{u/1}(R)$ at $R \leq R_c$, since the condition $\bar{n}_{\text{trig}} = 1$ is equivalent to the relation $t = 0$ (cf. Eqs. (104) and (114)).

As is evident from the discussion leading to Eq. (100) an avalanche of the size S in some magnetization event originates from certain configuration of random fields. The probability to find respective configuration and, therefore, an avalanche can be easily evaluated for sufficiently large systems, i.e. for $S \ll \Pi$. Let us assume that the random field f_i on a side i corresponds to the primary moment m_i triggering an avalanche of the size S. This implies that the random fields of exactly $(S - 1)$ sides associated with successive moment jumps are located in the interval $[(f_i - \nu_n S J_{\text{eff}}/\Pi), f_i]$. When the number Π is sufficiently large, i.e. $\nu_n S J_{\text{eff}}/\Pi \ll R$, the probability density of random fields $W(f)$ is approximately constant over this interval. Then the probability $P(S)$ to generate corresponding configuration of random fields is given by the Poisson distribution

$$P(S) = \frac{\lambda^{(S-1)}}{(S - 1)!} \exp(-\lambda) \tag{115}$$

with the average value $\lambda = \nu_n J_{\text{eff}} S W(b_n - J_{\text{eff}}\mathcal{P} - H) = S(t + 1)$, where $t \equiv \bar{n}_{\text{trig}} - 1 = \nu_n J_{\text{eff}} W(b_n - J_{\text{eff}}\mathcal{P} - H) - 1$. We recall in this regards Eq. (104) pointing out thereby the relationship between the average number of triggered moments $\bar{n}_{\text{trig}}$ given by Eq. (114)

and determinator of the magnetic susceptibility.

To obtain the avalanche size distribution $D(S,t)$ the probability $P(S)$ Eq. (115) has to be multiplied by a factor $1/S$, a value corresponding to the probability that among S moments the chosen one has the highest random field and triggers the avalanche. Then accounting for the relationship between λ and t the avalanche size distribution $D(S,t)$ reads

$$D(S,t) = S^{(S-2)}/(S-1)!(t+1)^{(S-1)}e^{-S(t+1)}.\tag{116}$$

It is worthy to clarify further the difference between the probabilities $P(S)$ and $D(S,t)$ expressed by Eqs. (115) and (116), respectively. The probability $P(S)$ includes cases in which the random fields of the S moments are arranged in the interval $[(f_i - \nu_n S J_{\text{eff}}/\Pi), f_i]$ in such a way that they can jump not in one extended avalanche, but rather in some separate avalanches triggered at slightly different external magnetic fields. Imposing periodic boundary conditions on the interval $[(f_i - \nu_n S J_{\text{eff}}/\Pi), f_i]$ it can be seen that for any arrangement of random fields in the interval there is exactly one moment which can trigger the rest in a single extended avalanche. Thus the random field configuration with the smallest random field domain triggering an avalanche is met in $(1/S)$ part of the cases accumulated in the probability $P(S)$. The ratio of the probabilities $P(S)$ and $D(S,t)$ is given then by the total number of moments in the avalanche since the value $D(S,t)$ corresponds specifically to an avalanche of size S starting with a moment jump at a random field $f_i = b_n - J_{\text{eff}}\mathcal{P} - H$.

Employing Stirling's formula

$$S! \approx \sqrt{2\pi} S^{S+1/2} \exp\{-S\}$$

in Eq. (116) we find for large S the relation

$$D(S,t) \sim S^{-3/2} \exp\{-St^2/2\}.\tag{117}$$

The distribution at large sizes is essentially determined by the determinator of magnetic susceptibility which classifies the critical behavior, see Eqs. (107) and (109) as well as discussion therein. To obtain the scaling behavior of avalanche size statistics for two different criticality classes we make use of Eq. (107) for the expansion of $t(h)$ around h_c in the expression Eq. (117).

8.2.1. Avalanche Sizes in the Vicinity of the Critical Point

In the vicinity of the critical point $(R_c, H_c(R_c))$ the relations $h_c = 0$ and $W'(h_c) = 0$ yield an expansion

$$t = \nu_n J_{\text{eff}}(W(0) - 1) + J_{\text{eff}}W''(0)h^2 + O(h^3).\tag{118}$$

Employing Eq. (110) leads to the scaling relation

$$t \sim r[1 \mp 1/4\pi \mathcal{G}_\pm (\Delta H/|r|^{\beta\delta})^2],$$ (119)

where $\mathcal{G}_\pm$ is the solution of Eq. (111), while $\pm$ again refers for the sign of $r = (R_c - R)/R$. Combining Eqs. (117) and (118) we obtain scaling form for the avalanche size distribution in the vicinity of the critical point

$$D(S, r, \Delta H) \sim S^{-\tau} \mathcal{K}_\pm (S/|r|^{-1/\sigma}, \Delta H/|r|^{\beta\delta})$$ (120)

with the mean–field critical exponents $\tau = 3/2$, $\sigma = 1/2$, $\beta\delta = 3/2$, and respective scaling function

$$\mathcal{K}_\pm(x, y) = \frac{1}{\sqrt{2\pi}} e^{-x[1 \mp \frac{\pi}{4}\mathcal{G}_\pm(y)^2]^2/2}.$$ (121)

8.2.2. Avalanche Size Distributions at Critical Fields

Since in the case $R < R_c$ the first derivative of random field distribution is not vanishing $W'(h_c) \neq 0$ the expansion t contains the linear term with the difference $(h - h_c)$ as well

$$
\begin{aligned}
t &= \nu_n J_{\text{eff}} W(h_c) - 1 + \nu_n J_{\text{eff}} W'(h_c)(h - h_c) + \cdots \\
&\approx \nu_n J_{\text{eff}} W'(h_c)(h - h_c) \\
&= -\nu_n J_{\text{eff}} W'(h_c) J_{\text{eff}}(\mathcal{P} - \mathcal{P}(H_c(R))) - \Delta H
\end{aligned}
$$ (122)

Following the steps that led to Eq. (112) we arrive to an expression

$$t = -2\sqrt{J_{\text{eff}} W'(h_c) \Delta H} + O(\Delta H^{3/2})$$ (123)

so that for the field strengths H approaching the onset to macroscopically large (infinite) avalanche (with $H \leq H_c^u(R)$ for increasing field H and $H > H_c^l(R)$ for decreasing field) the avalanche size distribution is given by

$$D(S, \Delta H) \sim S^{-3/2} \exp\left\{-2[W'(h)J_{\text{eff}}]S|\Delta H|\right\}.$$ (124)

This relation can be re-written in more general form

$$D(S, \Delta H) \sim S^{-\tau} \bar{\mathcal{Y}}(S|\Delta H|^{1/\kappa})$$ (125)

with the exponents $\kappa = 1$ and $\tau = 3/2$ in mean-field theory, and corresponding scaling function $\bar{\mathcal{Y}}$.

9. Implications in SGR-Burst Activity

As shown in sects. 5, 6, 7, and 8 the neutron star crust magnetotransport exhibits irregular jumps, when magnetic fields match the vicinity of step-wise anomalies of nuclide
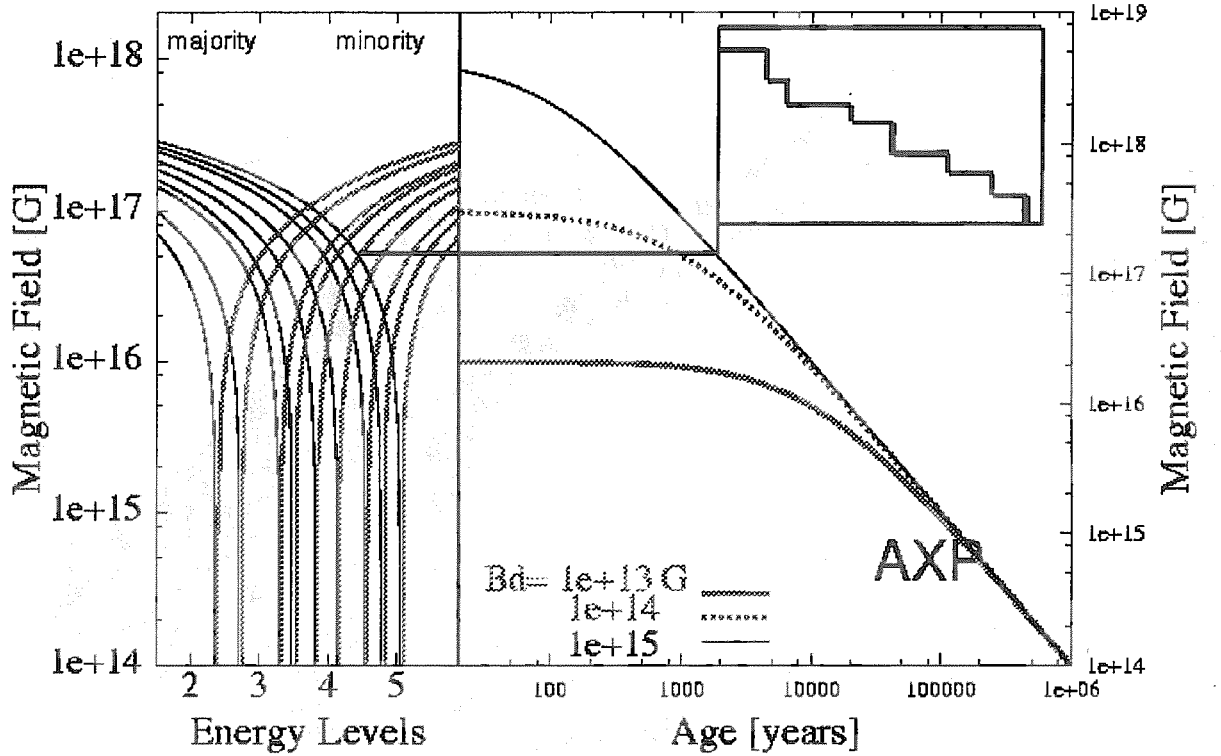
Fig. 33.— Schematic view of neutron star crust magnetotransport. The left panel shows the magnetic field dependence of neutron majority- and minority-spin energy levels for NM, decreasing and increasing with the field, respectively (cf. figs. 12 and 13). The right panel represents the time evolution of overall magnetic field with an inset displaying the magnetodynamics during the active bursting period. The respective level crossing (see text) is indicated by horizontal line intersecting the left and right panels.

magnetic moments. Such an epoch of neutron stars is represented schematically in fig. 33. As shown in the inset of the right panel of fig. 33 the RJIM model confirms very short periods for the burst activity with rather small time intervals between the bursts which are associated with step-like change of the crust magnetic field. Such sharp decrease of the magnetization is caused by avalanches of the magnetic moment jumps due to ferromagnetic coupling between nuclides. The proportional to the avalanche size excess of magnetic energy is released to the magnetosphere. Assuming the field strength $H \sim 10^{16.5}$ G in the outer crust of a linear size $l_{crust} \sim 100$ m and employing an estimate Eq. (74) the energy upper limit is evaluated

$$E_{max}^{SGR} \approx H \mathcal{P} l_{crust}^3 \sim 10^{42} \text{ ergs} \qquad (126)$$

to be in a good agreement with SGR-burst observations, the detailed comparison is given in sect. 9.1. This energy is larger by about 30 orders of magnitude as compared to the case of magnetic Barkhausen emission (see Eq. (73) and discussion therein). When the de-magnetization jumps involve the inner crust as well, the linear size is an order of
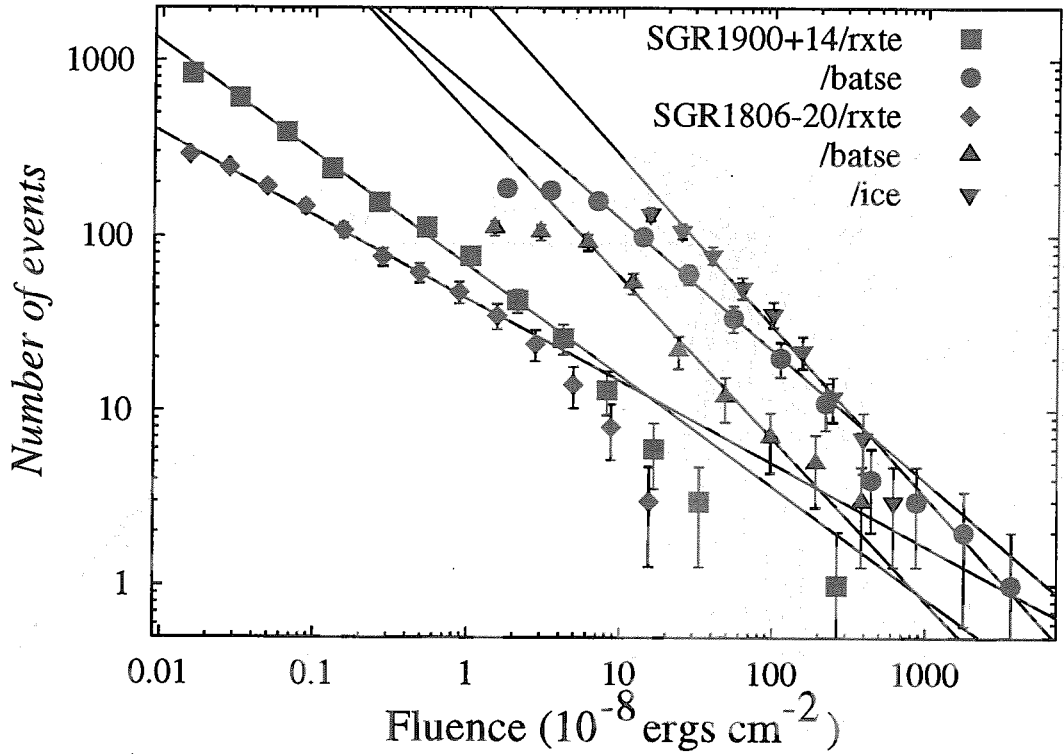
Fig. 34.— Cumulative fluence distribution of SGR-bursts as observed by various missions. SGR 1900+14 bursts from (Gögüs et al. 1999) are shown by squares (RXTE) and circles (BATSE). RXTE (diamonds), BATSE (up-triangles), and ICE (down-triangles) data for SGR 1806-20 are from (Gögüs et al. 2000). The solid lines represent fits to the power law distributions.

magnitude larger and the energy release extends up to $10^{44.5}$ ergs, a value corresponding to giant flare events.

The typical time for the energy release is determined by the spanning time of the crust linear size, $\tau_{av} \approx l_{crust}/c_m$. The speed of avalanche propagation c_m is determined by the relaxation time τ_N of nuclear reconfiguration associated with magnetic response. Applying familiar value $\tau_N \approx 10^{-20.5}$ s we find for the speed $c_m \approx a/\tau_N \approx 10^8$ cm/s. The corresponding estimate for spanning time $\tau_{av} \approx 10^{-1}$ ms is in a good agreement with rising time of SGR-bursts (cf. Kouveliotou et al. 1993, 1998, Thompson & Duncan 1995, 1996).

In the reminder of this section we analyze statistical properties of SGR-burst activity, common for various pulsars. In particular, we show that the distribution of magnetization jumps (i.e. number of jumped domain-moments and, respectively, the emitted energy or fluence) displays an universal self-similar power-law behavior, while the scaled waiting time distributions between successive bursts follow a function universal for various sources. We also propose the systematics for periods of SGR active phases.
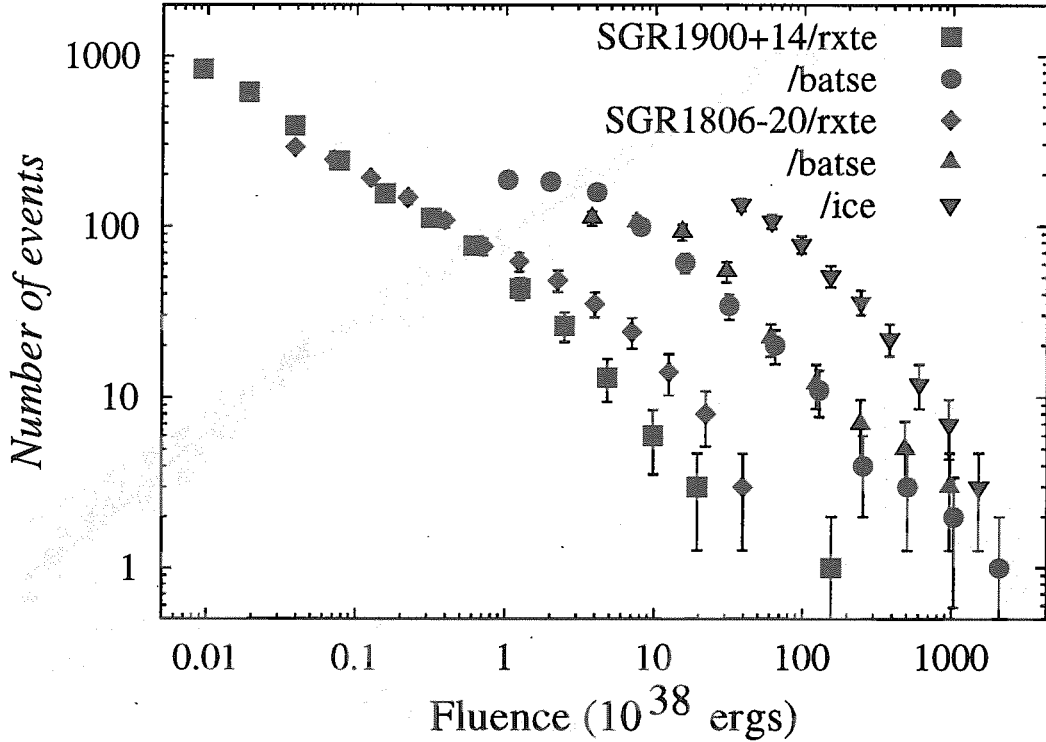
Fig. 35.— Cumulative fluence distribution of SGR-bursts accounting for the remote distances of SGR 1900+14 and SGR 1806-20. The notations are the same as in fig. 34.

9.1. SGR-Burst Statistics

Figure 34 represents the cumulative distributions of detected fluence, i.e. the burst number with a fluence exceeding certain value, as observed by different missions, sensitive to individual regions of emitted energy. The observed distributions are well fitted by the power law dependence. Relevant exponents range from 0.47 to 0.97.

To calculate the total energy released per respective measured burst fluence we assume an isotropic emission of the sources at the remote distances $R \approx 14.5 \pm 1.4$ kpc for SGR 1806-20 (Corbel et al. 1997) and $R \approx 7$ kpc for SGR 1900+14 (Vasisht et al. 1994). Then the total energy associated with the γ-ray burst emission can be estimated to be distributed uniformly over the surface of a size $(4\pi R^2)$ which is evaluated as $(2.53 \cdot 10^{46}$ cm$^2)$ and $(5.8 \cdot 10^{45}$ cm$^2)$ for corresponding pulsars. The result of respective renormalization in the fluence is shown in fig. 35. We see that the observed fluences cover rather wide region of the emitted during the burst energies which extends, in fact, over nearly 6 periods. In particular, the set of RXTE/PCA detectors displays a sensitivity for the fluence region from $7 \cdot 10^{35}$ to $2 \cdot 10^{39}$ ergs for SGR 1900+14 and from $3 \cdot 10^{36}$ to $4.9 \cdot 10^{39}$ ergs for SGR 1806-20, while the observations by BATSE mission yield an information about the burst activity in the range of larger energies $1.1 \cdot 10^{38} - 1.5 \cdot 10^{41}$ ergs for SGR 1900+14 and $3.5 \cdot 10^{38} - 1.1 \cdot 10^{41}$ ergs for SGR 1806-20. The upper range of considered
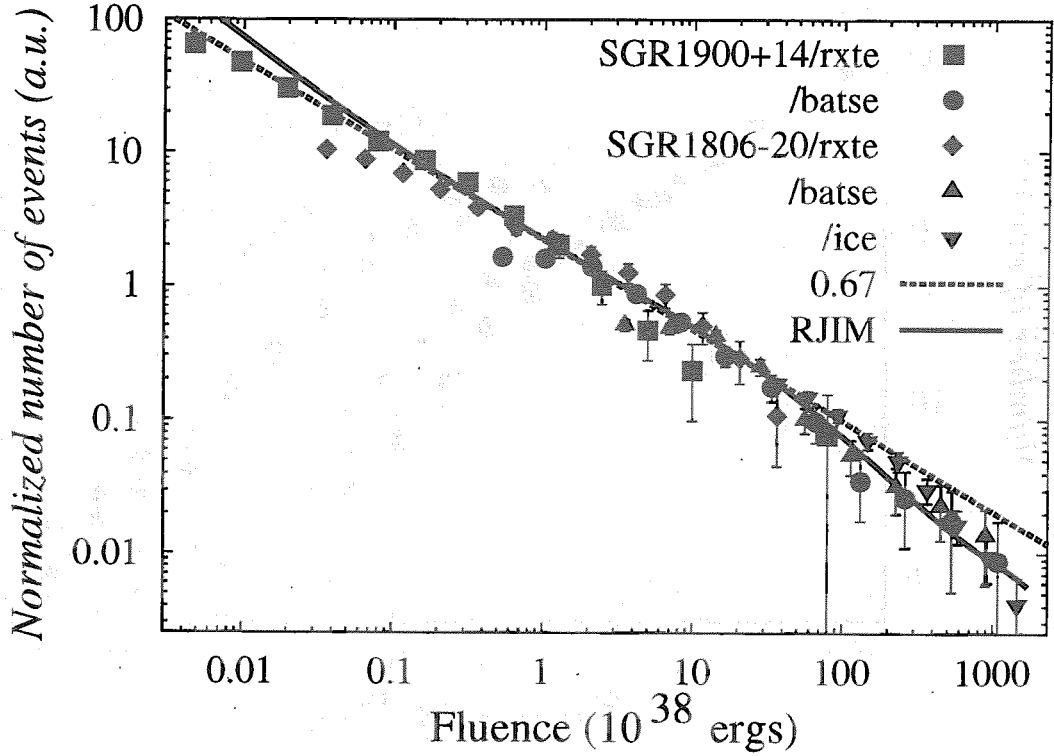
Fig. 36.— Normalized cumulative fluence distributions of SGR-bursts are compared with the avalanche size distribution from RJIM for the cubic lattice of a size $(150)^3$ represented by the solid line. The observational data represent the isotropic fluences accounting for different remoteness of pulsars (see text) and are given by the same notations as in fig. 34. The dashed line denotes the power law distribution.

here fluence distributions is also provided by the results of the ICE mission with isotropic energies between $3.6 \cdot 10^{38}$ and $1.6 \cdot 10^{41}$ ergs for SGR 1806-20.

The cumulative avalanche size distribution in the vicinity of the critical point is compared in figs. 36 and 37 with the normalized cumulative fluence distribution. In the energy range exceeding 5 periods the observations by various missions are in a good agreement with simulations when accounting for the scale of the energy release given by Eq. (126), remoteness, and isotropic emission of such objects. The agreement is slightly better when difference in the distances for sources is taking in to account as compared an assumption of nearly equal remoteness ~ 10 kpc (Kondratyev 2001). Some difference between the data and simulations at the regions corresponding to lower limits of the energies of detectors could be due to reducing detector efficiencies. The obtained event number dependence is well fitted by the power law with an exponent 0.67, which corresponds to the value 1.67 for the differential distribution and provides a signal of self-organized criticality in the burst statistics.

For the case of a constant change rate $\dot{B}$ of the magnetic field the inter-avalanche field interval is proportional to the time interval (i.e. waiting time) between the induced bursts. Taking the respective normalized values, i.e. inter-burst time and inter-avalanche field, we
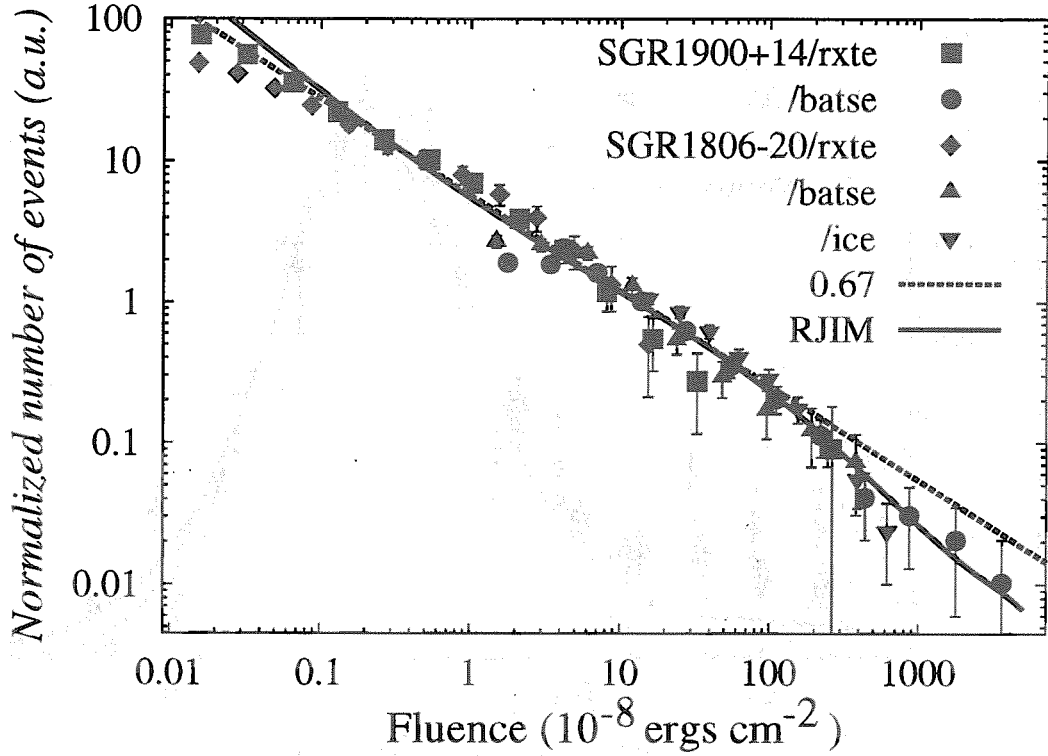
Fig. 37.— The same as fig. 36 but assuming the same remoteness ~ 10 kpc for both sources.

compare the theoretical predictions with observations in fig. 38. The theoretical results are shown for the events, i.e. avalanches, covering entire range of intensities of fig. 36, while the observations are only for bursts registered by RXTE/PCA detector set. As we have seen, however, from analysis of simulation data, the applications of constraints or limits on the avalanche sizes influences considerably the position of the distribution maximum, while the width is only slightly affected.

As seen in fig. 38 for different SGRs the waiting time distributions as a function of the reduced time, i.e. the time normalized at the maximum, obey universal function. The data are well reproduced by simulations and fitted at a maximum by the lognormal function

$$LN(t) = \frac{\theta(t)}{\sqrt{2\pi}t\ln\sigma}\exp\left(-\frac{(\ln t/t_{\mathrm{m}})^2}{2(\ln\sigma)^2}\right) \tag{127}$$

with $\sigma \approx 3.6$. Such a property points out the single time scale for SGR-burst triggering processes. Within RJIM such a time-scale is determined by the ratio of the disorder parameter R and the field change rate $\tau = R/\dot{B}$. Therefore, the scaling with respective time leads to an universal function. It is worthy to point out here the difference in the field change rate during quiescent and active phases.
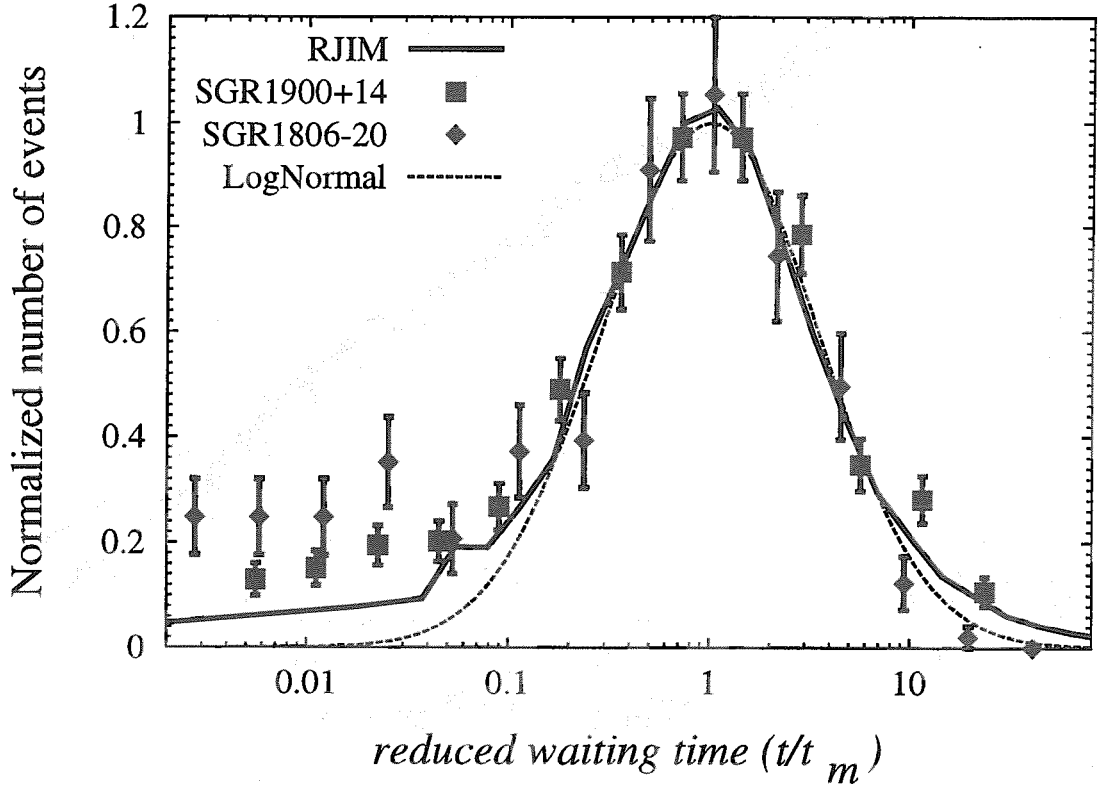
Fig. 38.— The reduced waiting time distribution between the successive RXTE/PCA bursts from SGR 1900+14 (squares) by Gögüs et al. (1999) and SGR 1806-20 (diamonds) by Gögüs et al. (2000) are compared with the waiting time distribution between avalanches (solid curve). The dashed line represents the fit to the lognormal distribution of the width 3.6.

9.2. Periods of Burst Active Phases

According to presented RJIM model the star enters the phase of intensified burst activity when the magnetic field approaches critical values (see fig. 33 and discussion therein). An expectation time T_s for an inactive evolution is then determined by the ratio of the spacing β_{jmp} of magnetic moment jump anomalies (see Eqs. (80) and (81)) and the rate $\dot{B}$ of overall field change, $T_s \approx -\beta_{jmp}/\dot{B}$. Since the magnetic energy $F_B \sim B^2$ dominates and powers the emission we find $\dot{B} \sim -L_p/B$. Using the familiar (Shapiro & Teukolsky 1983) relation $L_p \sim B_p^2$ and assuming the proportionality of the crust field to the field on star magnetic poles [2] $B \sim B_p$ we obtain

$$T_s^2 L_p = const. \qquad (128)$$

In fact, SGR 0526-66 has been reported to have nearly half a year period of burst activity (Rothschild & Lingenfelter 1984). At the same time SGR 1900+14 has experienced four active periods during 1979 (Mazets et al. 1981), June – August 1992 (Kouveliotou et al.

---

[2] It is worthy noticing here that such an assumption implies an exponential decay of the field with time $B = B_0 \exp\{-\alpha t\}$. For some sufficiently small time interval it can be always a reasonable approximation.
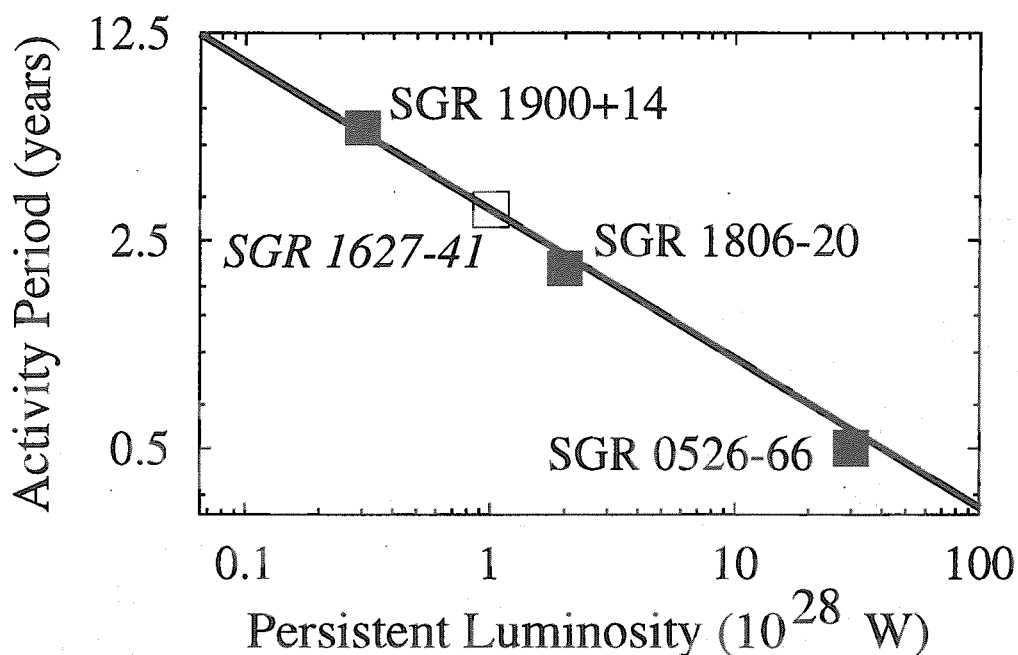
Fig. 39.— Period of SGR's active phases versus the persistent luminosity. The observational data are from (Mazets et al. 1979,1981,Gögüs et al. 1999, 2000, Kouveliotou et al. 1993, 2001) for SGR 1900+14, from (Woods et al. 2000) for SGR 1806-20, from (Rothschild & Lingenfelter 1984) for SGR 0526-66, as also discussed by Zhang, Xu & Qiao (2000). The solid line indicates the systematics with $const \approx 10^{43.5}$ erg·s (see text).

1993), May 1998 – January 1999 (Gögüs et al. 1999, 2000), and April 2001 (Kouveliotou et al. 2001). The active periods are short, and the interval between them varies from 2 to 12 years with an average expectation value of about 6 years. Although SGR 1806-20 activity does not display a clear periodicity, a plausible two years period has been suggested from an analysis of its timing residual (Woods et al. 2000).

As illustrated in fig. 39 SGR's observables follow rather well the systematics given by Eq. (128). The evaluated constant can be compared, e.g., with total angular momentum of neutron star (Shapiro & Teukolsky 1983) with typical period $10^{0.5}$ s of rotation for SGRs, $I \approx 10^{53.5}$ ergs · s. The obtained systematics predicts an expectation time of 3-4 years for the periodicity of intensive burst sets for SGR 1627-41 (Hurley et al. 2000), suggesting thereby the next probable active phase in fall of 2001 or 2002. We note, however, that fluctuations of level spacing and, corresponding, intervals of magnetic moment jumps give significant variations of activity periods, like in case of SGR 1900+14.

10. Summary and Outlook

Magnetic response of neutron star matter at various densities have been considered by employing the thermodynamic formalism within the mean-field treatment. As demonstrated the uniform neutron liquid shows almost linear magnetization. We have seen that quantization of spatial motion results in a sharp abrupt field dependence of the magnetization. Such a behavior is particularly pronounced in the case of outer crust nuclides with three-dimensional confinement of spatial motion. In such a case the level crossings give rise the jumps of magnetic moments of nuclei.

The Pauli-type paramagnetic response of neutrons results in the moment jumps arising almost periodically at crossings of majority- and minority-spin energy levels. The jump period is determined by the distance between neighboring levels.

The proton magnetic response is determined by the relationship between spin- and orbital-magnetism. It corresponds to more frequent jumps of nuclear moments.

As seen such jump anomalies of magnetic moments in conjunction with ferromagnetic inter-nuclide coupling induce sharp steps in the crust demagnetization process due to avalanche propagations. As a consequence, sudden energy releases to magnetosphere lead to SGR-bursts. The crust seismic activity is not implied within such a triggering mechanism, corroborative with a lack of spin-up glitches in the rotation of such pulsars. The quasi-periodic (with the field) magnetic moment jumps are consistent with some regularities in the SGR-burst emissions and provide a tool for systematic analysis of SGR activity.

For the description of such noisy magnetodynamics of neutron star crusts we develop the RJIM model accounting for quantum fluctuations due to the discrete level structure, internuclide coupling, disorder and demagnetization energy. The comparison of model predictions with observational data allows, therefore, to quantify crust properties in terms of respective set of parameters. From numerical simulations and an analysis based on the mean-field treatment we find the magnetic equation of state and identify conditions corresponding to the occurrence of self-organized criticality. As demonstrated the system exhibits universal scaling behavior at such conditions.

As shown the predicted by RJIM model scaling properties for, e.g., the burst intensity and waiting time distributions, are in a good agreement with SGR observations supporting thereby the credibility of RJIM model. As implied within considered treatment the specific feature classifying SGRs is plausibly represented by the crust ultra-strong multipolar magnetic field components matching the strength region of important quantization effect in nuclide magnetization. For outer crusts such fields exceed 10^{16} G, while weaker fields are expected for neutron-rich nuclides of inner crusts (Kondratyev, Maruyama & Chiba 2000, 2001, 2001a, Kondratyev 2001a). Further implications of the proposed magnetic

emission mechanism in the analysis of SGR activity can provide better understanding of neutron star crust, in particular, strengths and evolution of magnetic fields.

Finally, we note that arrays of atomic clusters and/or quantum dots (see, e.g., Kondratyev & Lutz 1998, 1999) can display similar noisy magnetodynamics at conditions far from magnetization reversal. Such an effect might be employed as a tool to analyze the roughness and disorder in an array.

References

Audi, G., & Wapstra, A.H. 1995, Nucl. Phys. A, 595, 409

Baym, G., Pethick, C.J., & Sutherland, P. 1971, ApJ, 170, 299

Beskin, V.S., Gurevich, A.V., & Istomin, Ya.N. 1993, Physics of the Pulsar Magnetosphere (Cambridge: Cambridge University Press)

Brack, M., Creagh, S.C., & Law, J. 1998, Phys. Rev. A, 57, 788

Brack, M., Reimann, S.M., & Sieber, M. 1997, Phys. Rev. Lett., 79, 1817

Broderick, A., Prakash, M., & Lattimer, J.M. 2000, ApJ, 537, 351

Bulgac, A., & Magierski, P. 2001, Nucl. Phys. A, 683, 695

Cardall, C.Y., Prakash, M., & Lattimer, J.M. 2001, ApJ, 554, 1021

Chatterjee, P., Hernquist, L., & Narayan, R. 2000, ApJ, 534, 373

Chatterjee, P., & Hernquist, L. 2000, ApJ, 543, 367

Corbel, S., Wallyn, P., Dame, T.M., Durouchoux, P., Mahoney, W.A., Vilhu, O., & Grindlay, J.E. 1997, ApJ, 478, 624

Douchin, F., & Haensel, P. 2000, Phys. Lett. B 485, 107

Douchin, F., Haensel, P., & Meyer, J. 2000, Nucl. Phys. A665, 419

Duncan, R.C. 1998, ApJ, 498, L45

Duncan, R.C., & Li, H. 1997, ApJ, 484, 720

Duncan, R.C., & Thompson, C. 1992, ApJ, 392, L9

Feroci, M., Hurley, K., Duncan, R.C., & Thompson, C. 2001, ApJ, 549, 1021

Feynman, R.P. 1965, The Feynman lectures on Physics (Addison-Wesley, London) sect. II. 37-3

Fock, V. 1928, Z. Phys., 47, 446

Fowler, W.A. 1984, Rev. Mod. Phys., 56, 149

Galloway, D.J., Proctor, M.R., & Weiss, N.O. 1977, Nature(London), 266, 686

Ginzburg, V.L. 1964, Dokl. Akad. Nauk SSSR 156, 43 [1964 Sov. Phys. Dokl. 9, 329]

Gotthelf, E.V., Vasisht, G., & Dotani, T. 1999, ApJ, 522, L49

Göğüs, Ersin et al. 1999, ApJ, 526, L93

Göğüs, Ersin et al. 2000, ApJ, 532, L121

Haensel, P., Zdunik, J.L., & Dobaczewski, J. 1989, A&A, 222, 353

Harding, A.K., Contopoulos, I., & Kazanas,D. 1999, ApJ, 525, L125

Heiselberg, H., & Njorth-Jensen, M. 2000, Phys. Rep., 328,237

Hurley, K., B. McBreen, B., Rabbette, M., & Steel, S. 1994, A&A, 288, L49

Hurley, K. *et. al.* 1999, Nature(London) 397, 41

————— . 1999a, ApJ, 510, L111

————— . 2000, ApJ, 528, L21

Ibrahim, A.I. et al. 2001, ApJ, 558, 237; astro-ph 0007043

Iida, K., & Sato, K. 1997, ApJ, 477, 294

Iyudin, A.F. *et. al.* 1994, A&A, 284, L1

Kaspi, V.M., Chakrabarty, D., & Steinberger, J. 1999, ApJ, 525, L33

Kondratyev, V.N. 1994, Phys. Lett. A, 190, 465

————. 1996, Z. Phys. B, 99, 473

————. 2001, JAERI-Conf. 2001 – 12, 14

————. 2001a, Abstracts of 2nd Int. Symp. on Advanced Science Research: *Advances in Heavy Element Research* (JAERI, Tokai, Japan, Nov. 13 – 15, 2001) P. 60, and J. of Nucl. and Radiochem. Sci. in press

Kondratyev, V.N., & Di Toro, M. 1996, Phys. Rev. C, 53, 2176

Kondratyev, V.N., & Lutz, H.O. 1998, Phys. Rev. Lett., 81, 4508

————. 1999, Eur. Phys. J. D, 9, 483

Kondratyev, V.N., Maruyama, T., & Chiba, S. 2000, Phys. Rev. Lett., 84, 1086

————— . 1999, JAERI-Research 99-065

————— . 2000a, JAERI-Conf. 2000-011, 99

————— . 2001, ApJ, 546, 1137

————— . 2001a, J. Nucl. Sci. Tech. in press

Kouveliotou, C., et al. 1993, Nature(London) 362, 728

Kouveliotou, C., Dieters, S., Strohmayer, T., van Paradijs, J., Fishman, G.J., Meegan, C.A., Hurley, K., Kommers, J., Smith, I. Frail, D., & Murakami, T. 1998, Nature(London) 393, 235

Kouveliotou, C., Strohmayer, T., Hurley, K., van Paradijs, J., Finger, M.H., Dieters, S., Woods, P., Thompson, C., & Duncan, R.C. 1999, ApJ, 510, L115

Kouveliotou, C., Tennant, A., Woods, P.M., Weisskopf, M.C., Hurley, K., Fender, R.P., Garrongton, S.T., Patel, S.K., & Gögüs, E. 2001, ApJ, 558, L47

Lai, D., & Shapiro, S.L. 1991, ApJ, 383, 745

Landau, L.D., & Lifshitz, E.M. 1985, Statistical Physics (Pergamon, Oxford)

Li, X.-D., & Wang, Z.-R. 2000, ApJ, 544, L49

Luttinger, J.M., & Tisza, L. 1946, Phys. Rev., 70, 1946

Marsden, D., Rothschild, R.E., & Ligenfelter, R.E. 1999, ApJ, 520, L107, (E), 523, L97

Mazets, E.P., et al. 1979, Nature (London) 282, 587

———. 1981, ApSS , 80, 3

Maruyama, T., Niita, K., Oyamatsu, K., Maruyama, T., Chiba, S., & Iwamoto, A. 1998, Phys. Rev. C, 57, 655

Möller, P., Nix, J.R., Myers, W.D., & Swiatecki, W.J. 1995, At. & Nucl. Data Tables, 59, 185

Murakami, T., Kubo, S., Shibazaki, N., Takeshima, T., Yoshida, A., & Kawai, N., 1999, ApJ, 510, L119

Nilsson, S.G., & Ragnarsson, I. 1990, Shapes and Shells in Nuclear Structure (Cambridge Univ. Press, Cambridge)

Oyamatsu, K., & Yamada, M. 1994, Nucl. Phys. A578, 181

Pagel, B.E.J. 1997, Nucleosynthesis and Chemical Evolution of Galaxies (Cambridge, Cambridge University Press)

Pethick, C.J., & Potekhin, A.Y. 1998, Phys. Lett. B, 427, 7

Pethick, C.J., & Ravenhall, D.G. 1995, Ann. Rev. Nucl. Part. Sci., 45, 429

Pethick, C.J., Ravenhall, D.G., & Lorenz, C.P. 1995, Nucl. Phys. A584, 675

Ring, P., & Schuck, P. 1980, The Nuclear Many-Body Problem (Springer, Berlin)

Rolfs, C.E., & Rodney, W.S. 1988, Cauldrons in the Cosmos (Chicago Univ. Press, Chicago)

Rothschild, R.E., & Lingenfelter, R.E. 1984, Nature (London), 312, 737

Ruderman, M., Zhu, T., & Chen, K. 1998, ApJ, 492, 267

Schaab, Ch., Weber, F., & Weigel, M.K. 1998, A&A, 335, 596

Shapiro, S.L., & Teukolsky, S.A. 1983, Black Holes, White Dwarfs and Neutron Stars (Willey, NY)

Stanley, H.E. 1987, *Introduction to Phase Transitions and Critical Phenomena* (Oxford University Press, Oxford)

Strutinsky, V.M. 1967, Nucl. Phys. A95, 420

——— . 1968, Nucl. Phys. A122, 1

Suh, I.S., & Mathews, G.J. 2001, ApJ, 546, 1126

Tatsumi, T. Phys. Lett. B, 489, 280

Terletskii, Ya.P. 1939, Zhurn. Eksp. Teor. Fiz. 9, 796

The, L.-S., Leising, M. D., Kurfess, J. D., Johnson, W. N., Hartmann, D. H., Gehrels, N., Grove, J. E., & Purcell, W. R. 1996, A&AS, 120, 357

Thompson, C., & Duncan, R.C. 1995, MNRAS, 275, 255

———. 1996, ApJ, 498, 322

Thompson, C., Duncan, R.C., Woods, P.M., Kouveliotou, C., Finger, M.H., & van Paradijs, J. 2000, ApJ, 543, 340; preprint (astro-ph/9908086)

Thompson, C., & Murray, N. 2001, ApJ, 560, 339

Tsuruta, S. 1998, Phys. Rep. 292, 1

van Leeuwen, J.A. 1921, J. Phys. (Paris) 2, 361

Vasisht, G., Kulkarni, S.R., Frail, D.A., Greiner, J. 1994, ApJ, 431, L35·

Vertse, T., Kruppa, A.T., Liotta, R.J., Nazarewicz, W. Sandulescu, N., & Werner, T.R. 1998, Phys. Rev. C, 57, 3089

Watanabe, G., Iida, K., & Sato, K. 2000, Nucl. Phys. A676, 455

Watanabe, G., Iida, K., & Sato, K. 2001, Nucl. Phys. A687, 512

Weis, J.J., & Levesque, D. 1993, Phys. Rev. E, 48, 3728

————. 1994, Phys. Rev. E, 49, 5131

Woltjer, L. 1964, ApJ, 140, 13409

Woods, P.M., et al. 2000, ApJ, 535, L55

Woods, P.M., Kouveliotou, C., Gögüs, E., Finger, M.H., Swank, J., Smith, D.H., Hurley, K., & Thompson, C. 2001, ApJ, 552, 748

Usov, V.V. 2001, Phys. Rev. Lett., 87, 021101

Zhang, B., Xu, R.X., & Qiao, G.J. 2000, ApJ, 545, L127

This plano tables was prepared with the AAS LaTeX macros v4.0.

Appendix

A. Thermal Effects in Shell-Corrections

The thermal effects in the oscillating parts of thermodynamic quantities are related to the integrals of the form (cf. Eqs. (24), (25), (26), and (27))

$$O(T) = \int_{-\infty}^{\infty} d\epsilon \cdot L(\epsilon) \exp\{i\mathcal{S}(\epsilon)/\hbar\} \mathcal{F}'(\epsilon - \lambda) , \qquad (A1)$$

where the multiplier $L(\epsilon) \exp\{i\mathcal{S}(\epsilon)/\hbar\}$ originates from the oscillating level density components. Within the semiclassical treatment such oscillations are associated with a contributions of periodic orbits, while the quantity $\mathcal{S}(\epsilon)$ denotes an action integral along the orbit with the period $\mathcal{T}(\epsilon) = d\mathcal{S}(\epsilon)/d\epsilon$. In the case of Landau levels or HO the relation Eq. (A1) with $\mathcal{S}(\epsilon) = 2\pi\epsilon/\omega$ represents an exact result of quantum mechanical treatment. At realistic temperatures T the energy derivative of the Fermi distribution function $\mathcal{F}'(\epsilon)$ exhibits a sharp peak of a width T at chemical potential $\epsilon = \lambda$ and approaches zero at other values of the argument. In the limit $T \to 0$ the energy derivative becomes a δ-function $\mathcal{F}'(x) = -\delta(x)$.

Therefore, we can employ the linear expansion of an action $\mathcal{S}$ in the vicinity of chemical potential $\mathcal{S}(\epsilon) \approx \mathcal{S}(\lambda) + \mathcal{T} \cdot (\epsilon - \lambda)$. Then, integrating over the energy in Eq. (A1) and making use of the relation

$$\int_0^{\infty} dx \frac{x^y}{1+x} = \frac{-\pi}{\sin(\pi y)} ,$$

we obtain the thermally smoothed oscillating part in the following form

$$O = L(\lambda) \exp\{i\mathcal{S}(\lambda)/\hbar\} R(T/T_{\text{th}}) , \qquad (A2)$$

where $R(x) = x/\sinh(x)$, $T_{\text{th}} = \hbar/(\pi T)$, and $\mathcal{T} = \mathcal{T}(\lambda)$.

B. The Fermi Integrals

We briefly outline here some properties of the Fermi integrals

$$I_\nu(z) = \Gamma(\nu + 1) f_{\nu+1}(\exp\{z\}) , \qquad (B1)$$

$$f_\nu(y) = (\Gamma(\nu))^{-1} \int_0^{\infty} \frac{x^{\nu-1} dx}{\exp\{x\}/y + 1} , \qquad (B2)$$

$$\Gamma(\nu) = \int_0^{\infty} x^{\nu-1} \exp\{-x\} dx \qquad (B3)$$

which reflects the characteristics of the Fermi systems.

At high temperatures $T \gtrsim \lambda$, i.e. small fugacity $y = \exp\{\lambda/T\} \lesssim \pi$, the function $f_\nu(y)$ can be expanded as a series

$$f_\nu(y) \approx \sum_{i=1}^{\infty} (-1)^{i-1} y^i / i^\nu . \qquad (B4)$$

At low temperatures the Fermi integration can be written by making use of the Sommerfeld lemma (Landau & Lifshitz 1985) as a quickly convergent series

$$
\begin{aligned}
f_\nu(y) \approx & \left(\Gamma(\nu)^{-1} z^\nu \left(1 + \frac{\nu(\nu-1)}{6} \left(\frac{\pi}{z}\right)^2 \right.\right. \\
& \left. + \frac{7\nu(\nu-1)(\nu-2)(\nu-3)}{360} \left(\frac{\pi}{z}\right)^4 + \ldots \right).
\end{aligned}
\tag{B5}
$$

国際単位系 (SI)と換算表

表1　SI基本単位および補助単位

量	名　称	記　号
長　　　さ	メ ー ト ル	m
質　　　量	キログラム	kg
時　　　間	秒	s
電　　　流	アンペア	A
熱力学温度	ケ ル ビ ン	K
物　質　量	モ ー ル	mol
光　　　度	カ ン デ ラ	cd
平　面　角	ラ ジ ア ン	rad
立　体　角	ステラジアン	sr

表3　固有の名称をもつSI組立単位

量	名　称	記号	他のSI単位による表現
周　波　数	ヘ ル ツ	Hz	s^{-1}
力	ニュートン	N	$m \cdot kg/s^2$
圧　力，応　力	パ ス カ ル	Pa	N/m^2
エネルギー,仕事,熱量	ジ ュ ー ル	J	$N \cdot m$
工率，放射束	ワ ッ ト	W	J/s
電　気　量，電　荷	ク ー ロ ン	C	$A \cdot s$
電位,電圧,起電力	ボ ル ト	V	W/A
静　電　容　量	フ ァ ラ ド	F	C/V
電　気　抵　抗	オ ー ム	Ω	V/A
コンダクタンス	ジ ー メ ン ス	S	A/V
磁　　　　　束	ウ ェ ー バ	Wb	$V \cdot s$
磁　束　密　度	テ ス ラ	T	Wb/m^2
インダクタンス	ヘ ン リ ー	H	Wb/A
セルシウス温度	セルシウス度	℃	
光　　　　　束	ル ー メ ン	lm	$cd \cdot sr$
照　　　　　度	ル ク ス	lx	lm/m^2
放　　射　　能	ベ ク レ ル	Bq	s^{-1}
吸　収　線　量	グ レ イ	Gy	J/kg
線　量　等　量	シ ー ベ ル ト	Sv	J/kg

表2　SIと併用される単位

名　称	記　号
分，時，日	min, h, d
度，分，秒	°, ′, ″
リ ッ ト ル	l, L
ト ン	t
電 子 ボ ル ト	eV
原子質量単位	u

$1 \text{ eV} = 1.60218 \times 10^{-19} \text{J}$

$1 \text{ u} = 1.66054 \times 10^{-27} \text{kg}$

表4　SIと共に暫定的に維持される単位

名　称	記　号
オングストローム	Å
バ ー ン	b
バ ー ル	bar
ガ ル	Gal
キ ュ リ ー	Ci
レ ン ト ゲ ン	R
ラ ド	rad
レ ム	rem

$1 \text{ Å} = 0.1 \text{nm} = 10^{-10} \text{m}$

$1 \text{ b} = 100 \text{fm}^2 = 10^{-28} \text{m}^2$

$1 \text{ bar} = 0.1 \text{MPa} = 10^5 \text{Pa}$

$1 \text{ Gal} = 1 \text{cm/s}^2 = 10^{-2} \text{m/s}^2$

$1 \text{ Ci} = 3.7 \times 10^{10} \text{Bq}$

$1 \text{ R} = 2.58 \times 10^{-4} \text{C/kg}$

$1 \text{ rad} = 1 \text{cGy} = 10^{-2} \text{Gy}$

$1 \text{ rem} = 1 \text{cSv} = 10^{-2} \text{Sv}$

表5　SI接頭語

倍数	接頭語	記号
10^{18}	エ ク サ	E
10^{15}	ペ タ	P
10^{12}	テ ラ	T
10^{9}	ギ ガ	G
10^{6}	メ ガ	M
10^{3}	キ ロ	k
10^{2}	ヘ ク ト	h
10^{1}	デ カ	da
10^{-1}	デ シ	d
10^{-2}	セ ン チ	c
10^{-3}	ミ リ	m
10^{-6}	マイクロ	μ
10^{-9}	ナ ノ	n
10^{-12}	ピ コ	p
10^{-15}	フェムト	f
10^{-18}	ア ト	a

(注)
1. 表1−5 は「国際単位系」第5版, 国際度量衡局 1985年刊行による。ただし, 1 eV および 1 uの値はCODATAの1986年推奨値によった。
2. 表4には海里, ノット, アール, ヘクタールも含まれているが日常の単位なのでここでは省略した。
3. bar は, JISでは流体の圧力を表わす場合に限り表2のカテゴリーに分類されている。
4. EC閣僚理事会指令では bar, barnおよび「血圧の単位」mmHgを表2のカテゴリーに入れている。

換　算　表

力

力	N(=10^5dyn)	kgf	lbf
	1	0.101972	0.224809
	9.80665	1	2.20462
	4.44822	0.453592	1

粘　度　$1 \text{Pa} \cdot \text{s}(\text{N} \cdot \text{s}/\text{m}^2) = 10 \text{P}(\text{ポアズ})(\text{g}/(\text{cm} \cdot \text{s}))$

動粘度　$1 \text{m}^2/\text{s} = 10^4 \text{St}(\text{ストークス})(\text{cm}^2/\text{s})$

圧力

圧力	MPa(=10bar)	kgf/cm²	atm	mmHg(Torr)	lbf/in²(psi)
	1	10.1972	9.86923	7.50062×10^3	145.038
	0.0980665	1	0.967841	735.559	14.2233
	0.101325	1.03323	1	760	14.6959
	1.33322×10^{-4}	1.35951×10^{-3}	1.31579×10^{-3}	1	1.93368×10^{-2}
	6.89476×10^{-3}	7.03070×10^{-2}	6.80460×10^{-2}	51.7149	1

エネルギー・仕事・熱量

エネルギー・仕事・熱量	J(=10^7 erg)	kgf·m	kW·h	cal(計量法)	Btu	ft·lbf	eV
	1	0.101972	2.77778×10^{-7}	0.238889	9.47813×10^{-4}	0.737562	6.24150×10^{18}
	9.80665	1	2.72407×10^{-6}	2.34270	9.29487×10^{-3}	7.23301	6.12082×10^{19}
	3.6×10^6	3.67098×10^5	1	8.59999×10^5	3412.13	2.65522×10^6	2.24694×10^{25}
	4.18605	0.426858	1.16279×10^{-6}	1	3.96759×10^{-3}	3.08747	2.61272×10^{19}
	1055.06	107.586	2.93072×10^{-4}	252.042	1	778.172	6.58515×10^{21}
	1.35582	0.138255	3.76616×10^{-7}	0.323890	1.28506×10^{-3}	1	8.46233×10^{18}
	1.60218×10^{-19}	1.63377×10^{-20}	4.45050×10^{-26}	3.82743×10^{-20}	1.51857×10^{-22}	1.18171×10^{-19}	1

$1 \text{ cal} = 4.18605 \text{J}$（計量法）

$= 4.184 \text{J}$（熱化学）

$= 4.1855 \text{J}$（15℃）

$= 4.1868 \text{J}$（国際蒸気表）

仕事率　1 PS(仏馬力)

$= 75 \text{ kgf} \cdot \text{m/s}$

$= 735.499 \text{W}$

放射能

放射能	Bq	Ci
	1	2.70270×10^{-11}
	3.7×10^{10}	1

吸収線量

吸収線量	Gy	rad
	1	100
	0.01	1

照射線量

照射線量	C/kg	R
	1	3876
	2.58×10^{-4}	1

線量当量

線量当量	Sv	rem
	1	100
	0.01	1